Henryk Niewodniczański Institute of Nuclear Physics,
Polish Academy of Sciences,
Kraków, Poland

Study of cosmic ray extensive air showers in the Pierre Auger Observatory

Nataliia Borodai

Thesis submitted for the Doctor degree
prepared under the supervision of prof. dr hab. Henryk Wilczyński

Kraków, 2013

Abstract

The subject of this thesis is the experimental study of the optical image of extensive air showers generated by ultra high energy cosmic ray particles. This analysis is based on the determination of the lateral distribution of light in the shower optical image recorded by the fluorescence detector of the Pierre Auger Observatory. The lateral distribution was measured at different stages of shower development, i.e. at different shower ages, for showers with energies higher than 10^{18} eV. The measured lateral distribution profiles are compared to those obtained from the simulations, for the purpose of testing the function of lateral distribution of fluorescence light (the so-called Góra function), used for parameterization of the light distribution. The test has shown that the Góra function describes the measured fluorescence light distribution, if all atmospheric and telescope effects are included properly. Based on the knowledge of the Góra function at each shower age and using the measured lateral distribution of light, the method of calculation of the depth of shower maximum (X_{max}) using the shower age was elaborated. The first results obtained using this method give the approximate values of X_{max}, which are in agreement with the expected values.

Streszczenie

Przedmiotem niniejszej pracy jest eksperymentalne badanie obrazu optycznego wielkich pęków atmosferycznych generowanych przez cząstki promieniowania kosmicznego o bardzo wysokiej energii. Analiza ta jest oparta na wyznaczaniu rozkładu poprzecznego światła w obrazie optycznym pęku, rejestrowanym przez detektor fluorescencyjny Obserwatorium Pierre Auger. Rozkład poprzeczny został zmierzony na różnych etapach rozwoju pęku, tzn. dla różnych wartości parametru wieku pęku, dla pęków o energiach wyższych niż 10^{18} eV. Profile zmierzonych rozkładów poprzecznych są porównywane z profilami otrzymanymi z symulacji w celu testowania funkcji rozkładu poprzecznego światła fluorescencyjnego (tak zwanej funkcji Góry), używanej do parametryzacji rozkładu światła. W wyniku testu stwierdzono, że funkcja Góry opisuje rozkład rejestrowanego światła fluorescencyjnego, pod warunkiem że analiza obejmuje wszystkie efekty atmosferyczne i aparaturowe, poprawnie uwzględnione. W oparciu o znajomość funkcji Góry dla każdego wieku pęku i stosując zmierzony rozkład poprzeczny światła, została opracowana metoda obliczania głębokości atmosferycznej maksimum pęku ($X_{\max}$) za pomocą wieku pęku. Pierwsze wyniki uzyskane przy użyciu tej metody dają przybliżone wartości $X_{\max}$, które zgadzają się z wartościami oczekiwanymi.

Contents

1. Introduction

The Earth's atmosphere is constantly bombarded by high energy subatomic cosmic ray particles. Among them there are particles with energies higher than 10^{18} eV and even above 10^{20} eV. They are called ultra high energy cosmic rays (UHECRs).

Cosmic rays were discovered at the beginning of the twentieth century by Victor Hess. This researcher performed flights on balloons in 1911-1912 and got a surprising result, which showed that with increasing altitude from about 1.5 km, the average ionization of air increased compared to the ionization at the sea level [1]. During one of the Victor Hess's flights a solar eclipse occurred, but the drop of ionization had not happened. Those observations were a convincing evidence of the fact that the source of ionizing radiation was outside the atmosphere and it was not the Sun.

These experiments laid the foundation for the new direction in physics, known as the cosmic rays physics. Later in 1936 Victor Hess was awarded the Nobel Prize for his discovery of cosmic rays.

Cosmic rays do not reach the Earth's surface directly. They interact with the atmosphere, creating cascades of secondary particles, so-called extensive air showers (EAS). Most particles, born in this process, move nearly at the same direction as the initial cosmic ray due to momentum conservation. Traversing the atmosphere, they leave their energy deposited in the air. Furthermore, their interactions with the atmospheric nitrogen molecules lead to ultraviolet light emission. This light can be registered by sensitive optical fluorescence detectors. Shower particles, able to reach the Earth's surface, can be detected by particle detectors on the ground.

UHECRs with the energy about 10^{20} eV are very rare events. On average, less than one such particle falls on every square kilometer of the Earth's surface only once per century. Fluxes of the ultra high energy particles are so small, that their measurements require rather large detectors and therefore scientists are working mainly with large detector systems, located on the ground, like the Pierre Auger Observatory [2], the Telescope Array (TA) [3], Yakutsk air shower Array [4], etc. At the same time another experiment Extreme Universe Space Observatory JEM-EUSO [5] for UHECRs investigation is now in the construction phase. Its detectors will record the fluorescence light from extensive air showers by looking downward from space at the Earth's atmosphere during nights.

Measurements of cosmic ray properties, performed at the different experiments, do not completely agree to each other. That may be probably a result of the inaccuracies in the processes of air shower detection and reconstruction. That is why it is important for all

experiments to make the precise detection of UHECRs and to reveal the sources of experimental uncertainties, in order to eliminate them in the reconstruction procedures.

The Pierre Auger Observatory is a very good instrument for measurements of the extensive air showers. It gives the unprecedented statistics of the events with the energy higher than 10^{18} eV that can help in revealing of the cosmic rays mysteries. In the currently conducted Auger experiments two main types of detectors are used for taking data: a network of the ground-based detectors, which register air shower particles, which passed through detectors; and the fluorescence detectors - optical telescopes, which measure fluorescence light induced by charged particles of extensive air shower in the air. These observations enable the measurements of the lateral and longitudinal shower profiles that makes possible to observe the whole process of the development of showers, which are in the detector field of view. The detection of extensive air shower is a complicated process, which requires consideration and modeling of several significant physical phenomena, in particular, the cascade light development with the proper estimation of all the separate shower components, telescope effects, choice of the right atmosphere and geographical position of event, multiple scattering, etc. This work, in particular, is dedicated to the study of the fluorescence detection method and to the search and elimination of the factors that may influence the shower signal, measured at the Pierre Auger Observatory.

The aim of this work is to measure the lateral distribution of light in the fluorescence detector and to study its change during the shower development in the atmosphere, i.e. for different shower ages. For this purpose the procedure of the signal estimation in the shower optical image was developed. The lateral profiles were calculated both for the thoroughly selected recorded showers and for their simulations. The measured lateral distribution of fluorescence light was further compared to the simulated profiles, created using a theoretical function. This procedure allowed investigation of the method of shower maximum determination based on the width of lateral distribution of fluorescence light in the shower optical image.

The more detailed plan of this work is as follows. Main problems of the cosmic ray physics are discussed in section 2. Furthermore this section includes the basic facts, related to the development of the extensive air shower, and also the shower detection methods. In section 3 the Pierre Auger experiment is described, with particular emphasis on the hybrid detection technique. In addition, this section contains the recent results, obtained in the Pierre Auger Observatory. Section 4 embraces the description of the procedures of reconstruction and simulation of real extensive air shower, using the modern programming

tools. The main analysis includes the results, obtained by the author, and is presented in sections 5 and 6. In particular, the method of shower image registration in the fluorescence detector camera is described in detail in section 5. It also includes the parameterizations of the lateral distribution of shower fluorescence light. Special attention is paid to the parameterization using the phenomenological Góra function, the experimental test of which is discussed in the next section. Lateral shower profiles for measured and simulated extensive air showers are presented in sections 5 and 6. Based on these profiles the method of shower maximum determination, using the measured and simulated fluorescence light, is investigated in section 6. A short summarizing overview of the results, presented in this work, is given in the last section.

2. Ultra High Energy Cosmic Rays

The most energetic UHECRs ever observed have energy of the order 10^{20} eV. Such events are very rare (only less than one particle with energy higher than 10^{20} eV is observed per km^2 per millennium). Due to the extremely low flux of UHECRs at the Earth, the direct detection of such particles is impractical. When cosmic ray enters the atmosphere, it produces an extensive air shower of secondary particles. Using the atmosphere as the detector volume, the air shower particles can be registered and such parameters as energy, arrival direction and nuclear mass composition of primary cosmic rays can be reconstructed.

In this section both the physical properties of primary UHECRs and the development and detection of extensive air showers, initiated by them, are treated.

2.1. Physics of cosmic rays

What gives to the ordinary proton such energy, which is 10^7 times higher than the energy reached by the most powerful terrestrial accelerators? Where are the UHECRs coming from? These and other questions, concerning the cosmic ray physics, researchers are trying to answer for nearly a century. In particular, the urgent theoretical problems, which need to be solved, include the following aspects:

- it is still unclear, whether the UHECRs with energy higher, than theoretically predicted limit GZK-cutoff, exist; this has to be proven experimentally;

- the composition of the UHECRs is a one more problem to solve;

- there is no universal and commonly accepted acceleration mechanism of UHECRs;

- the question of UHECRs origin is still open: there are no astrophysical sources (such as active galactic nuclei, galaxy clusters, etc.) in the measured arrival directions of UHECRs.

So, despite the intensive investigations the nature of cosmic rays remains unclear. Due to the correlation of these problems, solving one of them will greatly facilitate the solution of another.

2.1.1. Energy spectrum and the GZK-effect

The flux of cosmic rays, i.e. number of particles above a given energy, changes much with energy. About one cosmic ray particle with energy 10^{11} eV arrives at m^2 per second, whereas for energies in the range of $10^{15} \div 10^{16}$ eV (the so-called “knee region”) only one particle is coming at m^2 per year, and for 10^{20} eV the flux of cosmic rays drops to

mere one particle at km^2 per century (Fig.2.1). That is why, for measurements of the UHECRs, either a lot of time for acquisition of these particles, or detectors of a big size are needed, in order to compensate such a low flux of UHECRs and accumulate a significant statistics of them. As these conditions are unaffordable for satellite or balloon-based detectors, so the most rational solution is to build a ground-based detector with a large area for collecting data during the long period of time (such as the Pierre Auger Observatory – see section 3).

Cosmic ray energy spectrum was measured in several experiments in the range of 10^7 eV to more than 10^{20} eV. The flux of cosmic rays can be described by a non-thermal energy spectrum, represented approximately by an inverse power law in energy [6]

$$\frac{dN}{dE} \propto E^{-\gamma}. \qquad [Eq.\,2.1]$$

Up to 10^{15} eV the spectral index of cosmic ray spectrum can be approximated by $\gamma = 2.7$. However, there are some visible steepening features in spectrum structure, where the spectral index behaves different (Fig.2.1.). One of them is the *knee*, i.e. a steepening with changing of the spectral index from $\gamma \approx 2.7$ to $\gamma \approx 3.1$ in the range of $10^{15} \div 10^{16}$ eV. Another feature is called the *ankle* and is observed at about 4×10^{18} eV. It is considered, that at the ankle region of spectrum the extragalactic cosmic rays start to dominate over the galactic ones (see section 2.1.3 for details).

The structure of the spectrum in the high energy region becomes better visible, if the cosmic ray flux is multiplied by an energy dependent factor, e.g. $E^{2.6}$, (Fig.2.2.). It should be mentioned that spectrum is generally known up to 10^{19} eV, but starting from this value its shape is not clear enough, as there is small amount of available experimental data and uncertainties on them become larger.

At the energy above 5×10^{19} eV the essential suppression is present in the cosmic ray flux (Fig.2.2). This feature of UHECRs is compatible with the *Greisen-Zatsepin-Kuzmin (GZK) cutoff* [7].

The existence of the GZK-effect was under investigation for a long time. In the 1990s, the GZK-cutoff was not observed in the spectrum of AGASA ground array and an excess over the theoretically predicted GZK-limit was clearly seen in the registered flux (Fig.2.2). At the same time, the GZK-suppression was seen in the first HiRes [8] measurements, which used the fluorescence detection technique for recording light from extensive air showers. To solve the inconsistency between these two results further experiments (the Telescope Array [3], and the Pierre Auger project [9], [10]) were

conducted and presence of GZK-like cutoff in the spectrum was confirmed.

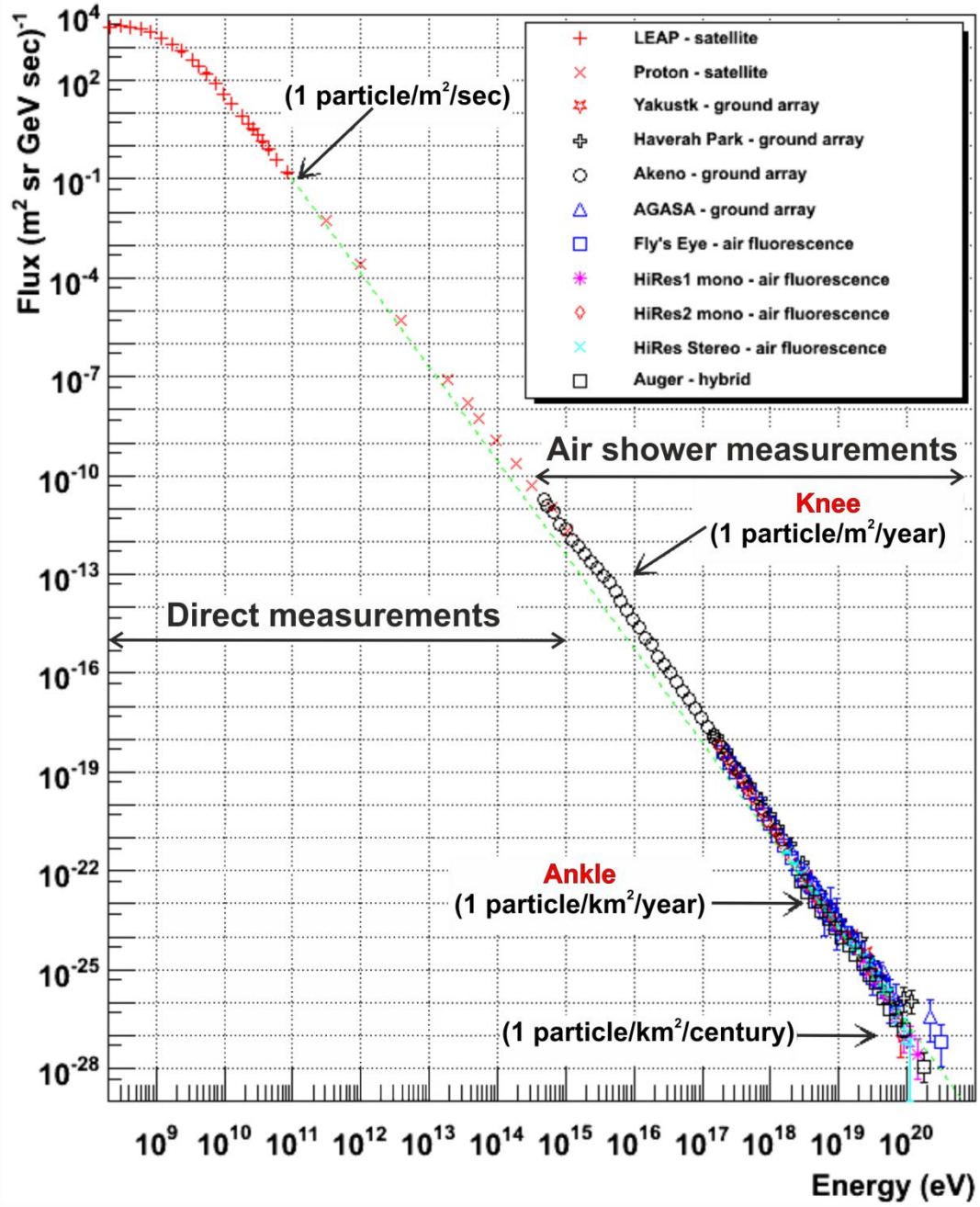

Figure 2.1: The differential all-particle spectrum of cosmic rays above 10^8 eV [11]**.** It combines the measurements of several experiments: direct measurements from the LEAP [12] and Proton [13] experiments and extensive air showers measurements done by Yakutsk [14], Haverah Park [15], Akeno AGASA [16], Fly's Eye [17], HiRes [8] and the Pierre Auger Observatory [9]. For comparison with experimental spectrum measurements, the theoretical spectrum with $\gamma = 3$ is drawn (green dashed line). Also the main shower features, i.e. ankle and knee, are indicated. The frequency of UHECR arrival at the Earth is also shown for different energies (Figure updated from [18]).

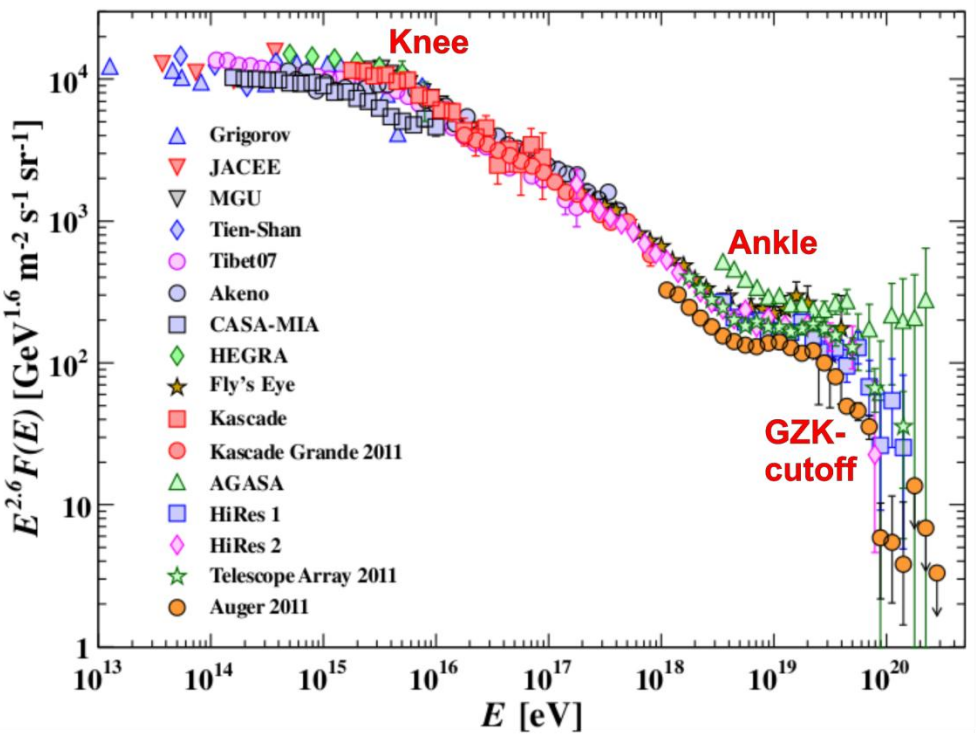

Figure 2.2: Cosmic ray high energy spectrum as measured in different experiments. The spectrum was scaled with the factor of $E^{2.6}$ for better presentation of its structure [19]. Such spectrum features as ankle, knee and GZK-cutoff are indicated.

According to the theory of Greisen, Zatsepin and Kuzmin [20], the energy of the cosmic rays is reduced in the region above $10^{19.5}$ eV due to the significant energy losses, which the primary cosmic ray particles (mainly protons) undergo in the intergalactic medium during interactions with the cosmic microwave background (CMB) radiation γ_{CMB}. The energy of the CMB photons is very low, nevertheless there can be enough center of mass energy of interaction to produce pions and induce high energy losses for these cosmic ray particles, that leads to reduction of their flux. So, as the result of this interaction, the photo-pion production through the resonance Δ^+ is expected

$$p + \gamma_{CMB} \rightarrow \Delta^+ \rightarrow p + \pi^0 \rightarrow p + 2\gamma, \qquad [Eq.\,2.2]$$

$$\rightarrow \Delta^+ \rightarrow n + \pi^+, \qquad [Eq.\,2.3]$$

and the energy of the initial hadron is decreased significantly. The length of the mean free path for this process for proton is very large for energies below the photoproduction threshold, but it decreases quickly for energies above the threshold, that is about several Mpc for energies above 10^{20} eV [21]. Therefore, primary UHECRs suffer essential energy losses from the interactions with CMB, if they are emitted at the distances larger, than several Mpc (Fig.2.3). So that, for example, protons with energies above 10^{20} eV are not

able to travel further than several tens of Mpc [22]. Consequently, the UHECRs which are coming from the distances larger than mentioned ones, are not observed at the Earth. In such a way the existence of the observable GZK-suppression leads to the conclusion that the sources of UHECRs should be nearby (up to 100 Mpc) to allow cosmic rays, accelerated by them, to avoid large energy losses and be able to reach the Earth's atmosphere.

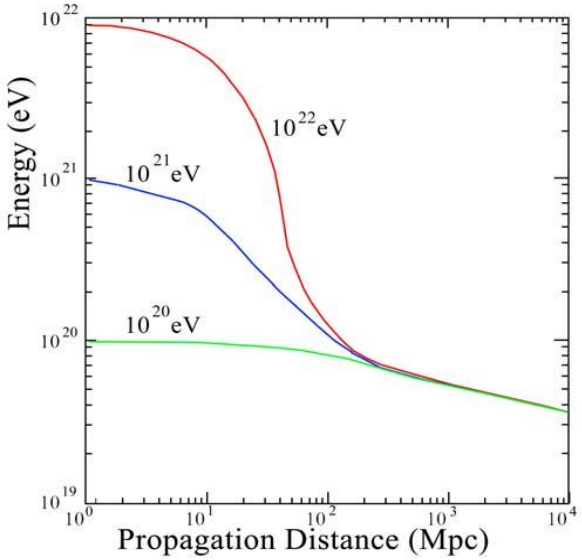

Figure 2.3: Proton primary energy as a function of the propagation distance [22].

As a possible interpretation of energy losses in the ankle region of spectrum, the interaction of extragalactic cosmic ray protons with CMB through the Bethe-Heitler e^+e^- pair production process [23], is commonly treated:

$$p + \gamma_{CMB} \rightarrow \Delta+ \rightarrow p + e^+ + e^-. \qquad [Eq.2.4]$$

Besides mentioned processes, high energy particles may lose their energy due to expansion of the Universe [24], [25].

If one takes into account the described situations, the travelling distance without energy losses shortens considerably for particles with energies above $\sim 10^{19.5}$ eV. So, if ultra-high energy cosmic rays originate from the cosmological distances, their flux should be consequently suppressed above that energy, indicating the GZK-cutoff in the spectrum.

It should be also mentioned that there are several other explanations of steepening after 5×10^{19} eV, different from the GZK-cutoff. For example, it can be interpreted as an inability of the UHECRs sources to accelerate particles to higher energies.

2.1.2. Chemical composition

Identification of the primary particle type for UHECRs is still an urgent problem in the cosmic ray physics, whereas the chemical composition of the low energy cosmic rays

was measured experimentally. For the particles in the energy range from a few MeV up to several TeV almost 86% of primaries are protons, about 11% are helium nuclei, electrons constitute ~2% and nuclei of heavier elements (like iron, carbon, oxygen, etc.) ~1% [25] (Fig.2.4).

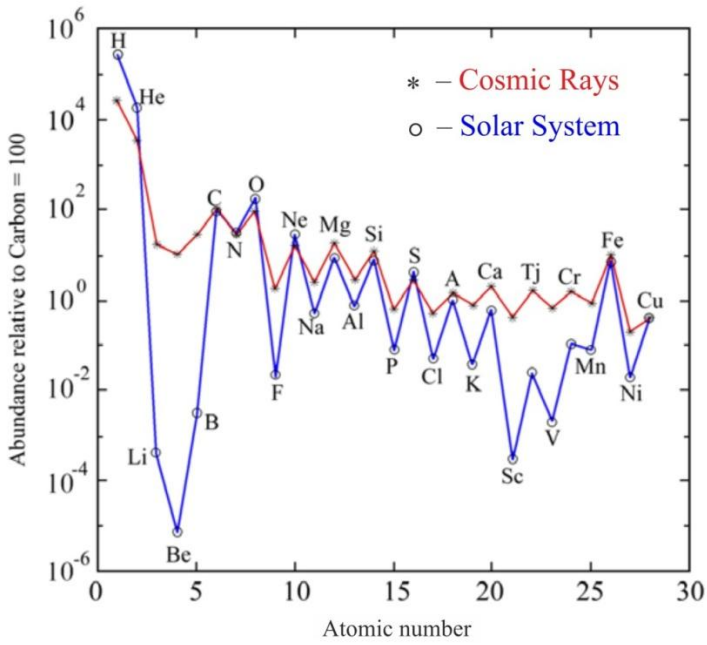

Figure 2.4: The chemical composition of low energy cosmic rays in comparison to solar system composition [26].

Unlike the low energy cosmic rays, primary UHECRs are not directly observed experimentally. That is why direct identification of primary cosmic ray particles is impossible, but it can be approximately inferred from measured extensive air shower properties: either from the measurements of the number of electrons and high energy muons with ground based detectors, or from the estimation of the depth of shower maximum (X_{max} - the depth, at which number of charged shower particles reaches its maximum) and its fluctuations [27] from the longitudinal shower profile (see section 2.2.1), using fluorescence telescopes.

Because of the significant fluctuations in the development from shower to shower (even for showers of the same energy), the primary particle type cannot be identified for each single shower, and is usually represented as an average solution.

The estimation of the mass composition of UHECRs was provided in several air shower experiments. However, the results of those investigations lead to different conclusions. So, light particles (mainly protons) seem to dominate in composition data of HiRes experiment [28]. Whereas, results from the Pierre Auger Observatory (presented in

section 3.3) are based on the greater statistics and indicate the mixed composition of UHECRs, i.e. both protons and iron nuclei are considered as possible primaries [29]. Moreover, the analysis of the dispersion in the depth of shower maximum in Auger data emphasizes a predominance of iron nuclei at the highest energies. Such results may suggest a change in the process of shower development, associated probably with some changes in the nuclear interactions.

2.1.3. Candidate sources and acceleration mechanisms

Observation of a particle with energy above 10^{20} eV [30] implies the existence of the very powerful sites in the universe, able to produce the UHECR. That is why among the most fascinating mysteries in the cosmic ray physics there is also origin of UHECRs that is closely related to a problem of the acceleration of cosmic ray particles to the ultra high energies.

The sources of cosmic rays can vary according to cosmic rays energy values. Cosmic rays in the range of 10^{7} to 10^{8} eV are emitted by the Sun; those in the range of 10^{9} to 10^{17} eV are called galactic cosmic rays as they are predominantly emanated in our Galaxy, in particular as a result of acceleration in supernova remnants. Extragalactic cosmic rays are considered to have the energy starting from above 10^{18} eV and to more than 10^{20} eV, their sources are not known very well.

It is difficult to identify practically even the sources of the galactic cosmic rays with energies around and below the knee region, as trajectories of these particles are curved much due to deflections in the irregular galactic magnetic fields (diffusive propagation of cosmic rays). Consequently, the measured directions, from which the particles arrive to the Earth, do not indicate the location of the sources, which caused the acceleration of these particles. This is why it is considered, that the distribution of arrival directions of these cosmic rays is isotropic.

On the other hand, cosmic rays with energies higher than 10^{19} eV cannot change their path because of the galactic magnetic field, as the Larmor radius of curvature for their trajectory is larger than the radius of the Galaxy itself. Such particles are known as extragalactic cosmic rays as they cannot be kept within the Galaxy and therefore, in the absence of a galactic candidate source, it is supposed that they are coming from the extragalactic sources [31]. It may be possible to determine the locations of the sources of such UHECRs, knowing their arrival directions, which should in good approximation point back to their sources. In particular, if the GZK-effect takes place as expected, the number of

candidate sources can be limited to nearby objects. Such determination of the origin of cosmic rays using pointing to sources method is currently under investigation in cosmic rays physics, making its contribution into the charged particle astronomy.

Among the objects that belong to candidate extragalactic sites, powerful enough to accelerate particles to ultra-high energies, there are: active galactic nuclei (AGN), radio galaxies, clusters of galaxies, gamma-ray bursts (GRB) sources etc. The number of them is limited by the GZK horizon and also by the maximum energy (Fig.2.5), achievable by particle as the result of acceleration by relativistic shock waves. This energy can be estimated as

$$E_{max} \sim b_S \cdot Z \cdot B \cdot L, \qquad [Eq.\,2.5]$$

where $b_S = v/c$, and v – the velocity of the shock wave, Z - the charge of the accelerated particle, B - the magnetic field able to keep the particles inside the acceleration region, and L - the size of the acceleration region.

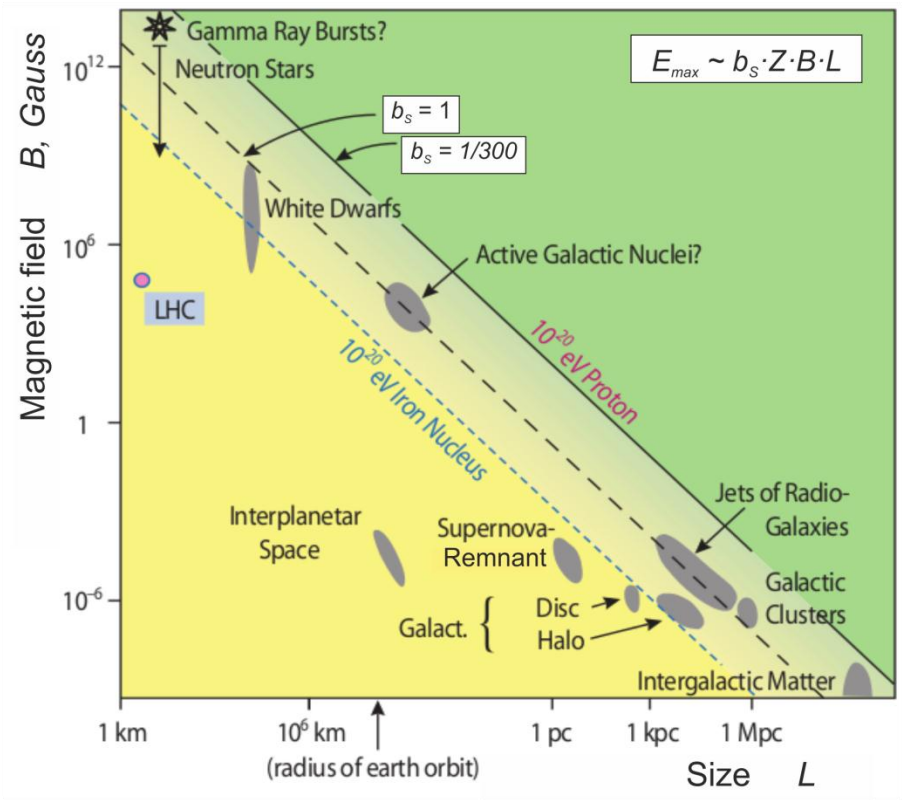

Figure 2.5: Hillas plot of candidate sources for acceleration of ultra high energy cosmic rays [32] in relation to the typical values of their magnetic fields and sizes. Green area depicts the region, in which it is impossible to accelerate the particles to the energies higher, than 10^{20} eV. The diagonal line denotes the sources, capable to accelerate the particles to the given energy. For comparison the point, corresponding to Large Hadron Collider (LHC), is shown.

There are two basic groups of processes, generally used for explanation of the particle acceleration up to the macroscopic energies: bottom-up and top-down models.

Top-down models suppose the creation of UHECRs as the result of the decay or annihilation of the more energetic or supermassive primary particles into the UHECRs. This group is represented by the more speculative exotic mechanisms, originating from the early Universe. In particular, they include the emission of particles by the topological defects (magnetic monopoles, cosmic strings) [33]; from the super-heavy dark matter particles [34]; from the QCD fragmentation [35] or from the Z-burst model [36].

Bottom-up models propose the acceleration from the low to high energies by means of some processes. This group predicts the more realistic scenarios of particle acceleration that can happen in observed astrophysical objects. So, for example, as the result of the explosions in these sources (for example, in supernova) some areas of randomly moving plasma can be created in the space. These areas can be regarded as separate plasma clouds, moving with large velocities relatively to each other. The bulk of plasma particles is kept inside the clouds and moves along with them. However, there is a small number of high-energy particles, for which the radius of curvature of their trajectory in the plasma magnetic field is of the size of the cloud or larger. Such particles, getting into the cloud, are not kept in it and so are deflected by the magnetic field of the cloud. During this process the particle, moving stochastically, is efficiently exchanging the energy with the whole cloud. But the kinetic energy of the cloud is very large and so the energy of the accelerated particles may grow indefinitely, until the particle leaves the area with intensively moving plasma. This statistical acceleration mechanism was suggested by Fermi in 1949 [37]. In the similar way particles may also be accelerated when they interact with the powerful shock waves (e.g., in the intergalactic space), in particular, when two shock waves approach, forming reflecting magnetic "mirrors" (or "wall") for the accelerated particles. Observations at different scales (AGNs, the Galaxy, the Sun, the Earth's magnetosphere, etc.) show that such particle acceleration may take place in the cosmic plasma areas with magnetic fields and intense nonuniform motions of plasma. However, large numbers of particles can be accelerated to very high energies only in the regions with the large kinetic energy of plasma. This is exactly what may happen in such processes as supernova explosions, or during activity of radio galaxies and quasars.

Another example of bottom-up models of cosmic rays acceleration is the “one-shot” mechanism [38]. It implies the direct acceleration of particles to high energy by an extended

electric field. This model can be applicable for such objects as pulsars or active galactic nuclei (AGN).

All acceleration mechanisms lead to the spectrum of cosmic rays, in which the number of particles decreases with increasing energy, but they may give different foresights for the shape of the energy spectrum, chemical composition, etc. That is why a universal acceleration mechanism or combination of mechanisms, able to explain all the features of the spectrum and charge composition of cosmic rays, has not yet been found despite the intensive theoretical and experimental studies.

Consequently, the precise measurements of the flux, energy, arrival direction and particle type of primary cosmic rays are necessary for solving the open questions of UHECRs physics. As the flux of the UHECRs is extremely low, this task can only be done by the experiments with a large exposure, such as the Pierre Auger Observatory [2], or the future space JEM-EUSO observatory [5].

2.2. Extensive air shower development

Extensive air showers (EAS) were discovered in 1938 by the French physicist Pierre Auger [39]. He observed signal from the cosmic ray particles, coming simultaneously to separate detectors, situated several tens meters away from each other. Based on these experimental results, Pierre Auger made a conclusion about the existence of *cascades of secondary particles*, i.e. extensive air showers, initiated by the high energy cosmic rays, and further developing in the atmosphere, causing the correlated arrival of secondary particles at the detectors at the ground level.

The development of an extensive air shower begins when high energy primary particle enters the atmosphere and interacts with a nucleus of air. This interaction provokes a production of secondary particles, which in their turn also interact with air nuclei, producing a large number of particles and creating in such a way a cascade of shower particles (Fig.2.6). During this process, the energy of the primary particle is shared between the secondaries. There are three components that are usually distinguished in the process of the cascade formation in the atmosphere, they are: hadronic, muonic and electromagnetic showers.

The hadronic component is represented mainly by pions and kaons, produced as a result of the collisions. The decays of kaons and pions, created in the hadronic interactions, lead to electromagnetic and muonic cascades.

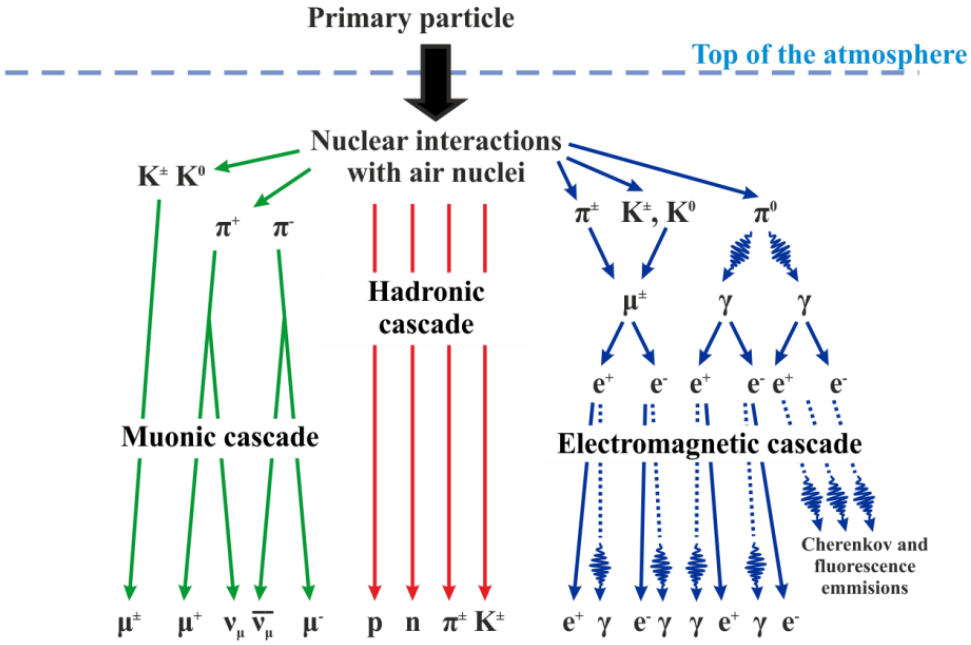

Figure 2.6: Cascade process, caused at the result of interaction of primary comic ray with the atmosphere, includes the production of the following extensive air shower components: hadronic, electromagnetic and muonic.

The electromagnetic component is composed of electrons and photons that appeared from the decay of the products of hadronic collisions. This part of cascade is always the most dominant component of the extensive air shower as it contains the largest part of shower particles. Electromagnetic shower is developing as a result of two main processes: pair-production and bremsstrahlung. Created during these processes photons and electrons have energy sufficient for production of the further particles. Hence, the number of particles in the cascade is growing in the avalanche-like way. The ionization losses start to dominate over the production of new particles, when the mean energy per particle in extensive air shower is below the critical energy (see more details in section 2.2.1.). During this process the total number of particles in the shower is decreasing, leading to the attenuation of the shower.

The muonic component is characterized by the hadronic decay of pions and kaons into the muons and neutrinos. The cross sections for neutrinos are very small, so these particles do not participate in the further interactions and are not detected. Most of the muons are able to reach the ground, as due to the high energy they are not much deflected from their path by multiple scattering. Estimation of the total number of shower muons and electrons is used for the reconstruction of the primary particle type and energy.

So, as the result of the cascade development only electrons, muons, neutrinos, photons and small numbers of hadrons can arrive at the Earth's surface. Secondary electrons and muons are observed in scintillators or through the Cherenkov light emission in water tanks. Fluorescence photons are registered by the fluorescence telescopes (see section 2.3 for details). Determination of the primary energy and mass composition of individual showers in particular is possible by observing the fluorescence light from extensive air showers.

The process of the evolution of the all shower components in the atmosphere can be also described numerically by the so-called differential cascade equations [40], representing the change of the number of particles with slant atmospheric depth X for defined shower energy and primary particle type.

The size of extensive air shower depends on the primary energy, primary particle type and arrival direction of cosmic ray. Showers of ultra high energies are composed of the billions of particles and, when coming to the Earth's surface, can cover the area of several square kilometers. The width of the showers can be estimated using lateral distribution of particles around shower axis, measured by the ground-based detectors. Cosmic ray arrival direction can also be found by measuring the relative arrival time and lateral density of particles at the grid of ground-based detectors. The approximate determination of the primary particle type is possible, knowing the shape of the longitudinal profile and shower maximum ($X_{\max}$). So, it is important to measure precisely the longitudinal and lateral shower profiles, which are responsible for determination of the main shower characteristics. The physics of extensive air shower development, including the description of the shower profiles, is discussed further in this section.

2.2.1. Longitudinal shower development

During developing in the atmosphere, a shower is traversing the amount of matter X (in g/cm^2) before reaching the Earth, where X is known as a slant atmospheric depth.

For the vertical showers the atmospheric depth can be defined as:

$$X_v(h) = \int_h^\infty \rho(h')dh', \qquad [Eq.\,2.6]$$

where h is a given height above the sea level, and ρ is the density profile of the atmosphere. For inclined showers (zenith angle $\theta \leq 60^\circ$) the slant atmospheric depth should be calculated as:

$$X = X_v / \cos\theta. \qquad [Eq.\,2.7]$$

The longitudinal shower profile is represented by the number of particles in the shower, N, as a function of X (Fig.2.7). At the beginning of the shower development the number of particles in the shower is increasing with X, reaching the maximum at X_{max}, after which it is decreasing.

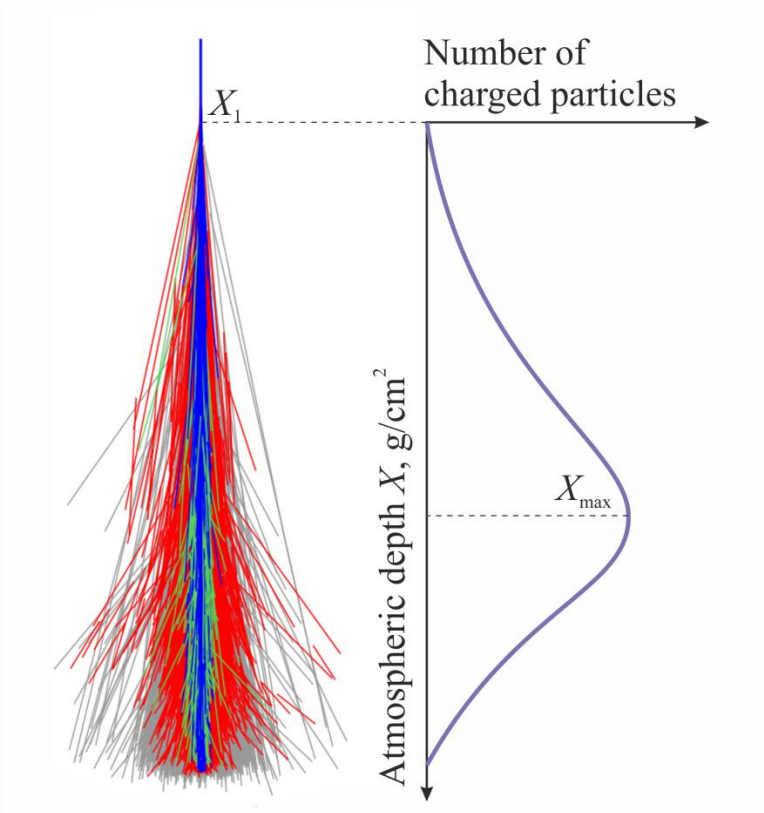

Figure 2.7: The extensive air shower cascade of secondary particles is shown together with longitudinal profile, representing the shower evolution process (schematic view). X_1 indicates the slant depth, at which the first interaction of the primary particle with the atmosphere takes place.

The longitudinal shower profile can be theoretically described by the Gaisser-Hillas parameterization [41]:

$$N(X) = N_{\max}\left(\frac{X - X_1}{X_{\max} - X_1}\right)^{(X_{\max}-X_1)/\lambda} \exp\left(\frac{X_{\max} - X_1}{\lambda}\right), \qquad [Eq.2.8]$$

where N_{max} is the number of particles at shower maximum, X_1 - depth of the first interaction, X_{max} - depth of shower maximum, $\boldsymbol{\lambda}$ - interaction length in air. Using the fit of this function to the measured longitudinal profile points of real event, such main shower parameters as X_{max} and energy can be estimated.

Shower behavior, and so the shape of the longitudinal profile, depends on the type and energy of primary particle. Showers, initiated by light nuclei will have their shower maximum closer to the surface, than showers generated by heavy particles of the same

energy. And also showers with large energy penetrate more deeply into the atmosphere, than showers with small energy.

The Heitler model [42] is a simplified way to describe shower development. It reflects the dependence of $X_{\max}$ on energy in the electromagnetic cascade. In this model Heitler assumed that bremsstrahlung and pair-production processes have equal interaction lengths, i.e. $X_0 = 36.7$ g/cm^2 for both processes, and that when a particle traverse the distance $\lambda = X_0 \ln 2$, two particles are created (e^+, e^- for pair-production process; and e^-, γ for bremsstrahlung) (Fig.2.8). It is also assumed, that during these processes the energy of the parent particle E_0 is shared equally between the created particles. Therefore, if the total number of particles after n iterations is $N = 2^n$, then the energy of each particle is $E_n = E_0 / 2^n$. The cascade continues until the particle energy drops below the critical energy E_C ($E_C = 80$ MeV in air [40]), reaching shower maximum point $X_{\max}$ and further starting the process of shower attenuation. The maximum number $N_{\max} = E_0 / E_C$ of electromagnetic particles is achievable at depth

$$X_{\max} = \lambda \cdot \ln \frac{E_0}{E_C}. \qquad [Eq.\,2.9]$$

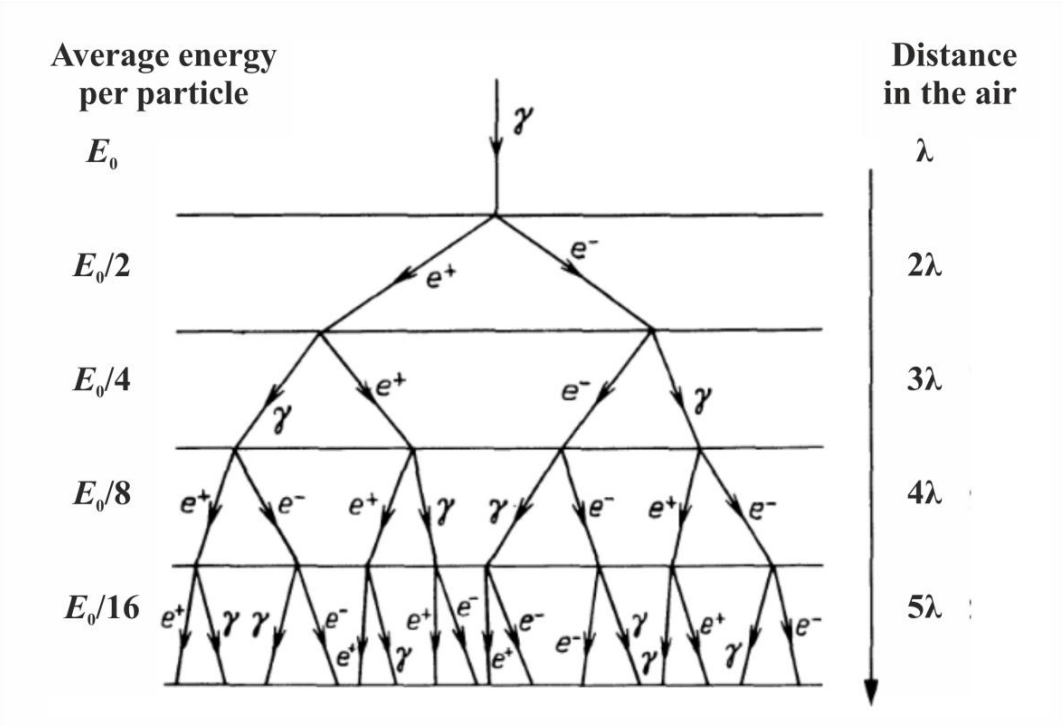

Figure 2.8: The Heitler model of electromagnetic cascade [24].

Although the Heitler model gives a simplified explanation for electromagnetic cascade development, it also brings important relations, that $N_{\max} \sim E_0$ and $X_{\max} \sim \ln E_0$. Furthermore, change of the average $X_{\max}$ with the logarithm of energy, termed as *the*

elongation rate, can be used for determination of the cosmic rays composition (Fig.2.9). For this purpose the average measured X_{max} is compared to the theoretically predicted values for different mass compositions.

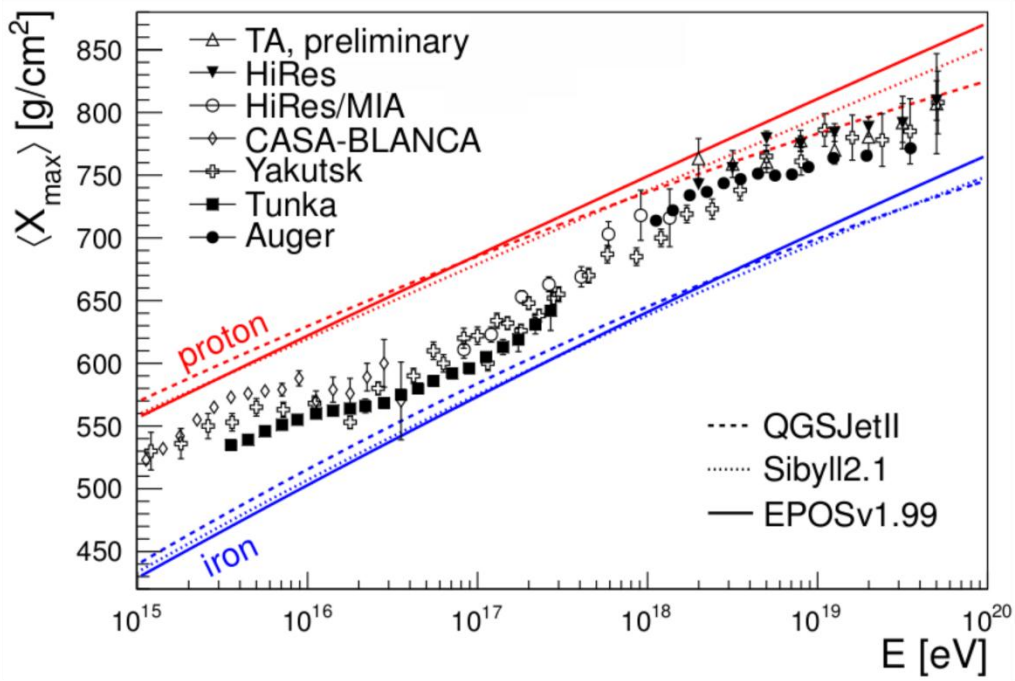

Figure 2.9: Average X_{max} measurements, provided by different experiments and compared to values from Monte Carlo simulations, using different hadronic interaction models, are shown [43]. The information about average mass composition at given energy can be obtained, using measured elongation rate.

2.2.2. Lateral shower profile

Another way to describe the evolution of the shower in the atmosphere is to study the distribution of particles around the shower axis, known as *a lateral distribution* of shower particles. The lateral distribution changes with slant atmospheric depth X, or according to the so-called *shower age* parameter s, and can be estimated at each stage of shower development. For the study of lateral shower profiles several stages of shower development, which correspond to certain values of shower age, can be selected at the shower path (Fig.2.10).

The shower age parameter s is ensued from the theory of the electromagnetic cascades [44]. It can be defined as:

$$s = \frac{3X}{X + 2X_{\max}}. \qquad [Eq.\,2.10]$$

Besides this definition there is also another approximation of shower age [45], according to

which the age parameter equals to:

$$s = \frac{3t}{t + 2 \cdot \ln(E_0/E_C)}, \qquad [Eq.2.11]$$

where $t = X/X_0$ is the slant atmospheric depth in terms of the electromagnetic radiation length X_0.

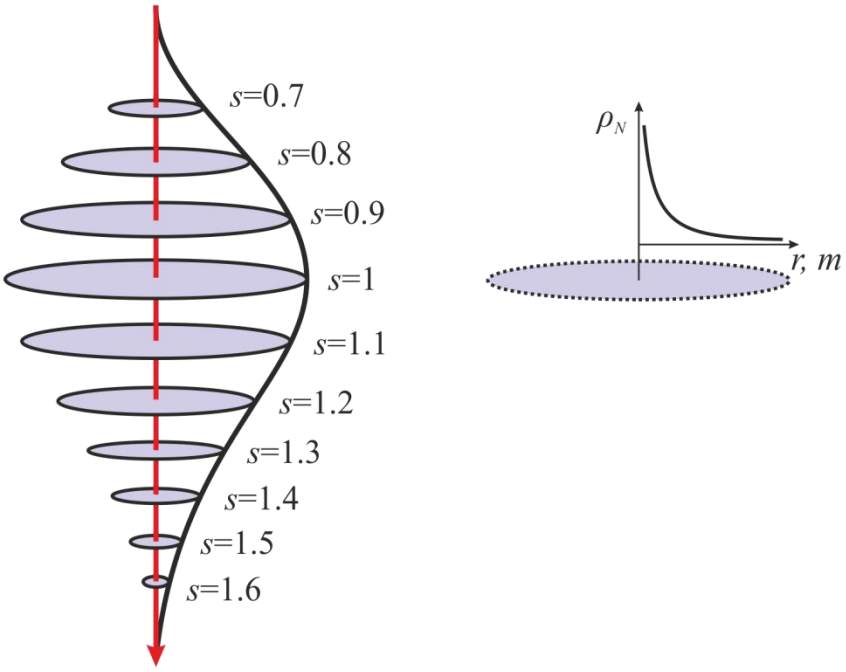

Figure 2.10: Schematic view of the shower, represented by several selected shower development stages. Particularly, such stages can be chosen for measurement of the lateral distribution of particles around shower axis. Shower stages, shown at the scale of the longitudinal shower profile, are indicated by the approximate values of shower age parameter. In addition, the lateral distribution of density of shower particles at certain stage is shown on the right.

The shower age changes according to the shower development in the atmosphere as follows: at $s = 0$ the extensive air shower is initiated by a single particle; at $s = 1$ shower reaches its maximum; and after $s = 1$ it is attenuated [46].

For the lateral and angular distribution of shower particles the Coulomb multiple scattering mechanism is of the most importance. It causes that some extensive air shower particles do not move forward along the shower axis, but are spreading away from axis. The formed shower front resembles a disc, in which the density of shower particles decreases with increasing distance from shower axis, i.e. with the disc radius r (Fig.2.10). By integration of the lateral density ρ_N of charged shower particles the total number of particles N can be found:

$$N(X) = \int \rho_N(X, r) 2\pi r dr. \qquad [Eq.2.12]$$

Examples of lateral distribution of the density of shower particles simulated using the CORSIKA program [47], are shown in Fig.2.11. They include the hadronic, muonic and electromagnetic components.

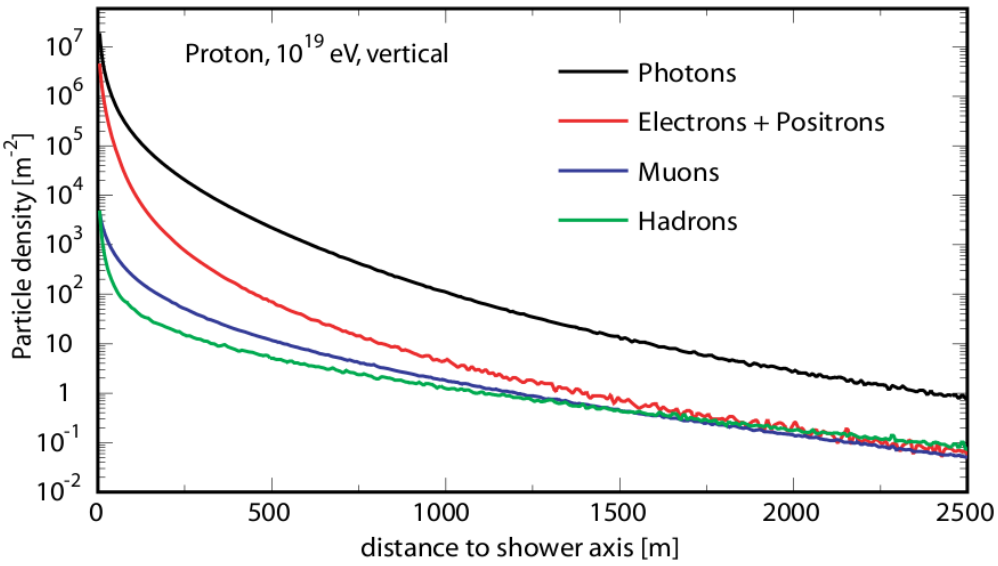

Figure 2.11: Lateral distributions of different shower components, determined at the ground level for the vertical proton shower with energy 10^{19} eV, simulated using the CORSIKA program [47].

Lateral distribution of shower particles at the small distances from the axis can be expressed in terms of *Molière radius* r_M. This is a characteristic, mainly useful for the central part of shower, known as shower core. The Molière radius depends on the atmospheric density $\rho(h)$, and thus on the altitude h, temperature T and pressure P, at which shower is detected [46]:

$$r_M[\mathrm{m}] = 272.5\,\frac{T[\mathrm{K}]\left(\frac{P[\mathrm{mb}]-73.94\cos\theta}{P[\mathrm{mb}]}\right)^{\frac{1}{5.25588}}}{P[\mathrm{mb}]-73.94\cos\theta}, \qquad [Eq.\,2.13]$$

where θ is the shower zenith angle. The Molière radius equals about 78 m at the sea level and about 100 m at the ground level of the Pierre Auger Observatory. It also can be interpreted as:

$$r_M = E_S\frac{X_0}{E_C}/\rho(h) = 9.6\,\frac{\mathrm{g}}{\mathrm{cm}^2}/\rho(h), \qquad [Eq.\,2.14]$$

where $E_S \approx 21$ MeV is the scale energy, $E_C = 80$ MeV the critical energy and $X_0 = 36.7$ g/cm^2 - the radiation length in air (also known as a cascade unit). So, the Molière radius changes along the shower path, in particular, it increases with altitude, while the air density $\rho(h)$ decreases.

The distribution of particles at a certain stage of shower development depends on the history of Molière radius changes with X rather than on the local r_M value at this depth. That is why r_M is usually calculated at 2 cascade units above the appropriate atmospheric depth [46], namely at $X_{NEW} = X - 2X_0/\cos(\theta)$, leading also to calculation of the new altitude value h_{NEW}. This situation is demonstrated in Fig.2.12, where the shift of the mentioned parameters is shown for the estimation of the proper r_M value, based on the atmospheric profile, fitted for the experimentally measured shower (represented in the further sections).

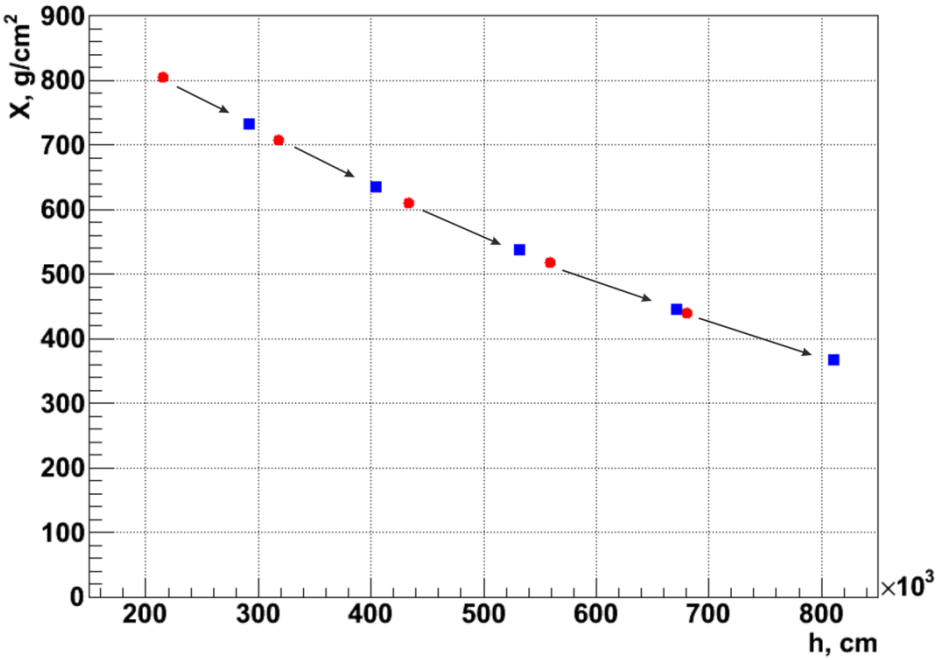

Figure 2.12: Shift of the slant atmospheric depth X (red dots) by 2 cascade units above its current values leads to the new depth X_{NEW} and altitude h_{NEW} values (blue squares), at which the true r_M values should be calculated. The calculations are made for the real atmosphere, appropriate for Auger event #200812102909, analysed in the further sections of this work.

Finally, for estimation of the number and lateral distribution of shower particles, the distance from shower axis is commonly represented in Molière units as $r^* = r/r_M$.

For pure electromagnetic showers the lateral density of e^+e^- particles at distance r from the shower core can be described by the Nishimura-Kamata-Greisen function, also known as the NKG approximation [48]:

$$\rho_N(X,r) = \frac{N(X)}{r_M^2}\left(\frac{r}{r_M}\right)^{s-2}\left(1+\frac{r}{r_M}\right)^{s-4.5}\frac{\Gamma(4.5-s)}{2\pi\Gamma(s)\Gamma(4.5-s)}, \qquad [Eq.2.15]$$

where s is represented by *Eq.*2.11, Γ is the Euler gamma function.

Although the NKG approximation is good for description of electromagnetic cascades, it is not sufficient for the other components (hadronic and muonic) of extensive air

shower. That is why other parameterizations of lateral distribution of shower particles, are under investigation (see section 5.4).

2.3. Air shower detection technique

When cosmic ray particles traverse the atmosphere, they interact with the air molecules, suffer energy losses and can be absorbed. For registration of them at the beginning of their way through the atmosphere direct observations by means of satellites or balloons are possible. These experiments are able to measure cosmic rays with energies up to 10^{15} eV. The other part of cosmic ray energy spectrum can be measured indirectly, through recording the extensive air showers by the ground-based detection systems and fluorescence telescopes. The fluorescence technique [17] is particularly useful for the energies above 10^{17} eV, as it makes possible to estimate the primary cosmic ray energy from the longitudinal shower development in the atmosphere, so that the primary energy is obtained by integrating the energy deposited in the air (see section 2.3.2.).

Thereby, there are two major methods of extensive air shower detection. One of them is to use a ground-based array of detectors, composed of particle counters. The other technique is based on the detection of the fluorescence light during shower traversing of the atmosphere. This kind of light is induced by nitrogen molecules in the air and its measurement makes possible to trace the development of the shower in the atmosphere.

Different detector types can be used in the surface detector for observations of UHECRs. Scintillation counters were used in the Volcano Ranch [49] and AGASA [50] experiments, whereas water-filled Cherenkov detectors were mounted at the Haverah Park [51] experiment and are currently used at the Pierre Auger Observatory. In particular, scintillators detect secondary electrons and muons, whereas Cherenkov detectors register the Cherenkov light produced as the result of interaction of the flux of charged particles with the water.

Besides these main techniques for extensive air shower detection, there are also attempts to develop the new ones. Among them there is a technique of radio detection of cosmic rays. It is very promising, as implies measurements with high duty cycle and offers a possibility of precise shower direction reconstruction.

The two basic techniques, described shortly above, are discussed in detail in the following parts of this section.

2.3.1. Surface detector technique

Shower particles, falling at the Earth's surface, cover an area of many square kilometers. That is why, to measure them carefully, the detectors, situated on the distance of 1 - 2 kilometers from each other, should be arranged on a grid. That was realized, for example, at the Pierre Auger Observatory, in the way, that more than 1500 surface detector stations, spaced by the 1.5 km, were mounted at the area of 3000 km^2 (see section 3.1). Such array of detectors is called a surface detector (SD). Among the advantages of the surface detector are its almost 100% duty cycle, which enables the continuous detection, and a relatively simple determination of the exposure (i.e. of the integral over instantaneous aperture of the observatory detectors). Detectors of such type measure density of shower particles and time of their arrival at many points. Based on the measurements, conducted at several detectors, it is possible to reconstruct the direction and position of shower axis. Moreover, the number of particles in the shower can be estimated, giving a possibility for the further calculation of the energy of primary particle.

Using surface detector the lateral distribution of shower particles at the Earth's surface can be measured. As the lateral distribution depends on the shower energy, on the inclination of the shower axis, on the shower age and depth in the atmosphere, at which the shower is detected, the surface detector calibration must be based on detailed Monte Carlo simulations of the shower development.

Lateral distribution of density of shower particles $\rho(r)$ can be determined on the basis of the density of particles in many points (surface detector stations). *The lateral distribution function* (LDF) can be denoted as:

$$S(r) = S(1000) \cdot f_{LDF}(r), \qquad [Eq.\,2.16]$$

where $S(1000)$ is a signal, measured at fixed distance r (equal 1000 m in this example case) from the shower core (it is considered, that at $r = 1000$ m the fluctuations between individual showers of the same energy and zenith angle are minimal [52]); $f_{LDF}(r)$ is a parameterization function, normalized to $S(1000)$. In particular, $f_{LDF}(r)$ can be represented as a modified NKG function [53], [46]:

$$f_{LDF}(r) = \left(\frac{r}{r_{1000}}\right)^{\beta} \left(\frac{r + r_{700}}{r_{1000} + r_{700}}\right)^{\beta}. \qquad [Eq.\,2.17]$$

In this formula $r_{700} = 700$ m, β describes the slope of the LDF and depends on the shower zenith angle. Similar expression of lateral distribution function can be used in all experiments, which employ the surface detector technique. Particularly, this formula is applied to the measurements at the Pierre Auger Observatory (the example of the shower

LDF for the real event, registered at the surface detector of the Pierre Auger Observatory, is shown in section 3.1.1).

Thus, with the information about measured signal strength *S(r)*, it is possible to find the total number of shower particles at the ground level:

$$N \propto \int 2\pi r S(r) dr. \qquad [Eq. 2.18]$$

Thereafter the shower energy can be obtained, as it is proportional to the number of shower particles. In practice, it is done simpler, as:

$$E = A \cdot S_{38}^{B}, \qquad [Eq. 2.19]$$

where S_{38} is the expected signal of a shower at a reference zenith angle $\theta = 38^{\circ}$ at the distance of 1 km from the core, *A* and *B* are the energy calibration parameters.

2.3.2. Fluorescence measurements

When charged shower particles traverse the atmosphere, they excite nitrogen molecules, causing the isotropic emission of photons in the ultraviolet range $300 - 430$ nm (Fig.2.13). Such photons are known as *the fluorescence light*. Their isotropic emission makes possible the detection of extensive air shower irrespectively of the moving direction of the primary particle. For registration of the fluorescence light from air showers the optical fluorescence detectors are used. By means of these detectors, it is possible to observe extensive air shower at the large areas. So, UHECRs can be seen from the distances of even 30 km, in favorable atmospheric conditions. However, the measurements of the fluorescence light can only be conducted during the clear moonless nights, which constitute only about 10% of the time.

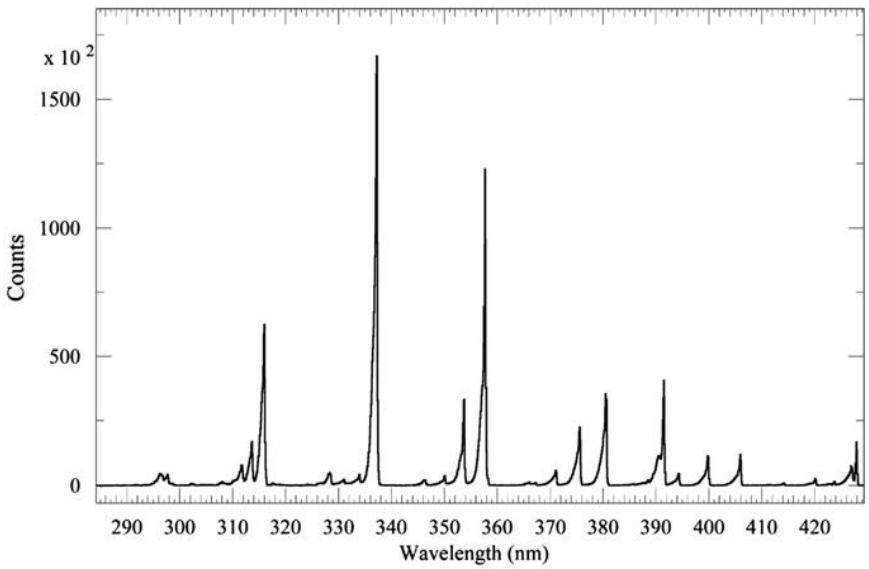

Figure 2.13: A measured spectrum of fluorescence light.

The technique of the fluorescence light detection is based on the Fly's Eye concept, used successfully for the first time in Utah at the Fly's Eye [54] and then in HiRes (High-resolution Fly's Eye) [55] experiments. So, for example, in the Fly's Eye experiment mirrors and photomultipliers were mounted in such a way, that the region of the sky observation was divided onto 880 pixels, at which the light from extensive air shower could be imaged. All pixels looked at their own directions of the sky, so that each pixel observed only small area of the sky, and some pixels might observe a certain region of the passing shower (Fig.2.14). Such triggered pixels formed a trace of the shower, mapping the shower trajectory on the telescope camera. Knowledge of the sequence of triggered pixels and triggering times allowed the determination of the arrival direction of the primary cosmic ray, shower axis and shower detection plane (see section 4.1.). In addition, this fluorescence detection technique made the possibility to trace out the longitudinal shower profile at all the visible atmospheric depth levels.

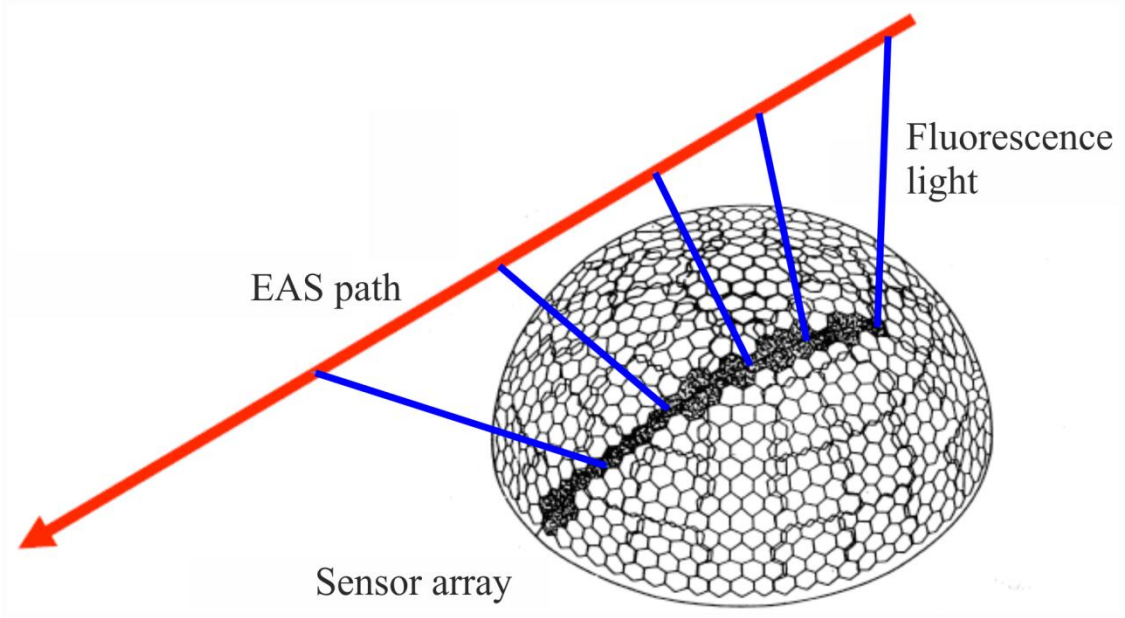

Figure 2.14: The geometrical layout of pixels as used in Fly's Eye experiment. The shower trace is shown by the shaded hexagons.

The Fly's Eye concept of the fluorescence detection technique is used by several experiments until now. In particular, it is one of the basic methods of detection at the Pierre Auger Observatory.

For estimation of the number of charged particles based on recorded fluorescence light, emitted in the air, the so-called *fluorescence yield* Y_γ should be known. This quantity determines the number of photons emitted per unit length l of a charged particle trajectory in

the air. It is usually measured experimentally in the laboratory conditions. It can be found from the relation [56]:

$$\frac{d^2N_\gamma}{dld\Omega} \cong \frac{Y_\gamma N_{CH}}{4\pi}\left[\frac{\text{photon}}{\text{sr m}}\right]. \qquad [Eq.\,2.20]$$

In this expression N_γ is the number of emitted fluorescence photons, Y_γ is a constant value of fluorescence yield, N_{CH} is the average number of charged particles in the shower. In such a way the intensity of the fluorescence light, emitted at each stage of shower development, is proportional to the average number of charged particles at that stage.

Alternatively, the amount of fluorescence light, generated in the atmosphere, is also proportional to the average energy, deposited along the shower path (*dE/dX*) as the result of ionization and excitation (so that, it can be assumed that average energy deposit is equivalent to average number of charged particles). It is also evident that the fluorescence yield should depend on the atmospheric conditions, in particular, on pressure *P*, temperature *T*, and atmospheric density of air ρ_{air} Therefore, the yield can also be represented as [57], [58], [59]:

$$Y_\gamma(\lambda) = \epsilon_\lambda(P,T)\frac{\lambda}{hc}\frac{dE}{dX}\rho_{air}\left[\frac{\text{photon}}{\text{m}}\right]. \qquad [Eq.\,2.21]$$

where $\epsilon_\lambda(P,T)$ is the fluorescence efficiency; λ is the photon wavelength, *c* is the speed of light and *h* is the Planck constant.

Looking at both formulas representing fluorescence yield *Eq.*2.20-2.21, it can be deduced, that the number of emitted fluorescence photons is proportional to the released energy:

$$N_\gamma \propto \frac{dE}{dX}. \qquad [Eq.\,2.22]$$

Therefore, it is possible to calculate the energy of cosmic ray primary particle (which is equal to the extensive air shower total energy) using fluorescence detection method. So, if E_C is the critical energy, X_0 – the radiation length in the air, N_{CH} – the number of charged particles, the cosmic ray energy can be calculated as:

$$E = \frac{E_C}{X_0}\int N_{CH}(X)dX. \qquad [Eq.\,2.23]$$

Although this formula is not used in practice, it shows that the measurements of fluorescence light, carried out at the fluorescence detectors, provide the nearly calorimetric estimation of shower energy.

Having the limited duty cycle, the fluorescence detection method is not as much effective as surface detector technique. However, it allows the rather precise estimation of

shower energy, using the calorimetric method, what is not accessible for the surface detectors. That is why, as the best method of extensive air shower detection the so-called *'hybrid' detection technique* was proposed, in particular, in the Pierre Auger experiment [2], [60]. This technique is represented by a combination of two complementary detection methods, which imply the employment of surface and fluorescence detectors (Fig.2.15). Simultaneous usage of these detectors at the observatory improves significantly the accuracy of measurements, as both detectors register the same shower by measuring the various quantities. The Pierre Auger experiment is discussed in more detail in the next section.

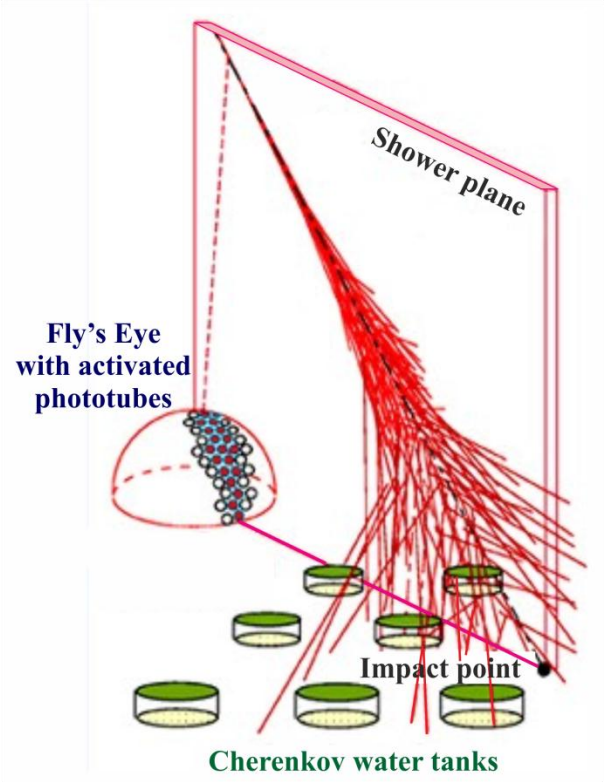

Figure 2.15: The schematic example view of hybrid detection technique of extensive air shower, represented by the detectors of two types: surface array (Cherenkov tanks) and fluorescence detector (Fly's Eye).

3. The Pierre Auger Observatory

The Pierre Auger Observatory [2] was built for the purpose of studying the UHECRs via measurements of the properties of extensive air showers. It is expected that the observations, conducted at the observatory, will help in explanation of the origin of UHECRs, primary particle identification, etc. These goals can be realized at the Pierre Auger Observatory as it has the exposure, which is much larger than in other cosmic ray experiments. Furthermore, the hybrid detection technique, used at the observatory, allows the shower registration, using different detection methods, and so provides the reliable, cross-checked data.

The hybrid detection technique, used at the Pierre Auger Observatory, is represented by two main types of detectors (surface and fluorescence). Using surface detectors (SD) it is possible to measure shower front at the Earth's surface, and find the lateral distribution and time dependence of shower particles, which reach the ground. Fluorescence detectors (FD) enable observation of shower development in the atmosphere and measurement of the longitudinal shower profile. By connecting two different measurement techniques, Auger hybrid detection system enables a very good calibration, and comparison of shower parameters. This technique allows also to reduce the systematic uncertainties of the single detection methods, and so to increase the measurement accuracy.

One of the main advantages of the Pierre Auger Observatory is its size. Being the largest detection system for UHECRs study in the world, it covers an area of 3000 km^2. Data collection started at the observatory at the beginning of 2004. The operation period of the observatory was planned at least for 10-15 years. So, starting from the beginning of data collection and up to the year 2012, the total exposure constitutes more than 23 500 km^2 sr yr. That means that the Pierre Auger Observatory has significantly larger exposure, than other cosmic ray observatories combined.

3.1. The instruments of the Pierre Auger Observatory

The Pierre Auger detection system [2] is situated in Malargüe (69° W, 35° S, 1400 m a.s.l.), Mendoza Province, Argentina (Fig.3.1). There are two types of detectors currently employed at the Pierre Auger Observatory, which have already been briefly discussed earlier. In addition to them, a radio detection technique, represented by the array of radio detectors, is being developed at the observatory. Besides different detectors, other instruments are located at the Pierre Auger Observatory. Some of them extend the

properties of the detectors (like the High Elevation Auger Telescope (HEAT)), others are responsible for the monitoring of the atmospheric conditions and aerosols at the area of observatory (such as weather stations, cloud cameras, etc.). The instruments of the Pierre Auger Observatory are discussed in more detail in the following section.

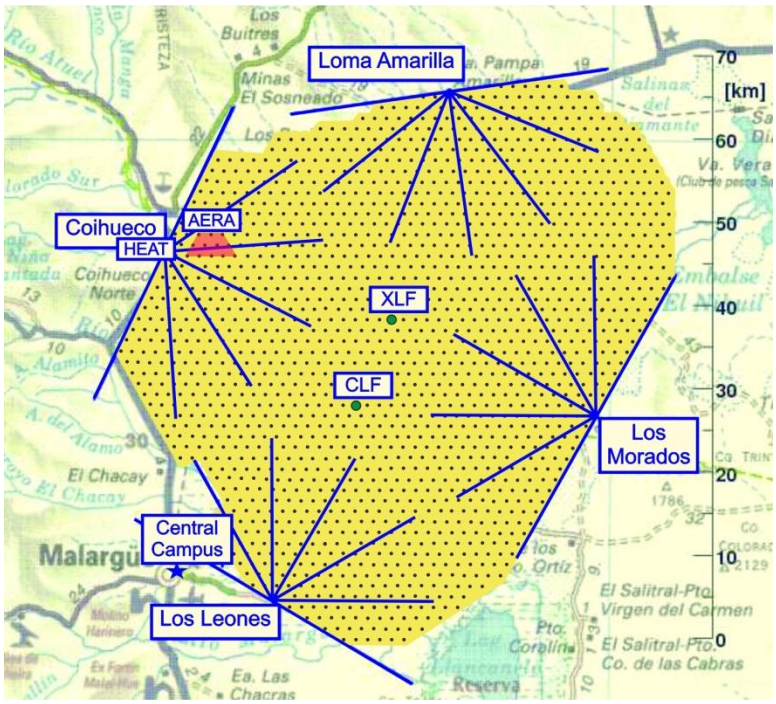

Figure 3.1: The Pierre Auger Observatory near the town of Malargüe. The positions of the instruments of the Pierre Auger Observatory are shown: the surface array detector stations (black dots), the fields of view of the fluorescence detector (FD) telescopes (blue lines), HEAT - High Elevation Auger Telescope (close to Coihueco FD), AERA - Auger Engineering Radio Array (pink region) and the atmospheric monitoring instruments Central and eXtreme Laser Facilities (CLF and XLF) are shown in the middle, while the others are situated mainly in the FD sites and so are not shown.

3.1.1. Surface array

The surface detector system [61] consists of 1660 water Cherenkov detector stations, arranged in a hexagonal grid on the distance of 1.5 km one from another, covering the total area of 3000 km^2. Each SD station (Fig.3.2) is a polyethylene plastic tank with 12 tons of purified water (water level inside the tank equals 1.2 meter). Each water tank encloses a Tyvek reflective liner that protects the water from contamination and ensures a uniform reflection of the Cherenkov radiation, produced by muons and electrons, traversing the water. Among other parts of SD station are: 3 photomultiplier tubes (PMTs), which record the Cherenkov light emitted by shower particles; electronics box for reading the signals from PMTs; communication antenna for sending the collected data to the Central Data

Acquisition System (CDAS) and GPS antenna for time and position determination; solar panel and battery box, used for power supply. The SD station photomultipliers monitor the water in the tank all the time and register the Cherenkov light, when the event comes to SD. The signal is further filtered and read out using the Flash Analog Digital Converters (FADCs) at 40 MHz. At the same time its arrival time is obtained by the GPS receiver. The information about the shower (the FADC signals and their time of arrival) is sent to CDAS, where the energy and direction of the primary cosmic ray is determined.

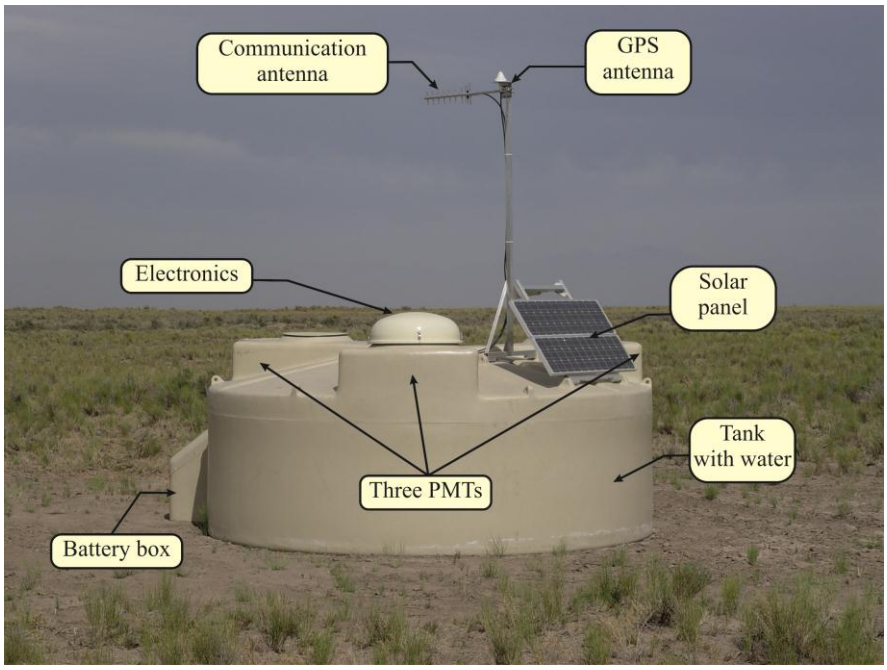

Figure 3.2: One of the SD stations of the Pierre Auger Observatory.

An example of the real Auger event, measured by SD is presented in Fig.3.3. The signal, coming to the array of SD stations, is shown in dependence on the time, distance and strength. In particular, colours of the individual circles at the grid of detectors (Fig.3.3a) denote the time of signal arrival at the station (from yellow (start of the signal detection) to red (last signal detected)). The size of the circles at the figure illustrates the strength of the signal. The dependence of the signal on the distance from the shower core $S(r)$ is represented by the lateral distribution of the signal (Fig.3.3b), calculated in VEM units, i.e. as the average signal deposited by a centered and vertically travelling high energy muon, traversing each SD tank. Shower particles are coming to several stations during a short time.

As it already was mentioned above, the duty cycle of the surface array is about 100% that makes possible collecting of the large ultra high energy event statistics. Therefore, large database of ultra high energy events, measured at SD array, can help much in determination of the shower parameters, and so in solving of the mysteries in UHECR physics.

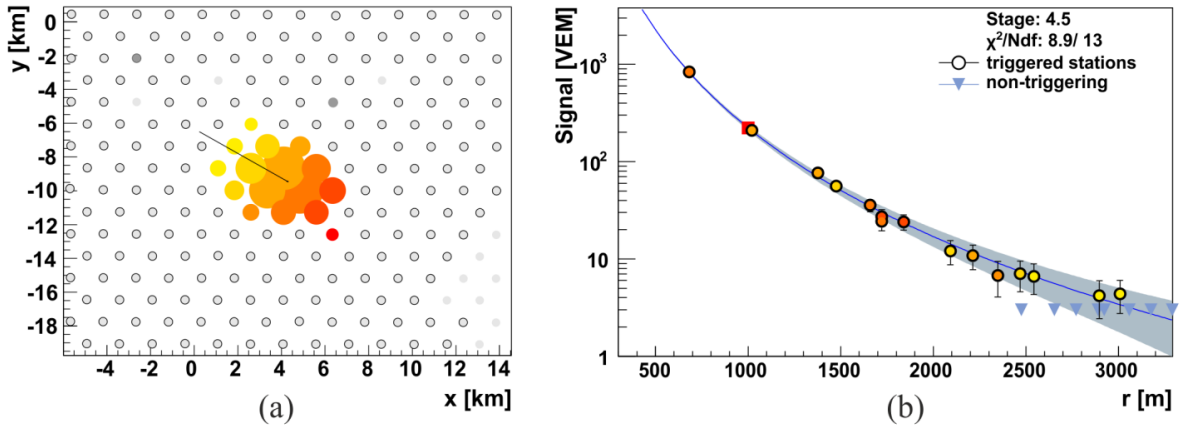

Figure 3.3: The real Auger event #201114608582 is shown at the image, representing the part of SD array (a). It has an energy $E \approx 5 \cdot 10^{19}$ eV, zenith angle $\theta = 42.7° \pm 0.1°$, azimuthal angle $\varphi = 143.9° \pm 0.2°$. The increasing size and changing colour (from yellow to red) of the circles at array correspond to the strength of the extensive air shower signal at each single station and to the arrival time of that signal respectively. The lateral distribution, represented by the signal value $S(r)$ vs. distance r, is shown in VEM units on the figure (b). The signal at 1000 m, indicated by a red square, equals to $S(1000) \approx 222.7 \pm 8.9$ VEM. The blue line fitted to the lateral distribution is a lateral distribution function, obtained from the NKG parameterization. Blue triangles at the right down corner of the picture mark stations with no signal.

3.1.2. Fluorescence detectors

The Auger FD system [62] consists of four FD sites, situated at the borders of the surface detector (Fig.3.1) and overlooking the whole SD array. They are: Los Leones (LL), Los Morados (LM), Loma Amarilla (LA) and Coihueco (CO) fluorescence detectors. Each such FD site contains six fluorescence telescopes (Fig.3.4a,b), which observe their own regions of sky with the size of 30° in azimuth and 2° - 30.6° in elevation, that constitutes the total field of view of FD site, equal 180° × 28.6°.

The inner structure of a FD telescope is presented in Fig.3.5a,b. When the shutter is opened, the light enters through the diaphragm with diameter 2.2 m. Using UV filter, most of the background light contamination (such as moonlight) is filtered out from the total light. After that the residual light is reflected by the spherical mirror (with the approximate size 3.5 m × 3.5 m) and focused onto the camera, located in the focal surface.

The large field of view of each telescope (30° × 28.6°) is obtained, using the modified Schmidt optics [63], which includes the diaphragm, corrector ring and a spherical mirror. Spherical optics makes possible observation of such a large field of view by focusing light from a wide range of directions on the focal plane. However, large spherical

aberrations arise during this process as the light is not focused on a single point, but on a caustic surface, leading to an extended spot on the focal plane. These aberrations become more significant with increasing of the part of the illuminated mirror surface, and therefore they have to be corrected. The diaphragm and corrector ring are responsible for the reduction of coma and spherical aberrations respectively. The diaphragm opening window limits the mirror area available for illumination, while the corrector ring compensates the increased spherical aberrations. The corrector ring lens, installed around the diaphragm, allows one to increase the effective light collection area of the telescope about two-fold, while maintaining a shower image size of 0.5° [64].

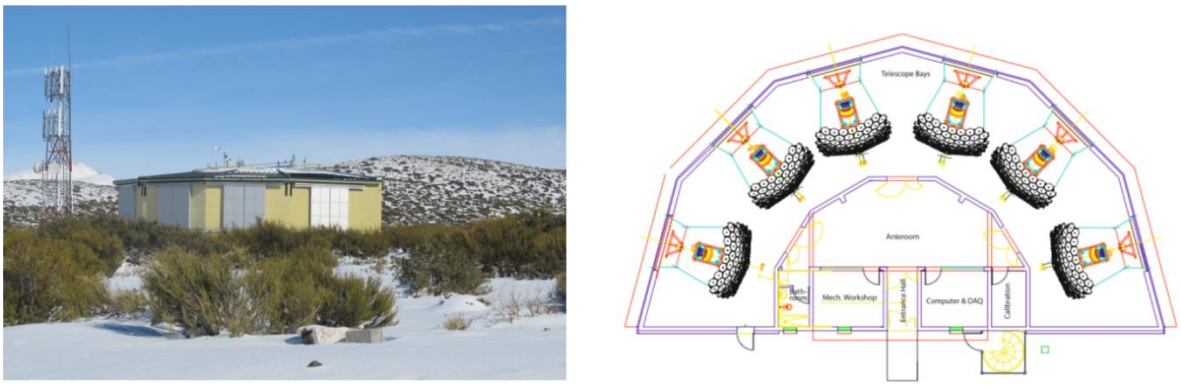

Figure 3.4: The real (a) and schematic view (b) of FD site at the Pierre Auger Observatory. The photo represents Coihueco FD. Six telescopes layout is shown at the schema.

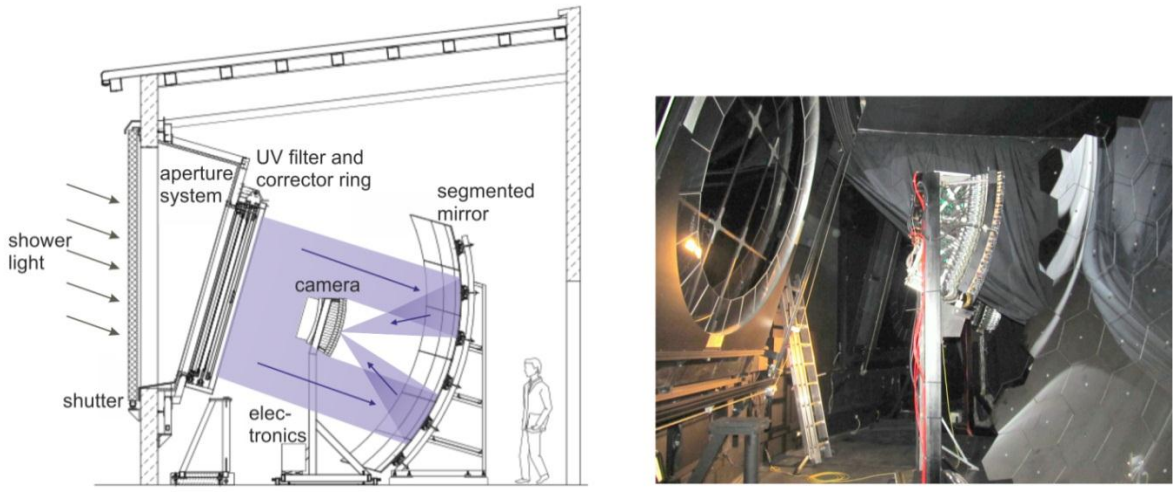

Figure 3.5: The inner schematic structure (a) and real view (b) of a fluorescence telescope at the Pierre Auger Observatory. The path of incoming photons is also shown at the scheme.

The FD camera (Fig.3.6a,b) is built of 440 pixels. Each pixel looks at its own direction, observing approximately 1.5° × 1.5° of the sky, as follows from its size, shown in

Fig.3.7. When shower light comes to the detector, the camera pixelizes the shower image and records the time and the amount of light, which comes to every pixel.

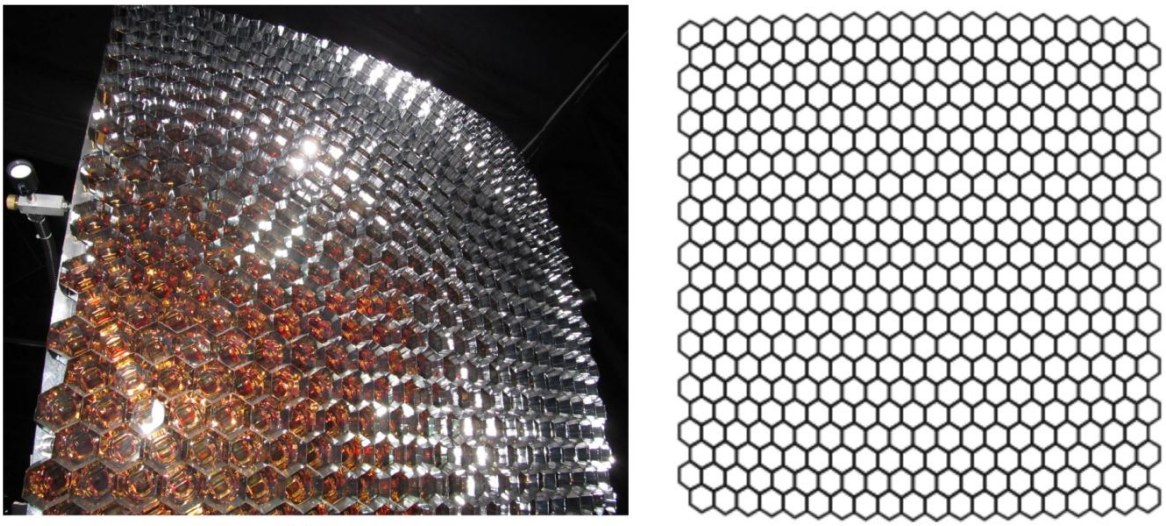

(a) (b)

Figure 3.6: Real view of the PMT camera of the telescope is presented on figure (a). Its schematic view (b) denotes that the camera consists of 440 pixels, arranged in a 22 × 20 matrix [62].

Each pixel has a hexagonal photomultiplier tube (PMT) (Fig.3.8). The camera PMTs have the light collection efficiency in the UV band, equal on average to 93% [62]. Such great efficiency is reached by installation of small light reflectors (“mercedes stars”) between the PMTs [65], that leads to the reduction of signal losses on the PMT boundaries.

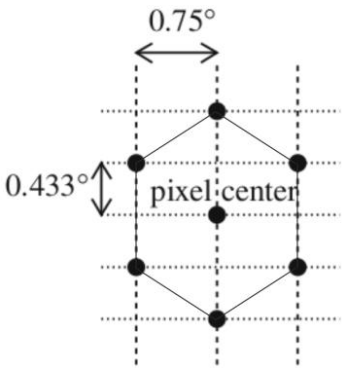

Figure 3.7: Schematic pixel size view.

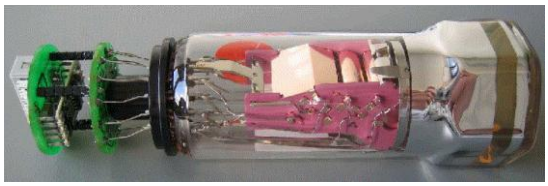

Figure 3.8: The photomultiplier tube (Photonis XP3062), which is used in the cameras of FD telescopes at the Pierre Auger Observatory.

Besides the listed FD parts, there are also electronic devices, responsible for data collection and processing. Thus, the main computers, located in each FD site, are used both for managing the signal identification scheme (also known as high level triggering process) and for storing the large volume of events raw data. The absolute timing information is assured by the GPS receiver. Each camera has its own data acquisition system (DAQ). Data

transfer to the Central Data Acquisition System (CDAS) is provided via a wireless communication link.

Air shower identification scheme, used at Auger FDs, is also of the special interest. It consists of 4 trigger levels [66], i.e. 4 steps, necessary for the correct event registration and including selection criteria for this purpose. The First Level Trigger (FLT) ensues with frequency equal 100 Hz, when the signal (measured in a single pixel and integrated over 10 time bins (1 time bin = 100 ns) to improve signal to noise ratio) exceeds a certain threshold of detection during 1 μs. For passing the Second Level Trigger (SLT) the previously chosen pixels should form a pattern of the definite shape (Fig.3.9). The Third Level Trigger (TLT) is activated for the verification of the event time structure. It is considered to be a software trigger operating on the telescope level. The last trigger is called the eye level trigger (T3), and is supposed to check the possibility of the quick rudimentary event reconstruction with determination of the direction and time of impact on the ground. After that, in order to enable the data readout and comparison with SD data the information is sent to CDAS.

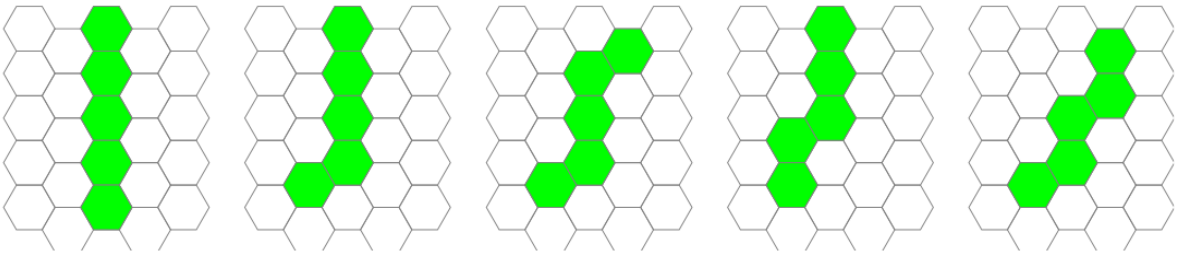

Figure 3.9: Basic topologic configurations, used by SLT at the Auger FDs [66].

For the purpose of conversion of the measured signal to the number of photons, the following procedure is commonly used in FD data analysis. After registration of the charge values of signal in the PMTs, the signal is digitized by the fast analog to digital converters (FADCs) with a frequency of 10 MHz in time bins of 100 ns [62]. This provides a time profile of the shower development in the atmosphere. Then, using the previously measured calibration constant [2], the FADC-traces can be transformed to the number of photons in the time interval. Shower profiles, built using number of photons determined in such a way, are presented in the next sections.

3.1.3. Other instruments of the Pierre Auger Observatory

Atmosphere monitoring instruments are also a necessary part of the Pierre Auger Observatory, as the atmosphere is variable, and therefore the special instruments are needed

to take into account its variability. Furthermore, the atmosphere itself forms a part of the detector system and so should be carefully monitored. As a shower develops in the air, the atmospheric parameters are of great importance for determination of shower characteristics. In particular, due to the fact that some fraction of the fluorescence photons is dissipated in the atmosphere and does not reach the detector, it is necessary to permanently monitor the density of aerosols in air, on which the scattering takes place. In addition, the monitoring instruments can help much in estimation of the influence of atmospheric effects (like clouds) on shower signal that can lead to reduction or even elimination of their impact on FD data. Among the instruments for atmosphere monitoring at the Pierre Auger Observatory are: weather stations, LIght Detection And Ranging station (LIDAR), atmospheric soundings (i.e. balloon sounding of the atmosphere), Central and eXtreme Laser Facilities (CLF and XLF), cloud cameras, optical telescopes - the Horizontal Attenuation Monitor (HAM) and the Fotometric Robotic Telescope for Atmospheric Monitoring (FRAM), and two Aerosol Phase Function Monitors (APFs). Specifics of the measurements, provided by these instruments, is briefly discussed further in this section.

Four weather stations are situated at the FD sites and two are in the central part of the observatory. For every five minutes they measure pressure, temperature, relative humidity and wind speed at the ground level.

Also for the measurements of vertical temperature and density profiles above Malargüe, the atmospheric sounding [67] was used. Helium balloons with radiosondes attached were launched several times per month and measure atmospheric properties at the height of up to 30 km. Currently, this procedure has been replaced by use of GDAS global data [68].

There are two laser facilities (CLF and XLF) in the middle of the surface detector array (Fig.3.1). They are used for measurements of the parameters (such as aerosol optical depth) of the aerosol component, responsible for the contamination of the atmosphere with dust and smoke particles. Each of these facilities is equipped with a pulsed laser, which generates a sequence of shots into the atmosphere. The laser light scattered in the air is registered further in all FDs [69]. Laser events, recorded by FD telescopes, give the information about the aerosol concentration at different altitudes.

There are also aerosol monitors (APFs), situated at Coihueco and Los Morados FD sites. These instruments include the Xenon flashers, which shoot horizontally in short distances in front of the FD eyes to observe scattered light over a large scattering angle

range [70]. Using these measurements, it is possible to find the Mie scattering phase function.

Additionally, for the purpose of aerosol studies, optical telescopes HAM and FRAM, located at Los Leones FD site, are used at the Pierre Auger Observatory. HAM lasers shoot horizontally from one FD building to another that allows measuring the horizontal attenuation length at the ground level. FRAM observes a set of known bright stars. Comparing the star brightness, obtained from these observations, with the catalogue value, it is possible to find the dependence of the light attenuation in the atmosphere with the wavelength [71]. Besides, FRAM is able to detect presence of clouds in the atmosphere.

The LIDAR [72] stations are located at each FD site of the Pierre Auger Observatory. Each station includes a pulsed UV laser with a wavelength of 351 nm and a 80 cm mirror. This system is capable to measure the atmospheric profile in any direction. Besides, during operation the LIDAR detects clouds, which are between the extensive air shower and the FD. The LIDAR stations are also used in measurements of atmospheric aerosols through backscattered light from the UV laser. In addition, the LIDAR can work in the shoot-the-shower mode: if a very high energy shower is detected, in short time the LIDAR is directed to scan the atmosphere crossed by this event.

Four infrared cloud cameras [73] are situated at the roofs of each FD site. A single camera has a field of view equal $45° \times 35°$. Every 5 minutes during data taking, the camera photographs the sky, looking at the FD field of view, and an estimate of the cloud coverage is made.

In such a way, the atmosphere studies, conducted all the time at the Pierre Auger Observatory, allow not only the monitoring of the atmospheric parameters, which influence the shower development, but also take into account the atmospheric fluctuations. Working together the instruments discussed above ensure the acquisition of a detailed information about atmospheric conditions, and so about important extensive air shower characteristics, that helps much in studies of UHECR properties.

There are several upgrades, being implemented currently at the Pierre Auger Observatory. The purpose of their implementation at the observatory is to increase the capability of the detectors, to develop new detection techniques, etc.

One of the enhancements for the Pierre Auger Observatory detectors is the High Elevation Auger Telescope (HEAT) [74]. It is situated close to Coihueco FD building (Fig.3.1) and contains the identical telescopes, as FD has. As it can be deduced from its name, high elevation telescope extends the FD field of view in elevation, so that its size is in

the range from almost 30° in Coihueco FD up to 60°. Such large field of view allows the registration and study of the low-energetic extensive air showers, which develop high in the atmosphere. Furthermore, the X_{max} measurements can be done at HEAT for the close showers with maximum outside the FD field of view.

Another extension of the Pierre Auger Observatory is AMIGA, i.e. Auger Muons and Infill for the Ground Array [75]. It contains 85 detector pairs, which consist of the water-Cherenkov detectors and muon counters. These detectors are situated near the Coihueco FD site at the area of 23.5 km^2, forming in such a way an infill array inside the Auger SD array. This infill array in its turn contains 2 sub-arrays. One sub-array includes 61 detectors, located at the distance of 750 m one from another; the rest 24 detectors constitute the other sub-array, and have a spacing of 433 m. The infill array allows more precise measurements of the muonic shower component, providing a detailed study of the showers with the energy 0.1 – 10 EeV.

Besides the discussed extensions the detectors of the third independent detection type are being developed at the Pierre Auger Observatory. They are radio detectors, which form the so-called Auger Engineering Radio Array (AERA) [76] (Fig.3.1). The main purpose of arrangement of these detectors at the Pierre Auger Observatory is to develop the radio detection technique. AERA occupies the area of 20 km^2, counting 160 detector stations. The detectors of this new type can measure the extensive air shower radio emission with radio antennas at each stage of shower development. Radio detection arises as a very promising measurement technique, which can provide shower reconstruction with very good angular resolution. The duty cycle of radio detectors is almost 100%. So, they can supply the Auger Observatory with the complementary information on energy and nature of the cosmic ray primaries.

3.2. Specifics of the hybrid detection technique

The main feature of the Pierre Auger Observatory is the hybrid detection method, which employs two independent detector types. The air showers, measured simultaneously by the surface and fluorescence detectors, are known as hybrid events. Taking advantage of both detection techniques, the properties of hybrid events can be measured independently, giving the opportunity to obtain the more accurate results.

Due to the layout of the FDs at the Pierre Auger Observatory, among hybrid events there are extremely high energy showers, which can be registered at the same time by

several FDs (Fig.3.10). Such showers are called stereo hybrid events, whereas events, detected by one FD, are mono hybrid events.

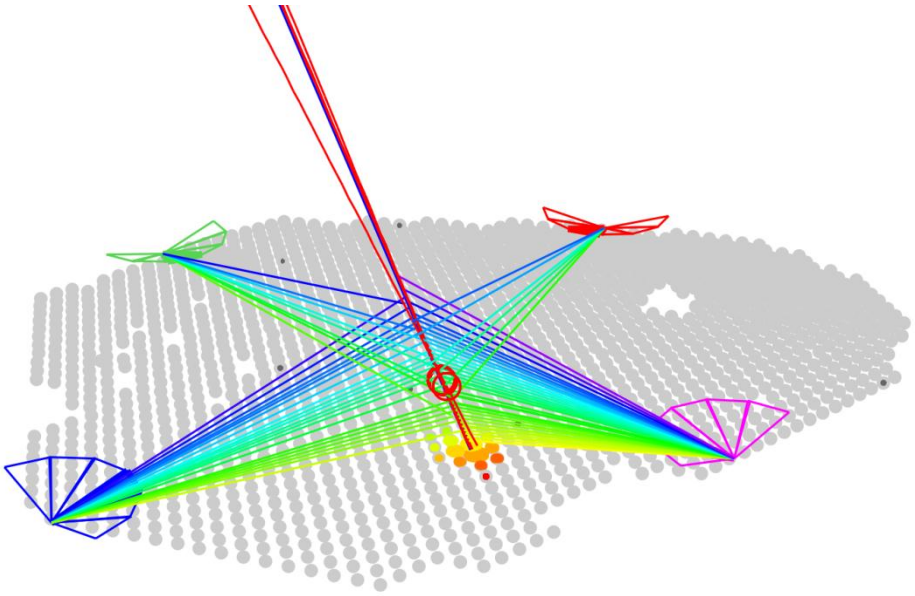

Figure 3.10: The example of real hybrid event #201114608582, recorded in May 2011 at the Pierre Auger Observatory, is shown at the picture together with schematic views of the four FDs and SD array. Presented event is a very rare, so-called, 'golden' event, which was register simultaneously by the all four FDs. Its characteristics together with SD view and lateral profile were specified in section 3.1.1. The picture includes slightly inclined vertical lines, which define the shower axis, reconstructed separately by the surface (blue line) and fluorescence (red lines) detectors. Lines, arising from the axis in the direction to the FDs, represent the signal, coming to the telescopes, depending on the time of arrival on FD (in the spectrum from violet colour (early time) to yellow or red one (latest registered time)).

The reconstruction procedure, appropriate for hybrid showers, is another distinctive feature of the detection technique, used at the Pierre Auger Observatory. In particular, it includes the reconstruction with the fluorescence detectors taking into account the information from the surface array, and consists of several important steps. They are: calibration and pulse determination; reconstruction of shower detector plane (SDP) and shower axis; finding the time fit; estimation of shower light at the aperture; and, finally, reconstruction of the shower profiles and energy. These steps of shower reconstruction procedure are described in more detail in section 4.1, particularly on example of the real hybrid event.

One of the consequences of the hybrid reconstruction procedure is a possibility of the precise estimation of shower energy by means of SD and FD detection methods (as it was shown in section 2.3). Thereafter, one more feature of the hybrid detection technique

arises; it is a cross-calibration of shower energy between the fluorescence and surface detectors. For this purpose the correlation between the measurements of fluorescence energy E_{FD} and shower signal $S(1000)$, recorded in SD at 1000 meters from shower core, should be carefully studied [77]. To adjust for the zenith angle dependent attenuation of signal, $S(1000)$ is converted to S_{38} value [9], which represents the expected signal at 1 km from the core of a shower at the zenith angle 38º.

At the same time, the energy E_{FD} of the event is known due to the fluorescence telescopes. The correlation between E_{FD} and S_{38} can be derived by fitting a power law to (S_{38}, E_{FD}) pairs of hybrid events (Fig.3.11).

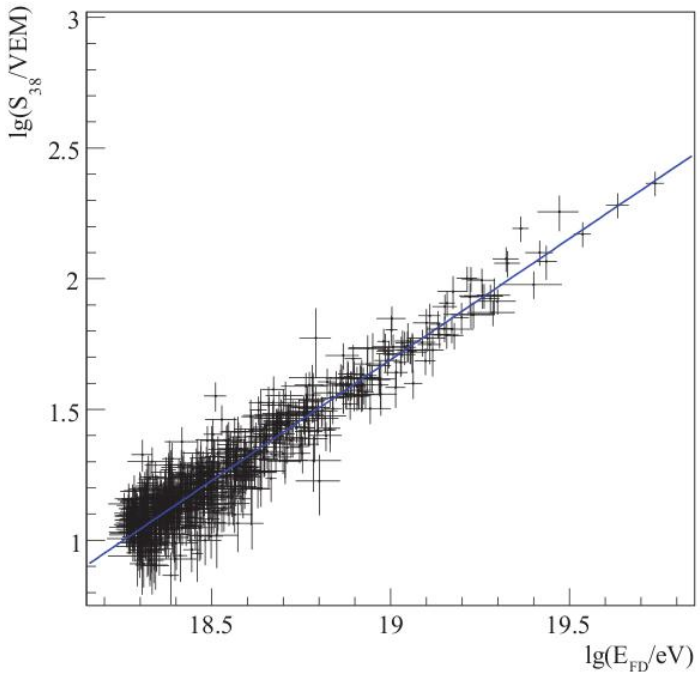

Figure 3.11: Correlation between shower signal S_{38}, measured by SD array, and energy E_{FD}, determined by FD, is shown. The data points represent the energies, obtained for hybrid events. The blue line denotes the best fit to the data [9].

So, the energy calibration can be obtained from the hybrid events dataset. Using this cross-calibration it is possible to estimate the energy of events, seen by one technique and unavailable for detection by another one (such as daytime events, which are unavailable in FD).

3.3. Main results of the Pierre Auger Observatory

One of the great advantages of the Pierre Auger Observatory is the unprecedentedly large statistics of UHECRs that allows obtaining more precise cosmic ray characteristics,

than it is done in other experiments, and consequently can greatly help in solving the mysteries of UHECR physics.

Thus, in 2008 the Pierre Auger Observatory reported the measured cosmic ray spectrum with a visible confirmation of the GZK-cutoff [9]. That energy spectrum was found for 20000 events with energy values starting from $2.5 \cdot 10^{18}$ eV. Further observations of energy spectrum at the Pierre Auger Observatory, using hybrid detection technique, confirmed that results [10]. Thus, due to the high statistics such spectrum features as the ankle ($\sim 10^{18.6}$ eV) and the GZK suppression (above $10^{19.7}$ eV) are well visible at the updated spectrum version (Fig.3.12). Furthermore, the shape of Auger energy spectrum is in a good agreement with the correspondent data from other experiments (Telescope Array, HiRes), despite the different energy scale of these experiments.

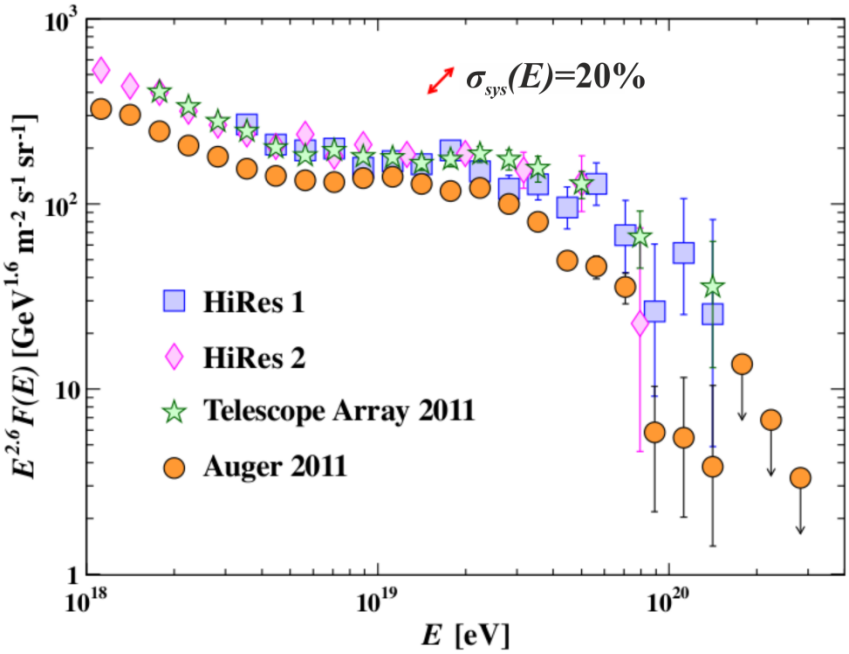

Figure 3.12: Recent energy spectrum measured at Auger Observatory in comparison to measurements, provided by Telescope Array and HiRes detectors [19]. The systematic uncertainties of the energy scale, indicated by arrows at the figure, are of the order of 20%. The differential cosmic ray flux is multiplied by $E^{2.6}$.

As it was discussed in section 2, the measurements of the primary cosmic ray particle type depend on the longitudinal profile and shower maximum estimation [27]. That is why changes of the average depth of the shower maximum and its *RMS* with energy are carefully studied at the Pierre Auger Observatory (Fig.3.13). In particular, according to measurements of $\langle X_{max} \rangle$ as a function of energy, the elongation rate (i.e. the dependence of the mean X_{max} on the logarithm of the energy) starts changing its value in the energy region

~ $10^{18.35}$ eV [78], which is close to the ankle. These results rather point out at the mixed composition at all energies (see Fig.3.13). However, as statistics of the events with energy above $4 \cdot 10^{19}$ eV is still insufficient, this result needs more studies. In addition, Monte Carlo simulations provided using different hadronic interaction models, give large uncertainties for expected values of elongation rate. So, the mass composition at the highest energies still is uncertain.

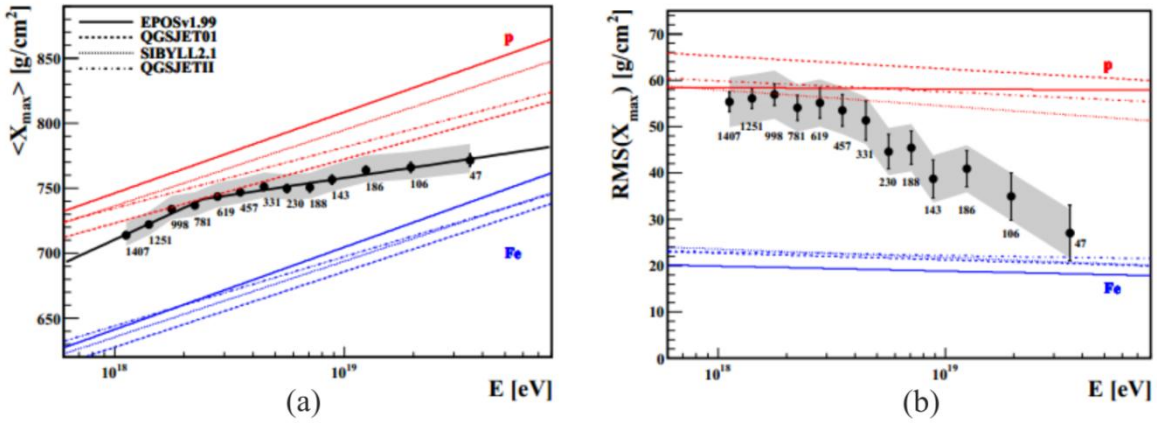

Figure 3.13: Average depth of shower maximum $\langle X_{max} \rangle$ (a) and *RMS* (X_{max}) (b) vs. shower energy are shown. The number of events (points) in each bin is indicated together with systematic uncertainties, denoted as a band. The limits of predictions for proton and iron primaries for several hadronic interaction models (EPOS, QGSJET01, SIBYLL, QGSJETII) are presented [79].

In [80] the Pierre Auger Observatory reported anisotropy in the arrival directions of UHECRs, based on the Auger data up to the end of August 2007. As a result of this analysis, a correlation with positions of active galactic nuclei in the Véron-Cetty and Véron (VCV) catalog was found. This correlation was observed for events with energy above 55 EeV and with angular separations of less than 3.1° from AGNs located closer than 75 Mpc from the Earth. The degree of the correlation with AGNs, observed at that time, was 69%.

The later analysis [81], carried out based on the Auger events up to the end of December 2009, increased number of events from 27 to 69 and revealed that the UHECRs correlating fraction with nearby AGN directions equals to 38%, while 21% is expected if cosmic rays were isotropic. The correlation between the 69 arrival directions of CRs and AGNs in the VCV catalogue is illustrated in Fig.3.14.

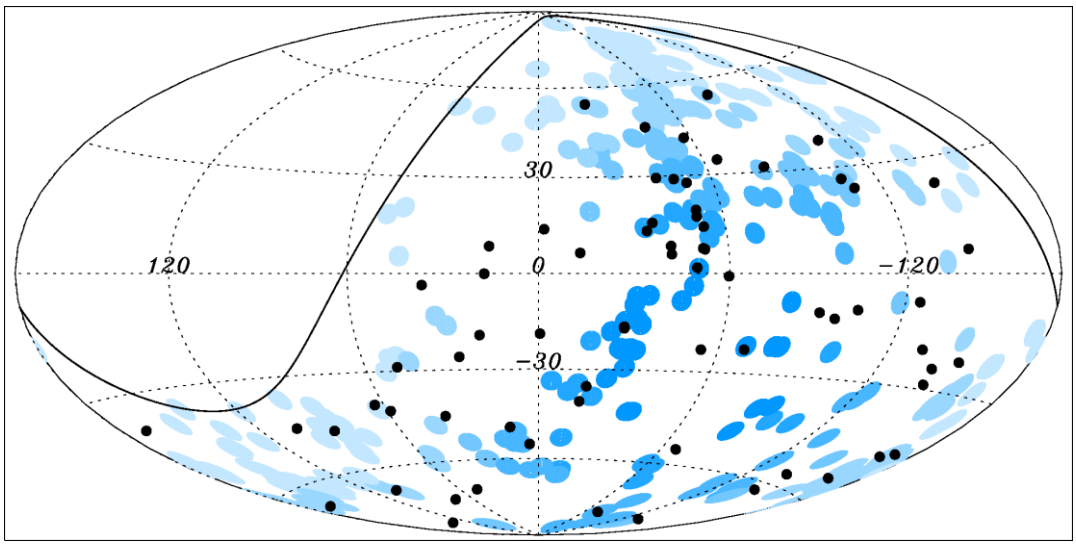

Figure 3.14: The 69 arrival directions (black dots) of cosmic rays with energy above 55 EeV and the positions of nearby 318 AGNs (blue points, where darker blue colour indicates larger relative exposure), according to the VCV catalogue, are shown at the map. The objects are plotted in galactic coordinates. The solid line draws the border of the field of view for the southern site of the Pierre Auger Observatory for zenith angles smaller than 60° [81].

Some correlations can be explained by existence of a possible source in the explored region of the sky – the radiogalaxy Centaurus A, situated at the distance of 3.8 Mpc. There is a significant number (about 12 from 69) of UHECRs with arrival directions pointing in that region (Fig.3.15), while arrival directions of 2 of them seem to correlate with the nucleus position of the radiogalaxy.

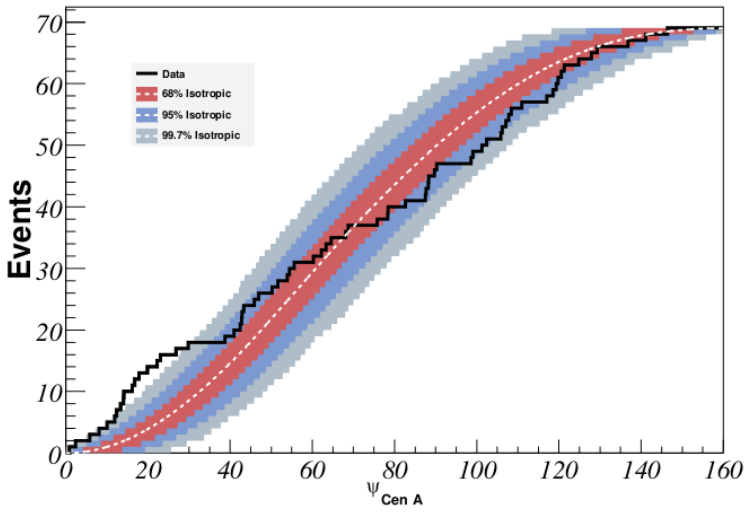

Figure 3.15: The number of cosmic ray arrival directions as a function of angular distance from Centaurus A. For an isotropic cosmic ray flux the expected dispersion is shown in different ranges (68%, 95%, and 99.7%) [81]. The excess in data above isotropic expectations is represented by the 13 arrival directions within 18º from Centaurus A.

It is still unclear, whether the UHECRs from Centaurus A really originate from this region, or from other close sources. This problem needs more sufficient statistics of UHECRs, which the Pierre Auger Observatory is able to supply, and so have a perspective to be solved in future.

The Pierre Auger Observatory is now running smoothly after complete installation of all the necessary components. Large statistics of events allows conducting of the precise measurements of the UHECR spectrum with GZK-cutoff, as well as provides the detailed study of chemical composition and arrival directions.

4. Shower reconstruction and Monte Carlo simulation

A shower reconstruction procedure, together with shower modeling and simulation of detector response, needs to be described by computational methods. This is done in the Offline software framework, designed within the Pierre Auger Collaboration [82]. Its general purpose is to supply the researches with good computing tools for analysis of the data collected at the observatory.

The structure of the Offline software package includes three main parts (Fig.4.1). They are connected with each other by means of a centralized mechanism, which consists of a collection of configuration files.

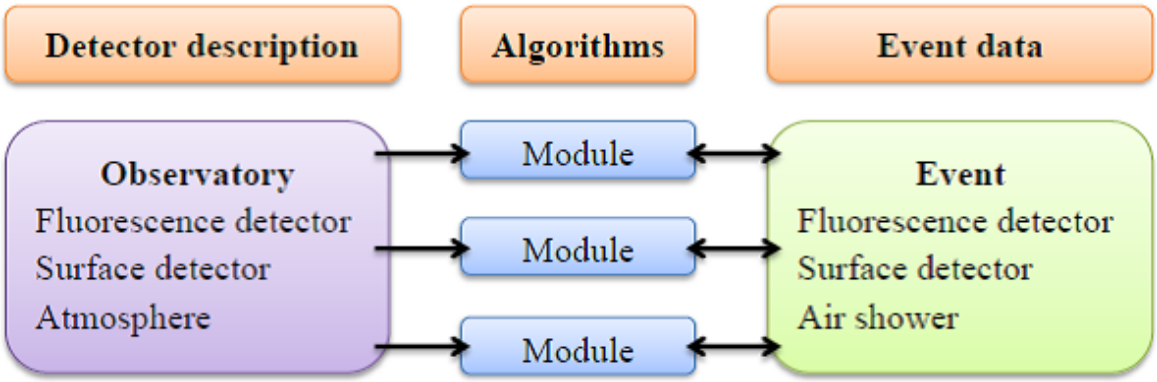

Figure 4.1: The structure of the Offline software framework.

The three component parts of the framework include:

- The detector description consists of a read-only information about detector performance at a given time. In particular, this contains details of the configuration, size and status of the SD and FD detectors, uptime information (the sum of the time intervals from the periods, when a fluorescence telescope was successfully operating, giving the good data for physics analysis), and data from atmospheric monitoring. The static information (about the detectors, for example) is stored in XML-files; relatively slowly varying data (like changes of the atmospheric conditions) are saved in MySQL databases. During work of the program the requested information is passed to a manager of modules, responsible for extraction of specific detector characteristics from data source;
- The algorithms, needed to provide objective data analysis, are arranged in processing modules, saved as the XML-files. A collection of modules can be assembled and sequenced, using instructions defined by the user in a special file (ModuleSequence.xml). The changes in modules can be done by means of a bootstrap file (bootstrap.xml);

- The event structure is built in the process of data analysis, using the processing modules of the program. They allow obtaining of raw, calibrated, reconstructed and Monte Carlo data for every Auger event.

The Offline software package is extremely flexible; it gives the possibility to use a combination of modules, appropriate for the conducted analysis.

The C++ language is used for code implementation in the Offline framework. The analysis output is recorded in a ROOT [83] based file format, called the Advanced Data Summary Tree (ADST) [84]. This format was specially designed for summarizing the resulting output of event reconstruction and simulation, done by means of Auger Offline software. It contains event variables from FD and SD, needed for physics analysis. The analysis, provided in the sections 5 and 6, is based on the data obtained from such kind of outputs.

As one of the main goals of this work is to measure the lateral shower profile using the optical image on FD camera, the stress in this analysis is made on the FD part of the hybrid study. That is why mainly the steps of FD reconstruction and simulation procedures are described in detail in the following sections. These procedures are implemented into the Offline software, and so can be applied to events from the Pierre Auger Observatory.

4.1. Shower reconstruction procedure

The main purpose of hybrid reconstruction is the extensive air shower energy estimation, based on the data collected by FD, and considering the information from the SD array [62]. The standard procedure of shower reconstruction consists of several steps (as it was briefly discussed in section 3.2). All of them are implemented in the Offline software as modules, arranged in the proper sequence (Appendix A1). The steps of the reconstruction procedure include the following:

1. Calibration of FD (responsible module – FdCalibrator). The detector calibration is needed in order to determine the number of photons, measured by the fluorescence detector. After subtraction of the background noise from the total measured light (see also section 5.2), the signal in ADC-counts (i.e. electric pluses) should be converted into number of photons at the aperture (photon traces). It is done for each pixel by multiplying the ADC-trace (i.e. the signal in ADC-counts as a function of time) by the calibration constant at the appropriate time interval. These constants depend on time and are determined for each telescope during the detector calibration procedure [62].

2. Pulse reconstruction (module – FdPulseFinder) is represented by an

algorithm which determines the true pulse of the shower. Using this algorithm, the calibrated ADC-traces are obtained at each 100 ns, by maximization of the signal over noise. A signal-to-noise ratio can be calculated as:

$$S/N = \frac{S(\Delta t)}{\sqrt{\Delta t} \times RMS}, \qquad [Eq.\,4.1]$$

where Δt – is the difference between the last and the first time moments, at which signal S arrives at the FD; $S(\Delta t)$ – is a total signal, measured at the correspondent time interval Δt, RMS is the variation of the ADC-trace baseline. Only S/N values greater than 5 are chosen for further analysis, that allows elimination of the accidental noise, caused by background radiation.

3. Shower detector plane (SDP) reconstruction (Offline module – FdSDPFinder) is a first step of the shower geometry reconstruction (Fig.4.2). SDP is a plane defined by the pixels of the fluorescence telescope. Each pixel of the telescope camera looks at its own direction, observing a certain region of the sky. Knowing the directions of a set of pixels which receive light from the shower, it is possible to determine the SDP by minimizing the function:

$$Q^2 = \sum_i \omega_i [\vec{p_i} \cdot \vec{n}]^2, \qquad [Eq.\,4.2]$$

where ω_i is the total integrated signal found in pixel i; $\vec{p_i}$ is a geometrical pointing direction of a pixel i corresponding to the angle χ_i; $\vec{n}$ is a searched vector normal to the SDP. When the SDP is determined, the shower axis can be found.

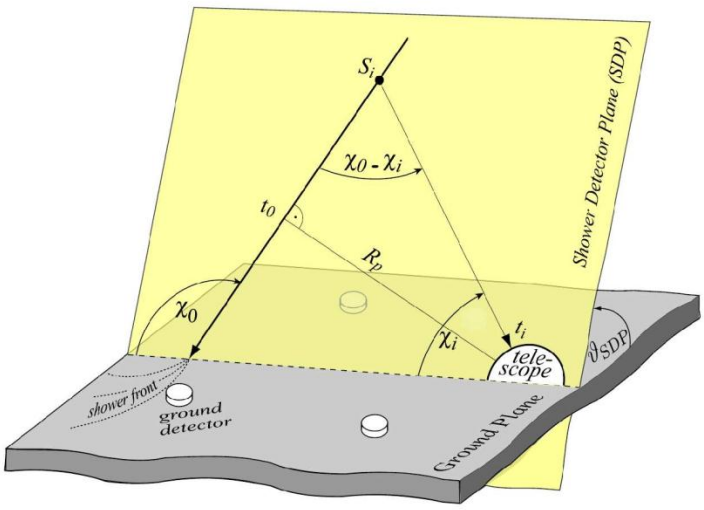

Figure 4.2: Schematic illustration of the shower geometry reconstruction [85]. Hybrid SDP is reconstructed using the shower trace image at the FD camera. Shower axis can be determined, knowing the timing and angular information for each pixel from shower trace, as well as using data from SD station.

4. Shower axis reconstruction within the SDP (module – FdAxisFinder) is the second step of extensive air shower geometry reconstruction. The SDP intersects the telescope camera, matching the triggered pixels. To find the position of shower axis within the shower detector plane, the following function should be minimized:

$$\chi^2 = \sum_i \left(\frac{t_i - t_i^{meas}}{\sigma(t_i)} \right)^2, \qquad [Eq.\,4.3]$$

where t_i^{meas} indicates the average measured time of shower light arrival to the field of view of pixel *i*, $\sigma(t_i)$ is an error, corresponding to the expected time t_i of pulse for pixel *i*. This time t_i (see Fig.4.2) can be given by:

$$t_i = t_0 + \frac{R_p}{c} \tan\left(\frac{\chi_0 - \chi_i}{2}\right), \qquad [Eq.\,4.4]$$

with R_p – the perpendicular distance of closest approach from the shower to the detector (also known as an impact parameter, determining the shower core), t_0 – time, at which shower front reaches the position of closest approach, χ_i – a pixel elevation angle, defining the direction of each pixel *i* projected onto SDP, χ_0 – angle between the shower axis and vector pointing from detector to shower landing point, *c* – velocity of light. The best fit of parameters χ_0, R_p, t_0 determines the shower axis.

The time fit can be more precisely found using the hybrid reconstruction (HybridGeometryFinder module). If the timing information from only a single SD station is additionally used in the reconstruction, the accuracy of event geometry reconstruction is much better, than that obtained by SD or FD independently. The estimation of the expected trigger time of the SD station can be given by:

$$t_i^{meas} = t_0 + \frac{1}{c} \vec{R} \cdot \vec{k}, \qquad [Eq.\,4.5]$$

where $\vec{R}$ is the position of the Cherenkov detector station with respect to the FD eye, $\vec{k}$ is the shower direction. So, using this timing information, the axis direction and the core position of the shower can be reconstructed.

5. Calculation of the light flux at the aperture (module – FdApertureLight). The special procedure is used at this step of shower reconstruction to estimate the total light received at the aperture of the fluorescence telescope. It includes a signal-to-noise maximization algorithm. This algorithm, first of all, implies the determination of the optimal width ζ of shower image on the camera (i.e. the optimal ζ angle, defined as the angle between the viewing direction of a pixel and the position of the shower on the camera (Fig.5.7a)). After that the integration of the signal from pixels inside the circle of radius ζ

allows us to obtain the number of photons at the telescope aperture as a function of time $N_\gamma(t)$.

6. Longitudinal shower profile and energy reconstruction (module – FdProfileReconstructor). As both the shower geometry and amount of light at the detector aperture have already been determined, it is possible to reconstruct the emission of shower light from the atmospheric layers, visible to FD. The number of photons collected in the FD aperture as a function of time $N_\gamma(t)$ is proportional to amount of light deposited by the shower particles along their path in the air as a function of slant depth $N_\gamma(X)$. In such a way, a longitudinal shower profile (see section 2.2.1) can be measured.

During such a reconstruction procedure several kinds of light are taken into account. They include the isotropically emitted fluorescence light, the Cherenkov light component, and scattered light from these contributions [86].

The Cherenkov radiation is emitted in a narrow cone along the direction of a particle. However, this kind of light covers a considerable angular range on its way with respect to the shower axis, because some charged particles are deviated from the primary particle direction due to multiple scattering. Therefore, two Cherenkov light components with different nature are usually distinguished: the forward direct and scattered light. Moreover, the scattered Cherenkov light consists of the Rayleigh (photons, scattered on particles smaller than the wavelength of fluorescence light) and Mie (photons scattered on larger particles, such as dust) components (Fig.4.3).

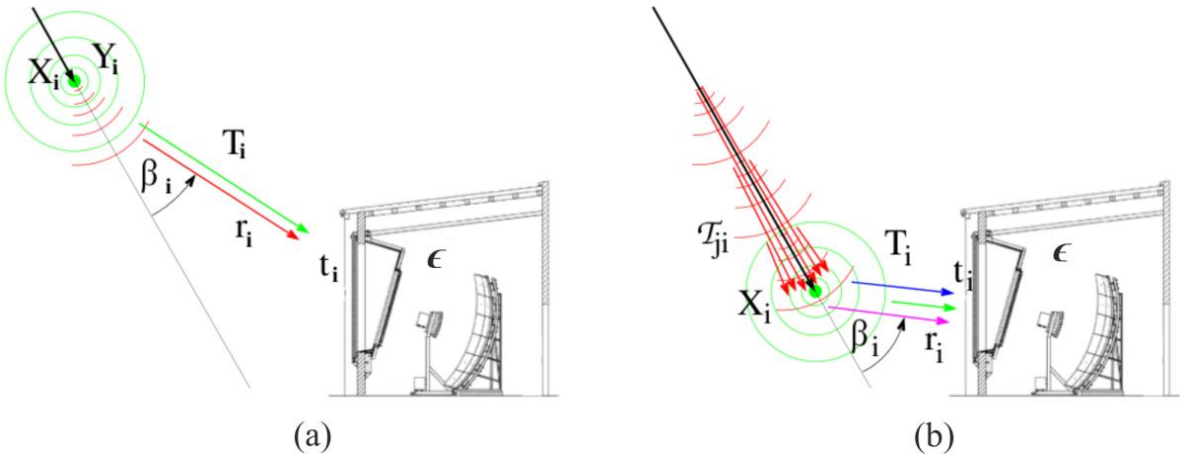

Figure 4.3: The flux of shower light, which comes to the FD, is composed of several direct (a) and scattered (b) components. They are shown by different colours at the picture: isotropic fluorescence light (green), forward beamed direct Cherenkov light (red), Rayleigh-scattered Cherenkov light (blue), Mie-scattered Cherenkov light (magenta) [86]. All these light contributions should be taken into account during shower profile reconstruction procedure.

The multiple scattering of light is supposed to occur in the atmosphere during propagation. This process describes the motion of photons, scattered on the aerosols or air molecules, instead of propagating along the direct path from the shower core to the telescope. Also some photons, which should not be in the telescope field of view, can be scattered back to the telescope and thus they may increase the signal. That is why it is important to add or subtract the scattered light to the total light flux correctly, to obtain the precise model of the shower signal.

Each of the mentioned contributions can be represented by the relations which include the fluorescence yield. Particularly, the non-scattered direct fluorescence light can be given by:

$$N_\gamma^f(X_i) = Y_i^f \frac{dE_i}{dX} \Delta X_i, \qquad [Eq.\,4.6]$$

where ΔX_i is the interval of slant atmospheric depth, Y_i^f – the fluorescence yield (i.e. the expected number of fluorescence photons at slant depth X_i), and dE_i/dX – the energy, deposited by the extensive air shower charged particles, which covered the distance ΔX_i along the shower axis. The direct Cherenkov light can be represented by

$$N_\gamma^c(X_i) = Y_i^c N_e \Delta X_i, \qquad [Eq.\,4.7]$$

with Y_i^c – the expected number of Cherenkov photons at X_i, N_e – the number of the electrons and positrons with energy larger than the threshold energy needed for Cherenkov light production.

As shower light, which comes to the detector, is scattered in the atmosphere (Rayleigh and Mie scattering), only some its part can reach the FD. Being limited by the telescope aperture A, the registered direct fluorescence light can be calculated as:

$$y_i^f = \frac{A\epsilon T_i}{4\pi r_i^2} N_\gamma^f(X_i), \qquad [Eq.\,4.8]$$

where T_i is a light transmission factor, r_i is a distance between the light emission point and the FD, ϵ – the light detection efficiency dependent on the UV filter transmission, mirror reflectivity and PMTs efficiency.

Correspondingly, the direct Cherenkov light, registered in the FD, can be described as:

$$y_i^{cd} = \frac{A\epsilon T_i}{4\pi r_i^2} f_c(\beta_i) N_\gamma^c(X_i), \qquad [Eq.\,4.9]$$

with $f_c(\beta_i)$ – a fraction of direct Cherenkov light, emitted in a solid angle β_i (Fig.4.3).

On the other hand, as the Cherenkov photons move forward along the shower axis,

an intense Cherenkov light beam can be formed along the shower (Fig.4.3b), so the possibility of detection of scattered Cherenkov light also should not be neglected. Therefore, the number of Cherenkov photons in the beam can be calculated at certain depth X_i as:

$$N_\gamma^{c,beam}(X_i) = \sum_{j=0}^{i} \tau_{ji}\, Y_j^c \Delta X_j N_e(X_j), \qquad [Eq.4.10]$$

where τ_{ji} – is an attenuation coefficient, including the fact that the number of Cherenkov photons at the depth X_i corresponds to amount of the Cherenkov light, emitted from the previous stages of shower development X_j. Hence, the scattered Cherenkov light, coming to the FD aperture, can be estimated as:

$$y_i^{cs} = T_i f_s(\beta_i) N_\gamma^{c,beam}(X_i), \qquad [Eq.4.11]$$

with $f_s(\beta_i)$ – a fraction of scattered Cherenkov light, emitted in the β_i angle.

The total light, observed at the detector aperture, can be described as:

$$y_i = y_i^f + y_i^{cd} + y_i^{cs} + y_i^{ms}, \qquad [Eq.4.12]$$

and includes the multiple scattering component y_i^{ms}.

Shower energy can be calculated based on the amount of light, registered at the telescope aperture. This is possible knowing the energy deposited dE/dX_i by charged shower particles in the atmosphere, which corresponds to the summarized deposited energy of a single shower electron, multiplied by the number of charged particles $N_e(X_i)$ at the atmospheric depth X_i. Thus, the total deposited shower energy can be given by

$$\frac{dE}{dX_i} = N_e(X_i) \int_0^\infty f_e\,(E, X_i) \frac{dE}{dX_e}(E, X_i) dE, \qquad [Eq.4.13]$$

where function $f_e(E, X_i)$ represents the normalized electron energy distribution (this function is universal and depends on the shower age parameter only [87]), $dE/dX_e(E, X_i)$ is the energy loss of a single electron with energy E.

It happens often that due to the close distance to the detector or large elevation angle, not all stages of shower development are observed within the FD field of view, so that the shower longitudinal profile is cut. That means that a part of shower signal is lost. To avoid this loss, the parameterization of longitudinal profile, using Gaisser-Hillas function (see section 2.2.1), is usually applied. In addition, this function gives the opportunity to estimate quite precisely shower maximum $X_{\max}$. Furthermore, its integration over slant depth, together with taking into account of the measured fluorescence yield in air, enables estimation of energy deposited in the atmosphere that corresponds to a calorimetric energy of the shower.

Afterwards, the total reconstructed shower energy (that is the energy of the primary cosmic ray particle) can be estimated after correction for the invisible energy, to which the undetectable neutrinos and muons contribute. Sometimes, large systematic uncertainties on the calculated shower energy arise in the process of shower reconstruction. To reduce them the accurate study of the lateral distribution of light at different stages of shower development in the atmosphere is needed. Such kind of study is provided in the following sections of this work.

4.2. Example of event reconstruction

The process described in the previous section can be visually explained on example of the high energy Auger event #200812102909. This event is analysed in this and next two sections. For convenience, in the following it will be denoted as event 1 (correspondingly the other events, presented in Appendix, will be named as events 2, 3, 4, 5). So, event 1 was recorded by the Auger fluorescence telescope (mirror 2) at the Coihueco site (the 3D view of the reconstructed event is illustrated in Fig.4.4), and has zenith angle $\theta = 41.7 \pm 0.3°$, azimuth $\varphi = 241.3 \pm 0.6°$, and distance to the detector $\sim 5.90 \pm 0.02$ km. After the monocular reconstruction procedure the event primary energy, equal to 4.78 ± 0.47 EeV, was determined together with $X_{max} = 699 \pm 9$ g/cm^2. The estimated Cherenkov fraction is 18%.

The telescope field of view is divided into hexagonal pixels (PMTs). Shower light triggers some of these pixels, forming a shower trace on the camera (Fig.4.5a) (for details on procedure of signal acquisition see section 5.2). This trace defines the shower detector plane (SDP), which includes the shower axis. Location and orientation of shower axis within SDP is determined from the pixel times. The expected time of light arrival at each pixel of the camera (Fig.4.5b) is described by a function of angle χ (*Eq.* 4.4), responsible for determination of pixel directions.

Once the shower geometry is known, the amount of light collected at the aperture of the fluorescence telescope at different time bins is found (Fig.4.6a). During the reconstruction procedure the contributions (direct and scattered Cherenkov light, multiple-scattered light) to total shower light are estimated by calculating the attenuation due to scattering between the shower axis and the fluorescence telescope. Knowing the fraction of these contributions in the total light collected, the estimation of fluorescence emission in the atmosphere can be found by subtracting the photons of mentioned contributions from the total reconstructed light.

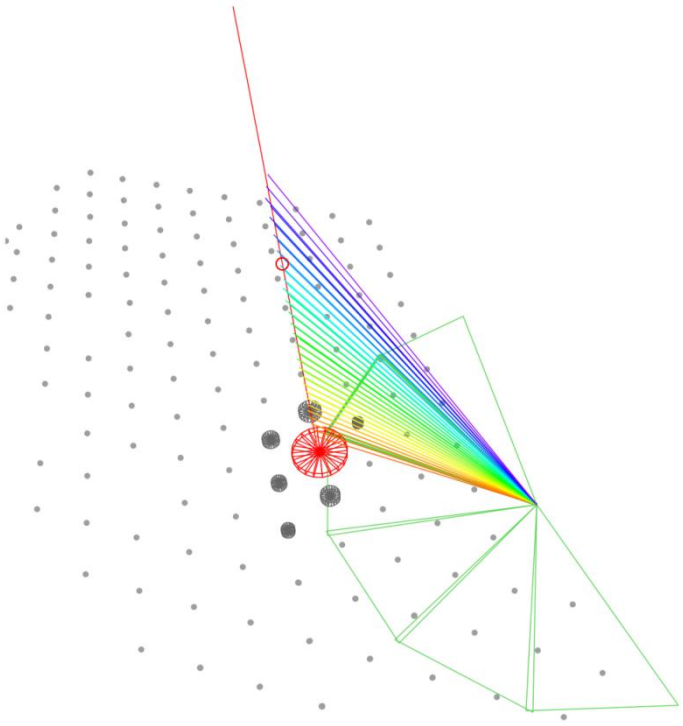

Figure 4.4: The example event 1, recorded in May 2008 at the Pierre Auger Observatory, is shown at the 3D picture together with schematic views of the Coihueco FD telescope and triggered SD stations. A reconstructed shower axis (almost vertical red line) is also defined. The coloured lines represent the light, coming to the FD at different times (in the range from early (violet colour) to latest (red) time moments).

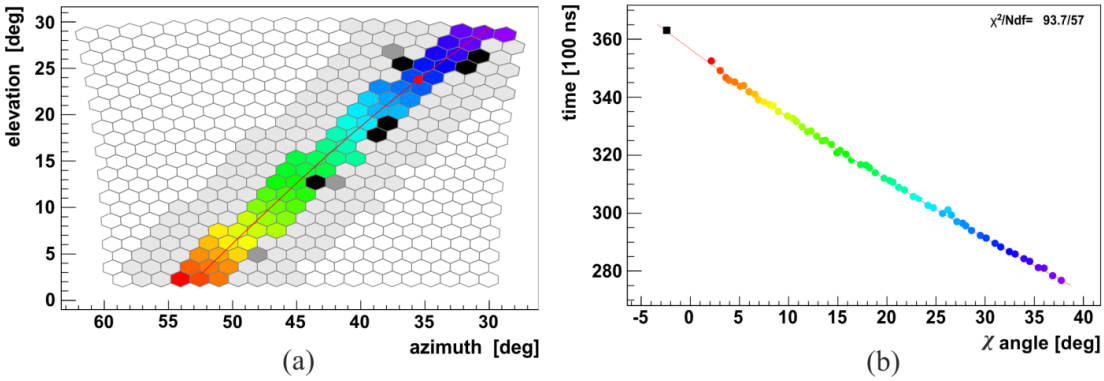

Figure 4.5: Light track of the example event is reconstructed at the telescope camera (a) of the Coihueco FD site. Colours of triggered pixels are changing depending on time of light arrival (according to the colour encoding, mentioned in the previous figure). In addition to the triggered pixels, there are also other pixels at the camera: grey ones correspond to the FLT pixels, which are not a part of the shower; light grey ones are all pixels without a pulse; black pixels have a pulse, but are not a part of SDP. The red line, crossing the camera, represents the SDP, intersecting the detector, and red point at this line denotes the position of shower maximum X_{max}. The time fit (red line) (b) is shown on the right. Coloured points correspond to appropriate coloured pixels. The black square indicates the surface detector station used for hybrid reconstruction.

After atmospheric corrections the light in the aperture is converted into the energy deposit at slant atmospheric depth (Fig.4.6b), and so the longitudinal shower profile is derived. The best fit of the Gaisser-Hillas function to the profile provides the estimation of shower parameters (such as X_{max}). As the atmospheric depth is connected with the shower age (*Eq*. 2.10), the longitudinal shower profile can be also drawn versus age (Fig.4.6c).

For the shower energy calculation, the energy deposit should be transformed to the number of charged particles (Fig.4.6d). Integration over them provides the calorimetric shower energy.

The longitudinal profiles for several other selected events (events 2, 3, 4, 5) are shown in Appendix B together with time fits and camera views with the triggered pixels.

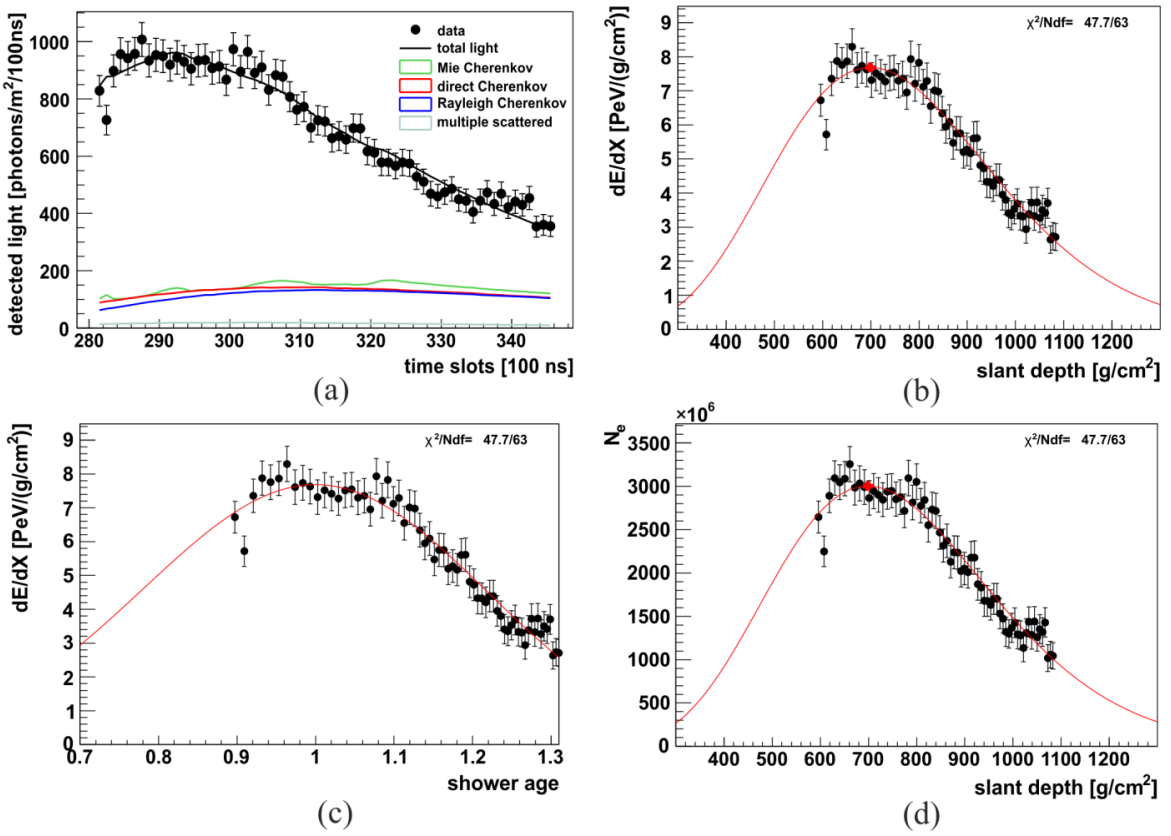

Figure 4.6: The amount of light (a) (black points) of the example event, registered at the aperture of the fluorescence telescope, is illustrated as a function of time. It corresponds to the total reconstructed light, and includes estimation of all its contributions (shown as the coloured curves). The energy, deposited in the atmosphere, is reconstructed from the light at the telescope aperture. Considering it as a function of atmospheric depth gives the longitudinal shower profile reconstruction (b). The red curve, fitted to the points of the profile, is a Gaisser-Hillas function. The energy deposit as a function of shower age is shown at (c). Number of charged particles vs. slant depth is presented at (d).

4.3. Monte Carlo simulation of extensive air showers

Measured signals usually have large uncertainties (shown at the profiles), which may appear because of the fluctuations of the background, electronics, etc., i.e. as a result of inaccuracies in the processes of air shower detection and reconstruction. Such uncertainties, in their turn, influence the uncertainty on shower energy. To solve this problem, a simulation of extensive air showers is used. Large number of showers with the same parameters (energy, zenith and azimuth angles etc.), as real shower has, are simulated. Such simulation is called a real Monte Carlo (MC) simulation. Taking the signal values, averaged over the simulated showers, as the most approximated to the real shower, allows calibration of the measured signal. Besides, the simulation of the detection process is needed to have the correct simulations.

There are several programs, widely used for the extensive air shower simulations. Among them are CORSIKA [47], [88], which simulates the development of the shower, and its derivative CONEX program [89], which is a simpler program, able to simulate 1-dimentional development of the shower.

The Offline framework allows simulations of the detector response, simulated measurements of showers with their reconstruction following, based on these simulations.

Before the Offline simulations, an input file including the main shower characteristics should be created to be subsequently read at the beginning of the Offline simulation procedure. This file can be obtained by means of CORSIKA or CONEX programs, which provide the MC simulations of high energy interactions with a fast numerical solution of cascade equations for the resulting distributions of secondary particles. Using these programs it is possible to simulate the interactions of the cosmic rays with the Earth's atmosphere and the development of extensive air showers. The advantage of the air shower MC simulation is a possibility to estimate the fraction of invisible energy, i.e. the energy not recorded by the air shower detectors (as it is mainly taken away by neutrino, created during shower development).

The MC programs enable simulations of extensive air showers with different input shower specifications. This finally allows getting of appropriate shower profiles. All input parameters, used for simulation in this work, are given by the characteristics of real reconstructed showers, needed to be simulated. Particularly, for CONEX they are: type of the primary particle, energy (up to 10^{21} eV), zenith and azimuth angles. The advantage of the CONEX simulation is providing the realistic air shower profiles including shower-to-shower fluctuations for the minimal computation time.

The Offline simulations used in this work are based on the one-dimensional simulations of proton shower profiles, obtained from CONEX, using QGSJET01 [90] hadronic model for ultra high energy interactions and GHEISHA [91] model for lower energies. As the result of these simulations, the energy deposit profiles as well as charged particle longitudinal profiles are calculated (Fig.4.7). Moreover, the Gaisser-Hillas function is fitted to these profiles and the following shower parameters can be derived for the further Offline simulation: the X_{max} value, the number of particles at shower maximum N_{max}, depth of the first interaction X_0, shower energy.

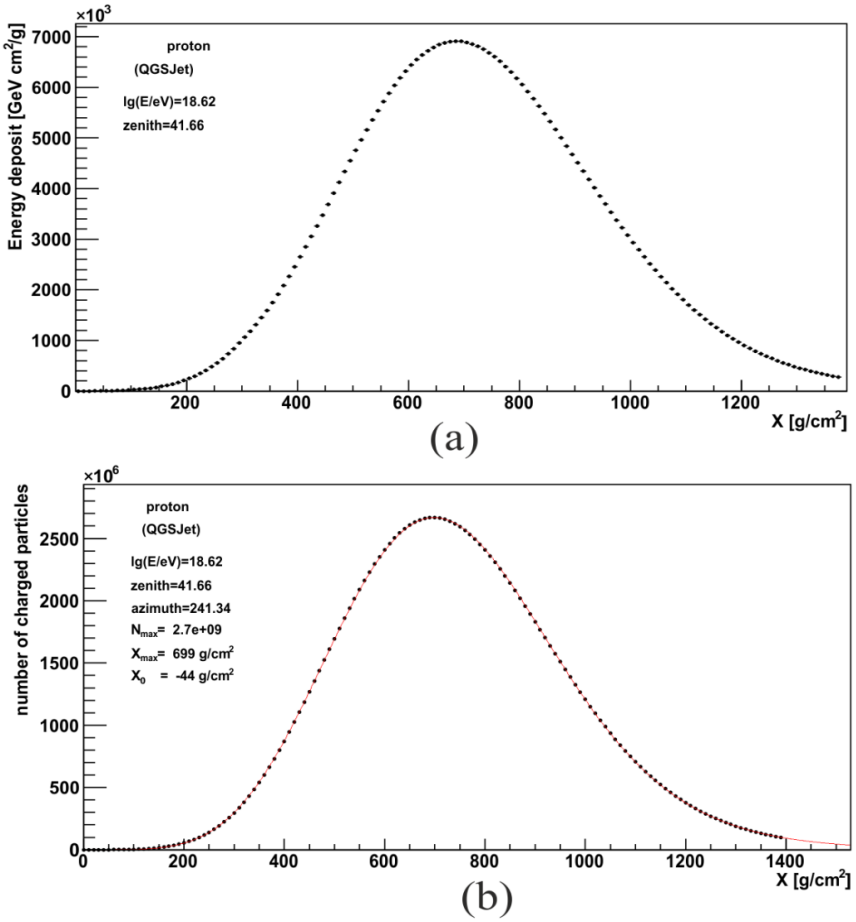

Figure 4.7: The longitudinal shower profiles, obtained using CONEX for the real event 1 (described in section 4.2), include energy deposit profile (a) and a distribution of charged particles (b). In addition, the Gaisser-Hillas function is shown (red fitted line), together with the shower parameters, estimated from fit.

Afterwards, the simulation of the shower detection process at the Auger observatory, using Offline framework, is done. It includes the simulation of the detectors response and takes into account the triggering of the surface array by the particles arriving at the ground, and of the FD eye by fluorescence light emitted by the shower particles and propagated in

the air. The real MC approach is used for hybrid detector simulation, and is applied to this work. The specifics of such simulation procedure implies a combination of the time dependent detector status and the use of monitoring data for each pixel of the camera. The simulation procedure contains several steps (represented also by a list of modules in the module sequence (Appendix A2)). First of all, the CONEX output file, which includes some showers, is read as an input file for Offline. Secondly, the atmospheric density and temperature profiles are defined based on the GDAS atmosphere parameterization [68]. After that the following steps are launched to provide a real MC simulation:

1. Generation of shower impact position and time stamp (responsible module EventGenerator) for determination of shower core location on the ground. This step precedes both real FD and SD simulation parts.

2. Event preparation (FdSimEventChecker module) includes a choice of the proper FD telescopes (eyes, pixels) to be used for further simulation. This is done based on the information about the event actual time and geometry (obtained, in particular, from the FD uptime manager, i.e. manager which is operating by the information about the time intervals, at which the FD was successfully operating), and using energy dependent telescope trigger probability.

3. Light generation (ShowerLightSimulator module) is a simulation of the fluorescence and Cherenkov photons along the shower track. At this step the simulation of only one of these components is also possible by switching off another one. Shower light simulation allows obtaining the information about the number of shower particles, with the following estimation of their energy deposited in the atmosphere, and calculation of the number of fluorescence photons emitted along the shower axis.

4. Propagation of the shower light to the telescope diaphragm (LightAtDiaphragmSimulator module) is also described. The light flux is calculated with certain time resolution (100 ns for standard FD telescopes), and at certain time moments, at which shower enters and then leaves the telescope field of view. It is also possible to simulate both direct (fluorescence and Cherenkov) and scattered (Mie and Rayleigh Cherenkov) light components, coming to the diaphragm.

5. Lateral shower structure (ShowerPhotonGenerator module) is implemented in this step. It should be pointed out that at the previous steps the shower was treated at each stage of shower evolution as a point-like one-dimensional object. However, it is a disk-like object, and the point-like simplification is corrected by implementation of the lateral shower particle distribution into shower simulation procedure. Using appropriate atmospheric

parameters, the lateral distribution of electrons at each stage of shower development can be found based on the shower age dependent parameterization [92], used only for the fluorescence light production. For proper simulations of the lateral Cherenkov light distribution, another parameterization [93] should be implemented. Also multiple scattering (Mie and Rayleigh scattering effects in the atmosphere) should be included into the flux, being parameterized by [94] or [95] (the Pękala parameterization [95] is the one, used for simulations in this work). Then, the total light flux at the diaphragm, summed over all wavelengths at each time interval, is converted into the number of photons. In sections 5 and 6 of this work, the contributions of the described components of shower light into the total signal are investigated, using the lateral distributions of photons, measured at the camera.

6. Simulation of the telescope optics (TelescopeSimulator module). After determination of the number of photons at the diaphragm, photons are traced through the telescope. During ray-tracing of photons in the telescope, properties of light and telescope are taken into account. They include: reflection and refraction at the corrector lens, mirror, light collectors and PMT window; transmission and reflectivity of the materials. Consideration of these characteristics leads to the proper estimation of the telescope effects, and to increasing of the accuracy of simulations.

7. Adding the background photons (such as from stars and moon) to the photon traces (FdBackgroundSimulator module) of the shower light allows to reproduce the total light, coming to the detector. In this work the so-called 'bgLoop' option is used in telescope background simulations. It is responsible for implementation of the background variances per pixel from the FD monitoring data, and so provides realistic background simulations.

8. Simulation of the telescope electronics (FdElectronicsSimulator module). At this step the electronics noise is added to the signal obtained from shower and background. Formed in such a way, the total signal for each pixel is further saved as ADC counts (see section 5.2). The 'useMonitoringInfo' option, which is applied for simulation process, should be switched on to provide the realistic simulations with the FLT threshold (see section 3.1.2) as well as the electronics noise data from the monitoring database. The monitoring and uptime information are the features, specific to the real MC simulation. So the total signal, obtained at this step of simulation, is supposed to correspond to the measured signal of appropriate real events.

9. Simulation of a response of FD trigger (FdTriggerSimulator module). Simulated at the previous steps ADC traces are used for FD trigger simulation. Four trigger levels, described in section 3.1.2, are implemented at this step. If the event passes them, a

conclusion whether to record the event for further use or not is made.

10. A simple procedure (SdSimpleSim module), which provides generation of realistic air showers in the surface detector of the Pierre Auger Observatory without employment of the full shower and detector MC simulations (appropriate for ordinary hybrid simulation) is provided at this step. The input information, including the one-dimensional shower profiles, is read from CONEX file. Using these data the generation of lateral shower signal at SD array and the timing information are provided. The one-dimensional shower longitudinal profile is extended to yield a three-dimensional air shower object, which can be detected by the surface detector.

The described above steps are the basic stages of the real MC simulation. They can be supplemented by other modules, needed for the specific analysis. After a successful detector simulation the events are reconstructed based on the reconstruction steps, described in one of the previous section, and using detector configuration and parameters of the atmosphere.

In particular, for simulation and further reconstruction of the shower at the Pierre Auger Observatory, the procedures described in the above are used. As a result, the profiles obtained after simulation and then after reconstruction (Fig.4.8), are found for example event, discussed in section 4.2. It is expected that the final profile (obtained after reconstruction) corresponds to the reconstructed profile of real event. Due to fluctuations it is not always true, therefore the average values for several tens simulated showers should be taken into account to provide unbiased data analysis.

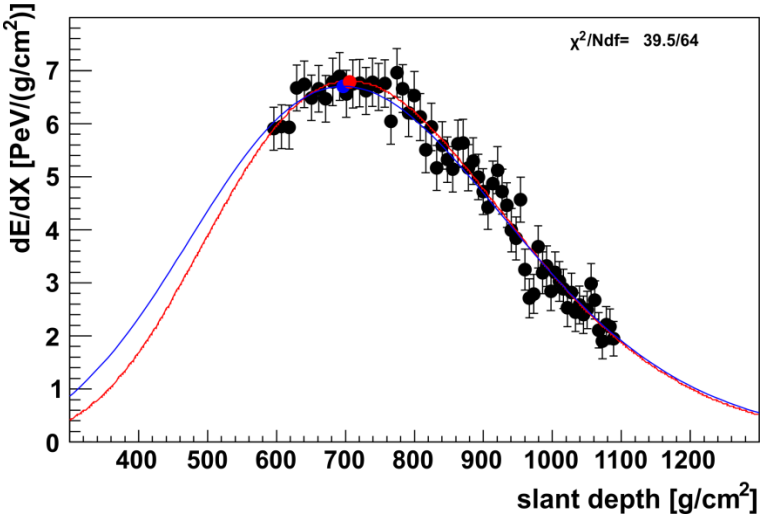

Figure 4.8: The longitudinal profile of event, created from simulation procedure is shown in the blue colour. After application of the reconstruction module sequence it results into the profile, coloured red. The reconstructed values of primary energy (equal 3.96 EeV), and shower maximum (X_{max} = 706 ± 8 g/cm^2) are a little bit different from those of real measured event, mentioned above.

5. Optical image of an extensive air shower

During simulation of shower development in the atmosphere several important aspects should be taken into account for precise shower parameters determination. The distribution of shower particles around the shower axis is often considered to be of a disk-like shape with the disk size equal to Molière radius r_M ($r_M \approx 80$ m at the sea level). Therefore, if the shower is seen from a distance of several kilometres, it can be represented as a point-like source of light, moving with the speed of light. The light, emitted during this process is further registered at the camera as the shower image. The point-like approximation of the shower, used in such experiments as Fly's Eye and HiRes, is generally relevant, but it is not sufficient for precise shower energy determination, especially for close showers. For the correct analysis, the disk-like structure of the shower front should be considered during measurements of light distribution in shower optical image. The principal part of high energy events, registered at the Pierre Auger Observatory, have the size of shower image, equal 1 - 4 pixels, that corresponds to 2ζ angle ~ 1.5 - 6º (Fig.5.1).

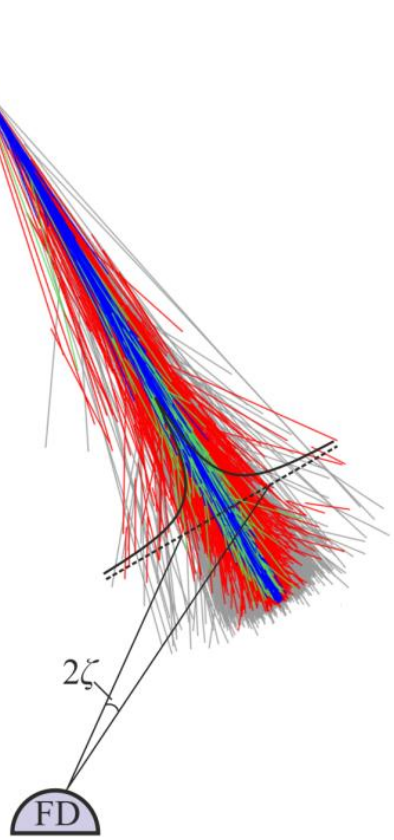

Figure 5.1*:* Main part of emitted light (collected in 2ζ angle) is registered by the FD and further used for reconstruction. But some part of shower light is lost and not included to reconstruction, as follows from the lateral distribution of light around shower axis.

The main part of shower photons, emitted in the process of shower development and forming the shower optical image, goes to pixels located in the center of shower image (usually 1-4 pixels). However, as the image is usually larger than the field of view of a single pixel used for light registration, some part of light is expected not to be registered (Fig.5.1). This smaller part of shower photons comes to the pixels situated relatively close to the image center, and is not registered by FD, as signal values in those pixels are below the pixel trigger thresholds. As a result, that part of photons is not included into the beam of registered light, and shower energy is underestimated. That is why it is important also to have a good theoretical background to be able to estimate precisely both the shower optical size and expected distribution of light in shower optical image. In the following sections the method of determination of shower image angular size and lateral distribution of fluorescence light in shower optical image is discussed together with its practical application to showers measured at the Pierre Auger Observatory.

5.1. Shower development and shower image in the FD

As the shower front is not a point-like source, but has a disk-like shape, the snapshot of the fluorescence light from the shower is seen in the detector camera as a circular spot [96]. This spot is the shower optical image formed by photons which come simultaneously at the camera from different stages of shower development [97]. Those photons originate from the surface *S* (Fig. 5.2). At this figure the shower at each moment of time is represented by a disk with a radius *r*, which moves downward in the direction of the shower axis. Let's consider the movement of particles from disk at position *m*. Photons, emitted at the same time from the points *A* and *B*, do not arrive at the same time to the FD eye, as the distances of these points to the eye are different ($AO \neq BO$). While a photon, emitted from point *B*, reaches the intermediate point *D*, shower disk is moving to a new position *n*. So, that $BD = AC$. As the distances $OD = OC$, the photons emitted from the points *C* and *B* will reach the FD eye simultaneously, while the photon from point *A* comes early. In other words, if the photons arrive simultaneously from the points *B* and *C*, the time, for which a particle passes the distance *BO*, equals to the time, needed to pass the distance $AC + CO$.

Consequently, the surface *S* consists of points of emission of photons, which arrive to the FD eye at the same moment of time. Photons emitted from the surface *S*, form the spot-like shower optical image (Fig. 5.3) at the camera at each moment of time.

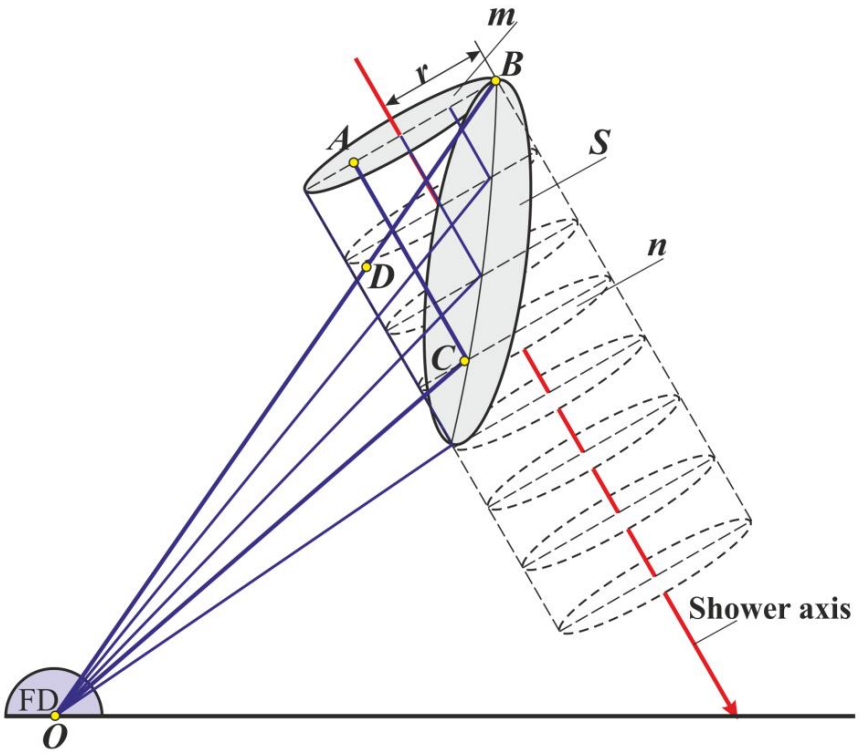

Figure 5.2: Schematic view of the air shower development (updated from [97]), with the stress on the geometry of this process and on forming of the shower image, seen by the FD. Shower front with radius *r* is moving through the atmosphere. Photons, which are coming simultaneously to the FD eye and constitute the shower optical image, originate from the surface *S*.

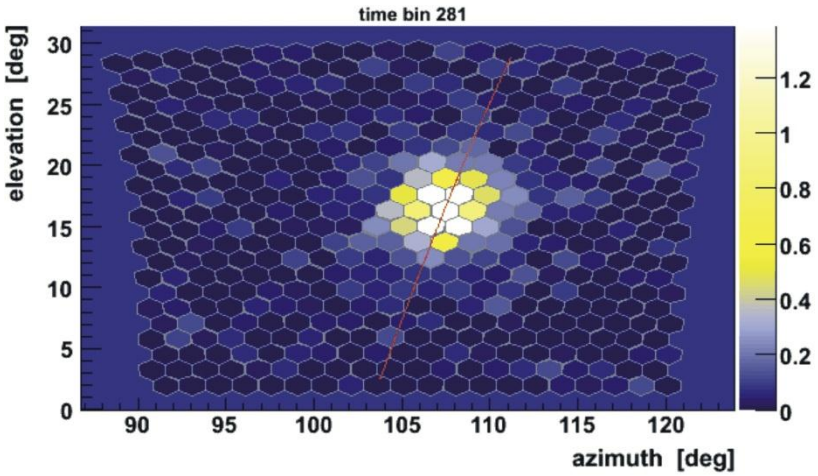

Figure 5.3*:* Example of shower optical image for real Auger event. It is formed by the photons coming to the camera at certain time moment and from a certain surface (as discussed above), forming in such a way a spot on the camera. A set of the spots, registered sequentially for all time bins, constitute shower trace at the detector camera. The indicated colour scheme corresponds to the change of logarithm of the signal. The red line represents the SDP.

The size of the shower optical image is defined as the angular diameter of the image spot, which contains the fraction of light, registered on the FD camera and limited by the circle of 2ζ angle (Fig. 5.1) at the shower image (the ζ angle corresponds to a certain radius r around shower axis (Fig. 5.7)). For distant showers the optical image is usually smaller than the field of view of a single pixel, that allows to collect almost 100% of light, using the signal-to-noise (*S/N*) maximisation algorithm (when the light is collected in the circle with radius $\zeta_{S/N}^{\max}$, which has a maximal *S/N* value). However, for close showers (with distance to detector $d \lesssim 10$ km) the shower image size is larger than 1.5° (single pixel size). So that the part of the photons, forming the image, hits the pixels, which are situated relatively close to the image center. Those pixels may have a signal value below the triggering threshold, that leads to underestimation of the total shower signal and consequently of the shower energy. This effect can be taken into account by means of a lateral distribution function (such as the Góra function, see section 5.4), fitted to the measured signal. However, such function should be proven experimentally by comparison with measured lateral profiles. This task is discussed in detail in section 6.

5.2. Procedure of signal detection in FD pixels

Determination of the signal distribution in shower image is based on the analysis of shower signals, registered in individual pixels of the camera at certain moments of time (time bins, equal 100 ns). They include the photons, coming from the shower, and the background light, constantly recorded from bright stars, our galaxy, the moon, atmosphere etc. [98].

The light from an air shower triggers pixels along the observed line of its propagation across the camera. When the shower trace at the camera is formed, the signal at each pixel is recorded (Fig. 5.4). Signal amplitudes vary for each pixel, and depend on the time, at which shower light arrives to the pixel. At the beginning, the signal, saved as ADC counts, contains the background light, which is responsible for most fluctuations seen in ADC traces. For calculation of the average number of background photons the variance, caused by electronics noise, should be subtracted from the recorded variance of ADC traces. After that, the signal without background light is determined for each pixel by subtracting the background from the trace. Afterwards the signal is converted from the ADC counts to photons (Fig. 5.5), using calibration constants. The photon traces for each pixel of the camera are reconstructed both for real measured as well as for simulated events.

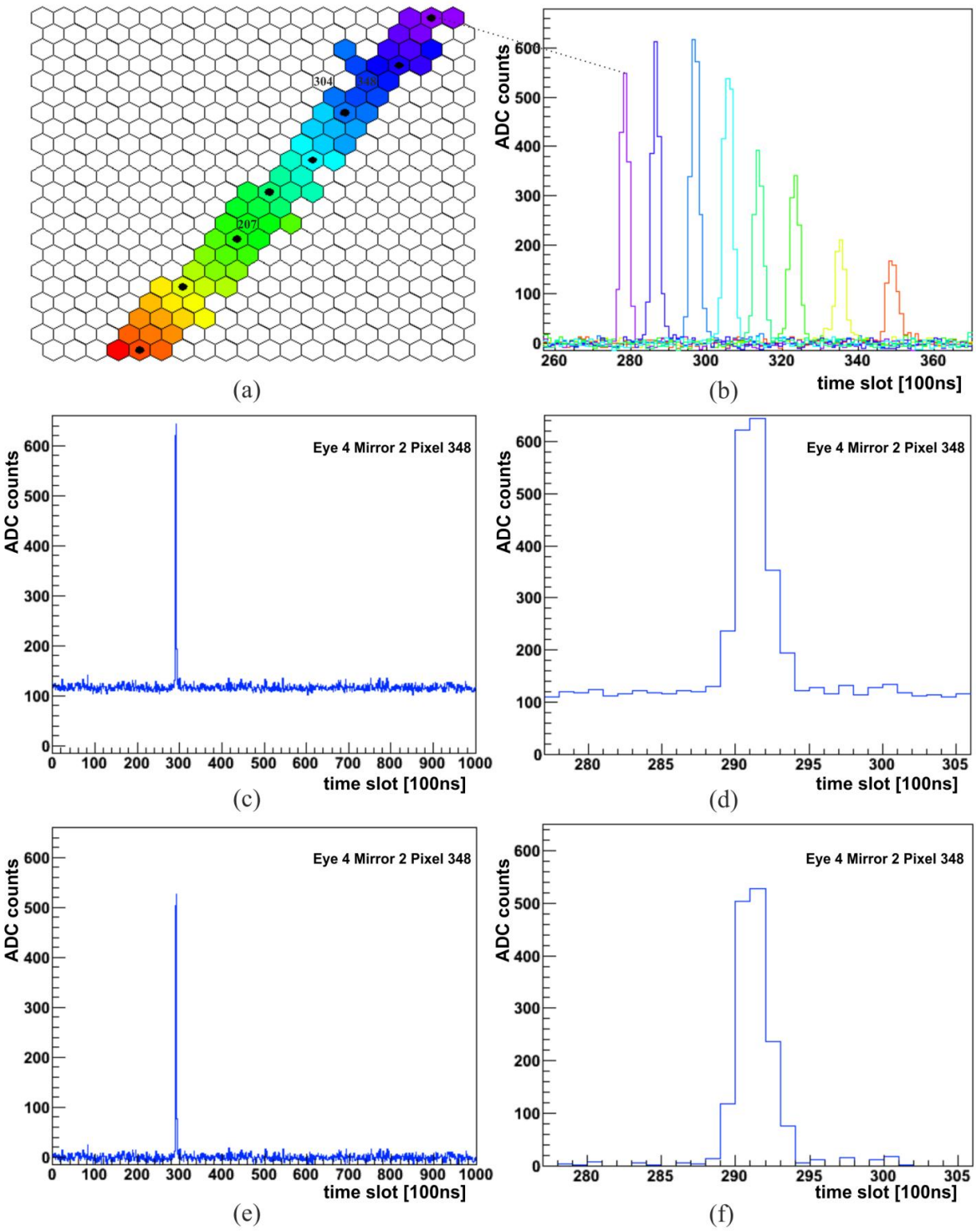

Figure 5.4: Several pixels (marked by black dots) are selected from the shower trace at the camera (a) to indicate the change of a signal (in ADC traces, without background) with time (b). The data are analysed for previously discussed Auger event 1. Typical acquisition of the signal is shown in detail in figures (c-f) for single example pixel #348, indicated by its number at the camera. In particular, signal in ADC traces with background is presented at (c) with its closer view (d), and signal in ADC traces without background is shown correspondently at (e) and (f). Shower signal values are determined by the height of the pulses.

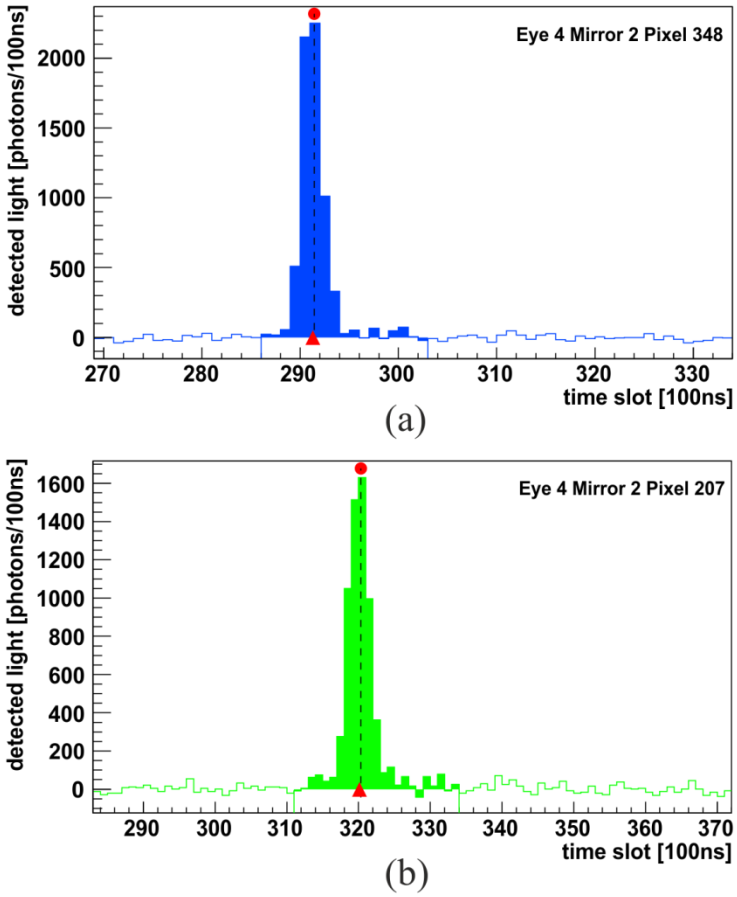

Figure 5.5: After application of the calibration constants of each pixel to signal in ADC counts, the signal in units of photons is recovered for pixel #348 (a) (discussed at (Fig. 5.4)). For comparison also a pulse, registered in the pixel #207 (b) at later moment of time is shown.

It should be also mentioned that a well visible pulse is seen in Fig. 5.4 only for coloured pixels, which passed all trigger levels and definitely have the shower signal. The white pixels, situated nearby the pixels with pulse, are considered not to have a shower signal and are not included into the ordinary analysis. They usually contain only fluctuations of the background light (Fig. 5.6). However, such pixels may contain a small part of shower signal (usually lost, as it was shown in Fig. 5.1). Therefore, they are taken into account in this analysis for measurements of the lateral distribution of shower light.

Once the signal in each pixel is known at each stage of shower development, the lateral distribution of photons in the shower optical image can be found.

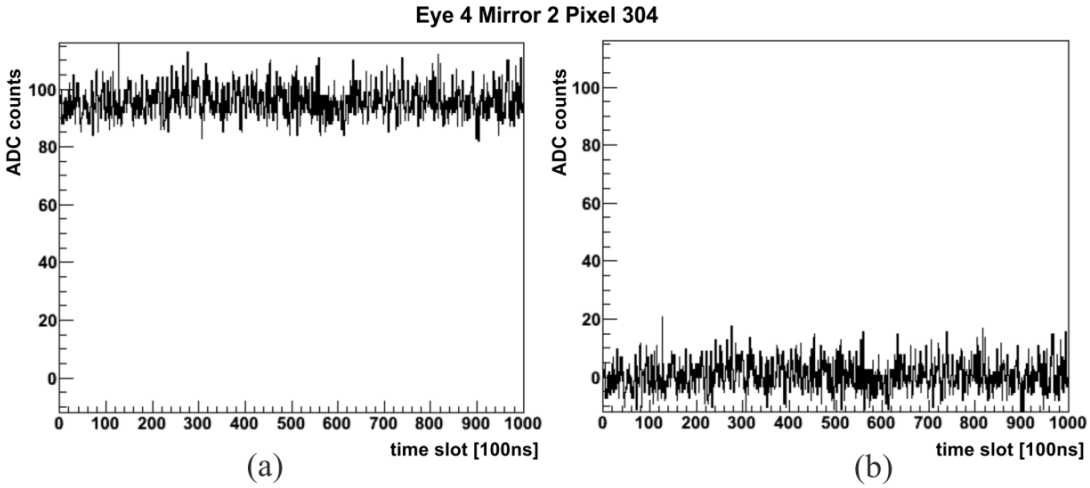

Figure 5.6*:* The signal without pulse is shown in ADC counts for pixel #304. Herewith, the background light is included at (a), and then subtracted at (b).

5.3. Measurement of lateral distribution of light in shower optical image

For the measurement of the lateral distribution of light in the shower optical image, the photons should be collected at certain moment of time (or in our analysis - at certain stage *s*) from all pixels located in a circle of definite angular radius ζ (Fig. 5.7). Then the signal is integrated within this circle, giving the number of shower photons and number of background photons for this moment of time.

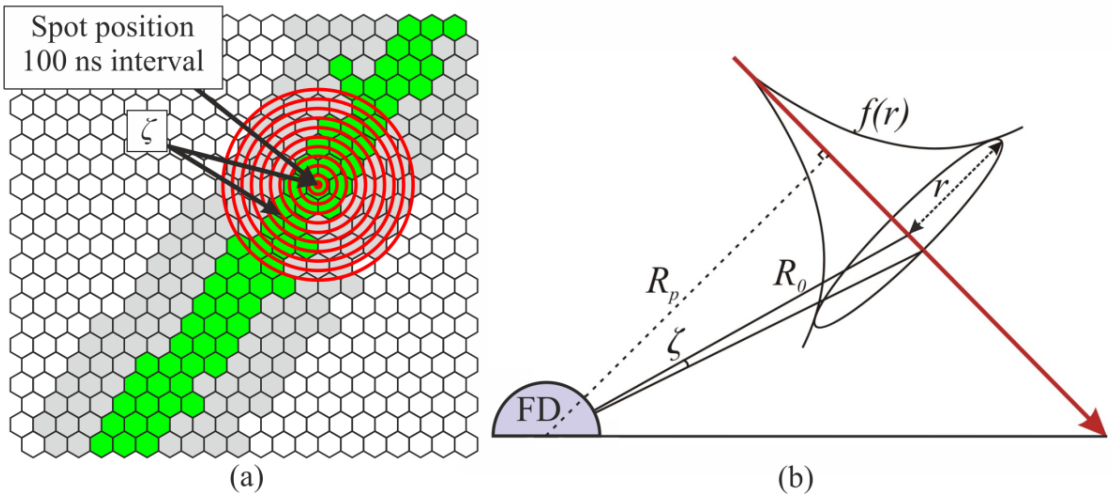

Figure 5.7: Shower optical image (a) of the discussed early real Auger event 1 is shown. Shower light triggered some pixels (green pixels), so that a trace of the shower at the FD camera is formed. Grey pixels are considered to be the pixels without pulse, but are used in this analysis for lateral shower profile determination. It is not possible to read the signal of white pixels. The light is collected each 100 ns in the circles of ζ radius, that correspond to the radius *r* of light distribution around shower axis (b).

At this stage of the analysis, the maximal possible angular radius ζ is chosen for the following lateral distribution measurement (Fig. 5.8). It equals to the circle radius, which takes into account the signal from all the available pixels at the camera (including both pixels with and without a pulse). The circle radius is limited by the edges of the camera. To demonstrate the shower evolution with different values of shower age parameter *s*, several circles (Fig. 5.8) of different radius are selected for those stages of shower development. The light was determined as a sum of pixel signals, measured inside these circles with the step $\Delta\zeta = 0.5°$. The pixel signal is taken into account if the pixel centre is inside the circle. This procedure allows very precise determination of the lateral distribution of light $f(\zeta)$ in shower optical image.

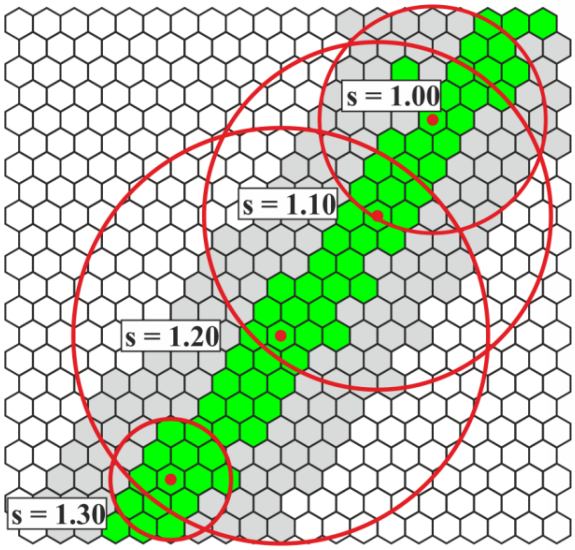

Figure 5.8: Lateral shower light distribution is measured inside the regions, limited by circles at the shower image. These regions correspond to several selected stages of shower development with different values of shower age parameter *s*.

The measured lateral distributions are shown in Fig. 5.9 for different age parameters of the event 1. In these examples the light is collected at certain stages, corresponding to the shower age parameter *s*. However, there are often more than one shower profile, measured for the same shower age. As the measurements are very detailed, different shower time bins can correspond to approximately the same shower age. For example, the profiles, measured at time bins 297 and 298, refer to the shower age equal 1.046 and 1.054 correspondingly; that means that different time bins have approximately the same value of shower age ~1.05. When such situation takes place, the signal used in lateral distribution measurement is calculated as an average value of signals from different profiles of the same shower age. The number of such profiles for one shower age is usually up to 10.

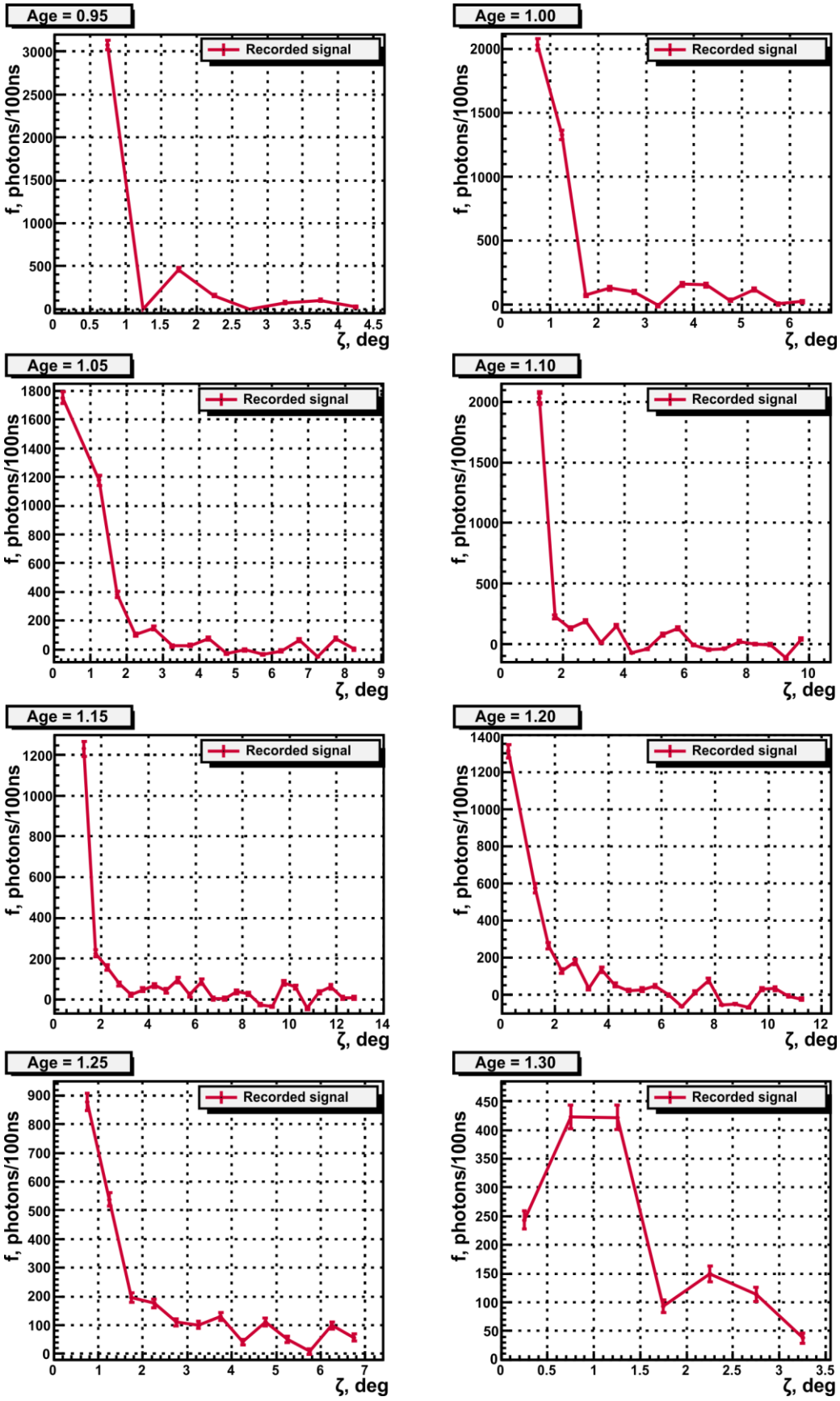

Figure 5.9: The lateral distributions of light *f(ζ)* for the real Auger event 1 (as described above) are shown in a sequential order for different shower ages, representing distribution of light in the circles distinguished in Fig. 5.8.

For better representation of the shape of the lateral distribution, the integrated (cumulative) lateral distribution, known as a fraction of light function *F(ζ)*, is used in the further analysis instead of *f(ζ)*:

$$F(\zeta) = \int_0^{\zeta} f(\zeta') 2\pi\zeta' d\zeta'. \qquad [Eq. 5.1]$$

Such distribution, measured for event 1, is shown for several measured shower stages in Fig. 5.10.

The angular distribution of light in the shower optical image is proportional to the local distribution of photons, emitted simultaneously in the air from the surface *S* (Fig. 5.2). It can be described by the lateral distribution of light, emitted around shower axis at certain stage of shower evolution. In other words, the part of light *F(ζ)*, registered within the *ζ* angle, is proportional to the appropriate part *F(r)* of the light, emitted around the shower axis [92]:

$$F(\zeta) = \int f(\zeta') 2\pi\zeta' d\zeta' \sim \int f(r') 2\pi r' dr' = F(r), \qquad [Eq. 5.2]$$

where *f(r)* is a normalized lateral distribution of the emitted fluorescence light, that can also be characterized as a function of light distribution in the shower optical image *f(ζ)*. Hence it appears that the shape of light distribution around the axis should be the same as the shape of light distribution in camera. *f(r)* is also referred to as the shape function, since the brightness distribution of the shower image also depends on the shape of *f(r)*. The transition from angle *ζ*, used for measurements of shower image at the camera, to the distance from shower axis *r* can be deduced from the shower geometry (Fig. 5.7b) and equals to:

$$r = R_0 \cdot \mathrm{tg}\left(\frac{\zeta}{2}\right). \qquad [Eq. 5.3]$$

Thereby, the lateral distribution of particles around the shower axis *f(r)* is a function, used for calculation of the shower optical size (the angular diameter of the image spot, limited by the 2*ζ* angle). The fraction of light, estimated at the distance *r* from shower axis, is shown in Fig. 5.11 for selected values of the shower age parameter.

In summary, the image of the real shower is not a point, since it has a definite width. Neglecting this fact may result in an underestimation of shower energy, by 2% - 14% (depending on the distances of shower to the detector) [92]. To correct this problem, the lateral distribution should be implemented in the analysis. To find the lost part of shower energy, the parameterization of the lateral distribution of shower fluorescence light (the so-called Góra function [92]) should be applied. Such kind of parameterization is already

implemented in detector simulations of Auger Offline framework, as well as in the event reconstruction.

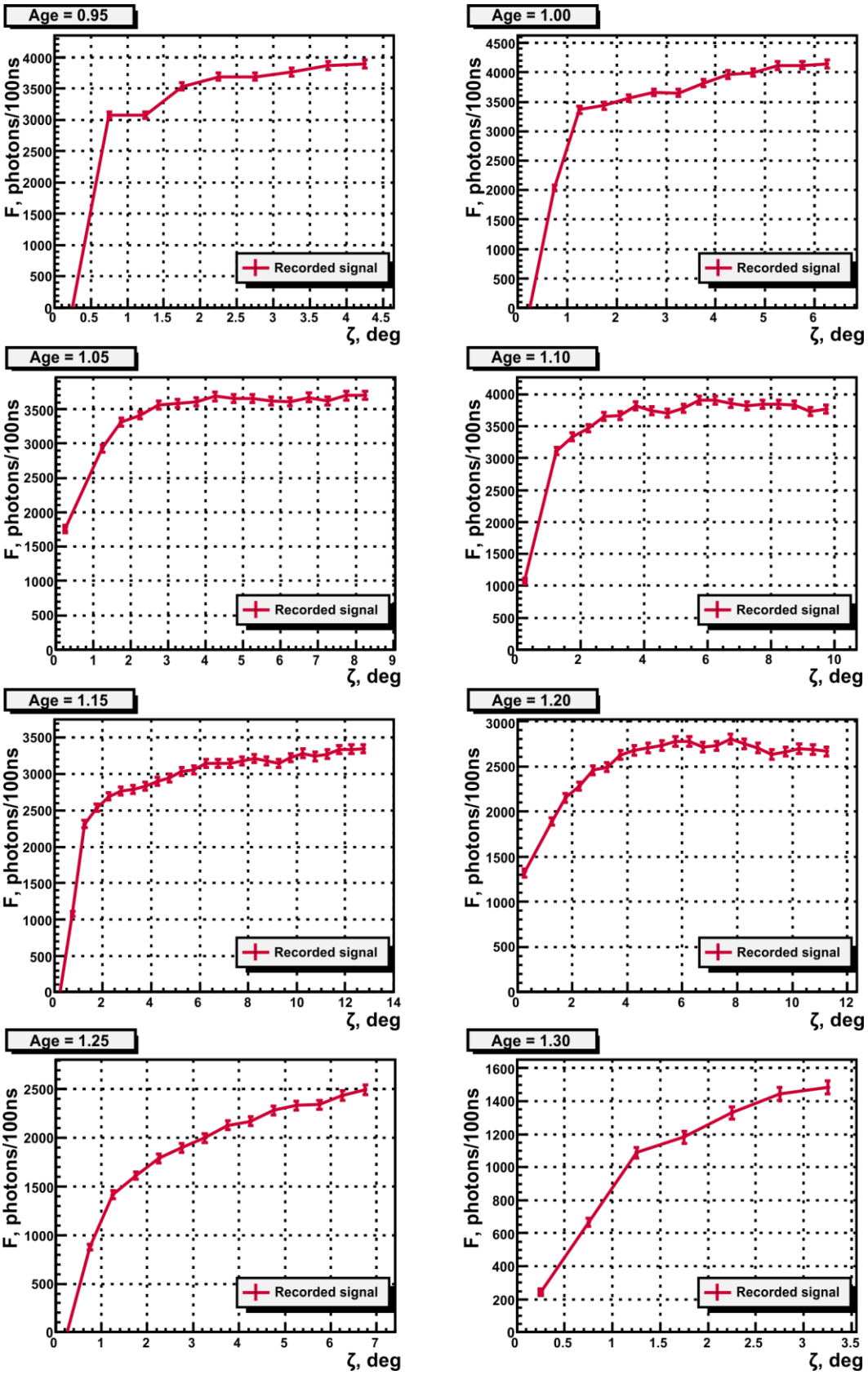

Figure 5.10*:* Plots, representing the fraction of shower light *F(ζ)* in *ζ* angle, are shown for different shower ages for the real shower (event 1).

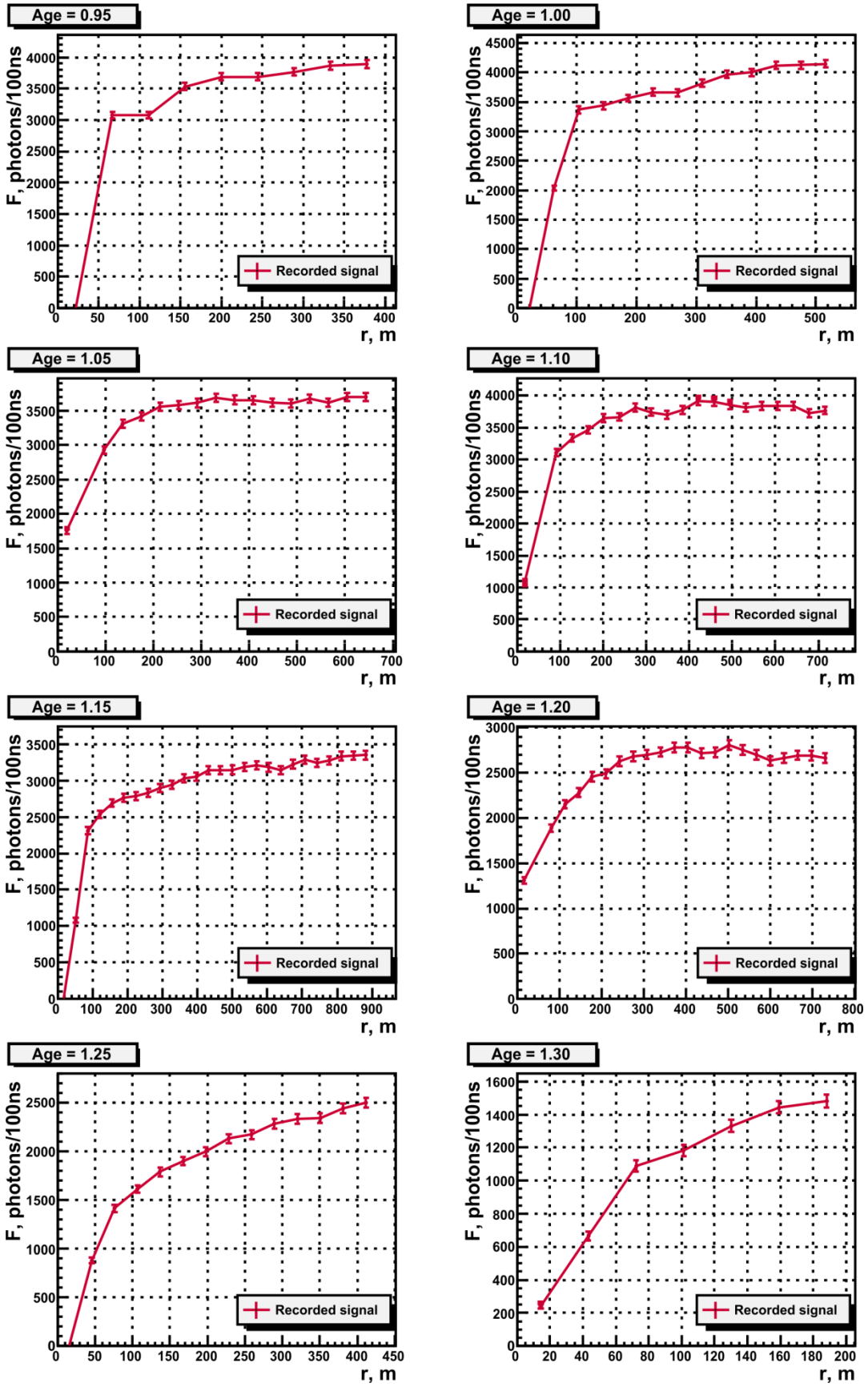

Figure 5.11: Plots, representing the fraction of shower light *F(r)* at distance *r* around shower axis, are shown for different shower ages for the real shower (event 1).

In addition to the measured profiles, the simulated profiles are presented in the following sections. The MC simulation of the showers with the same characteristics, as measured showers have, is needed. To minimize the effect of fluctuations, an average of many simulations should be used. The simulated lateral profiles are discussed in section 6 together with the measured ones.

5.4. Parameterization of the lateral distribution of fluorescence light in a shower

To obtain the lateral distribution of shower light, the NKG approximation of lateral distribution of shower particles (discussed in section 2.2.2), can be used. However, it describes only the electromagnetic shower component and so does not determine precisely the lateral distribution of the whole shower. Therefore, the CORSIKA approach [99] was proposed to obtain a more realistic simulation of the spatial distribution of light production. This section summarizes the results, obtained by D. Góra et al. in the works [92], [97], [99].

The distribution of photons *f(r)*, emitted (from the surface *S*) around shower axis, is described by the lateral distribution of energy deposited by shower particles in the atmosphere *dE/dX:*

$$f(r) \sim \frac{dE(X,r)}{dX_v dr}. \qquad [Eq.\,5.4]$$

It is called CORSIKA approximation as the profiles of deposited energy were obtained based on simulations using CORSIKA program. These profiles describe the sum energy, deposited by shower particles, including particles below threshold energy:

$$\frac{dE(X)}{dX_v} = \frac{E_{ioniz}}{\Delta X_v} + \frac{E_{e^{\pm},cut}}{\Delta X_v} + \frac{E_{\gamma,cut}}{\Delta X_v} + \frac{1}{3}\frac{E_{\mu^{\pm},cut}}{\Delta X_v} + \frac{1}{3}\frac{E_{had,cut}}{\Delta X_v}, \qquad [Eq.\,5.5]$$

where dX_v is the vertical atmospheric depth, E_{ioniz} – energy deposited as the result of ionization in the interval ΔX_v, $E_{i,cut}$ – the energy of particles of type *i* with the energy below threshold, used in simulations.

The fraction of deposited energy is obtained by numerical integration of the normalized distribution of the deposited energy density $\frac{dE(X,r)}{dX_v dr}$ as a function of distance *r* in the plane perpendicular to the shower axis:

$$F(r) = \int_0^r \frac{dE(X,r')}{dX_v dr'} 2\pi r' dr'. \qquad [Eq.\,5.6]$$

Such function *F(r)* allows calculation of the expected amount of shower light around shower axis, which should correspond to the true shower signal, registered by the

fluorescence detector. According to this function *F(r)*, the shape of lateral shower profiles does not depend much on shower energy, primary particle or zenith angle. It is universal and, when expressed in the Molière units $F(r/r_M)$ (Fig. 5.12), depends on shower age parameter only.

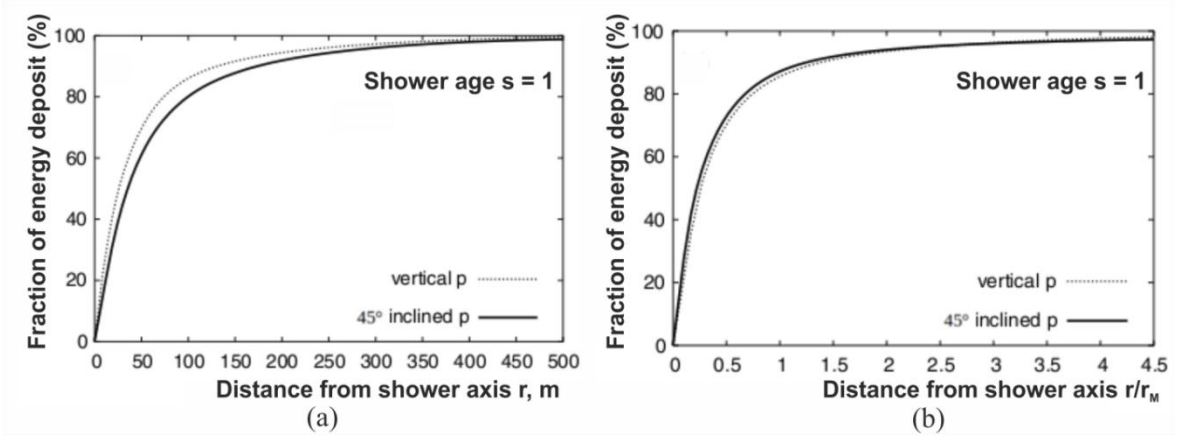

Figure 5.12*:* Plots, simulated at *s* = 1, using CORSIKA: integral of energy deposit density vs. distance from shower axis *r* (a) and vs. distance in Molière units r/r_M (b) for vertical and inclined proton showers with energy 10 EeV. The universality of the profiles is clearly seen in the case (b).

Based on Monte Carlo simulations, provided by CORSIKA, the universal parameterization of $F(r^*=r/r_M)$ for fluorescence light was proposed in [92] (the so-called Góra function):

$$F(r^*) = 1 - (1 + a(s) \cdot r^*)^{-b(s)} \qquad [Eq.\,5.7]$$

with parameters *a(s)* and *b(s)* :

$$a(s) = 5.151s^4 - 28.925s^3 + 60.056s^2 - 56.718s + 22.331, \qquad [Eq.\,5.8]$$

$$b(s) = -1.039s^2 + 2.251s + 0.676. \qquad [Eq.\,5.9]$$

The shape of this function changes, depending on shower age (Fig. 5.13).

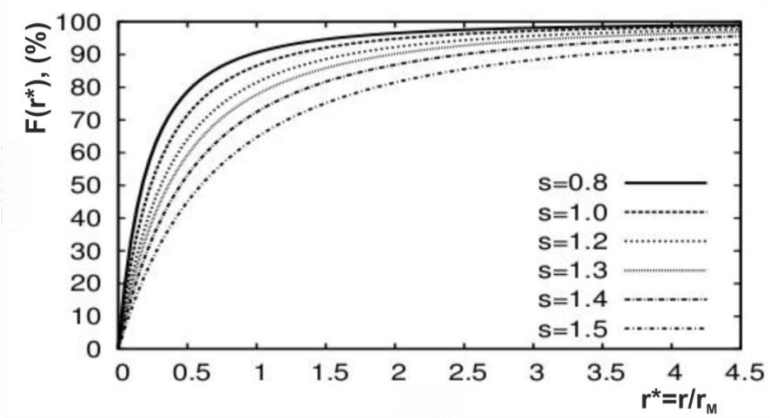

Figure 5.13: Integrated lateral distribution function, i.e. Góra function, which depends on shower age parameter *s* and distance from shower axis *r**.

So, the above equations give a universal parameterization of the integral of deposited energy, which can be used for description of lateral distribution of light for showers with different energies, primary particles and zenith angles.

The energy deposit density *f(r)* can be found by differentiation of the Góra function:

$$f(r) = \frac{a(s)b(s)(1 + a(s) \cdot r^*)^{-b(s)-1}}{2\pi r \cdot r_M}. \qquad [Eq. 5.10]$$

This equation is also referred to as the differential Góra function. This function allows making precise simulations of light distribution around shower axis.

Thereby, the Góra function (*Eq.* 5.7) can be used for calculation of expected size of shower optical image in the fluorescence detector camera, as it can also define the percent of light, collected within ζ angle, at each stage of shower evolution.

The lateral distribution, measured for real events, should be used to test the Góra function experimentally. If the experimental distribution agrees with the Góra function that means that there is also the appropriate relation between shower age *s* and the shape of the lateral distribution. Consequently, it may become possible to find the shower maximum $X_{\max}$, knowing the shape of the lateral distribution of fluorescence light. These tasks are discussed in detail in section 6.

6. Analysis of lateral distribution

As it is was mentioned above, existence of the relation between the shower age and the shape of the lateral distribution of fluorescence light around the shower axis is given by the Góra function [92]. However, as this is a phenomenological function, derived from CORSIKA shower simulations, it should be proven experimentally. For this purpose the test of the Góra function is done in section 6.2. For this test the lateral distribution of simulated showers is also needed. To reduce the fluctuations in the lateral distribution profiles of the simulated showers, a large number of showers is simulated with the same parameters, as the real showers have. The signal from these simulated showers is averaged over the number of showers. So, the signal used in all discussed simulated plots in this work is an average value of the signal, obtained from some number of showers. In particular, the number of simulated showers used for the analysis in the current work is about 50 for each event.

6.1. Measurements of light fraction

Before the test the special features, important for proper test, are discussed. First of all, to be able to compare the measured light with the theoretical function, the measured quantities should be considered in the units, appropriate for the Góra function, i.e. as normalized fraction of light:

$$F_{norm} = \frac{F(r/r_M)}{Norma}, \qquad [Eq.\,6.1]$$

where $F(r/r_M)$ is a fraction of light as a function of distance in Molière units, *Norma* is a normalization constant. Coming from the assumption that the Góra function defines the percent of fluorescence light from the shower (100% of light is emitted, if $F(r^* = r/r_M) = 1$), the normalization constant can be found from fitting the Góra function to the simulated fraction of fluorescence light. After application of this constant to the measured and simulated fractions of total light, the profiles of normalized fraction of light F_{norm} can be obtained (Fig.6.1, Fig.6.2) (for fractions of light, estimated for several other example events, see Appendix C).

The profiles obtained for the simulated showers include the following components: the fluorescence light only (green curve on the plots), and the fluorescence and Cherenkov light components (blue curve). In addition, multiple scattering light makes its contribution in both simulations with the fluorescence light only and with the fluorescence and Cherenkov light. The simulated profile, including the fluorescence and Cherenkov light components (blue line), almost corresponds to the one, measured experimentally (red line at

the plot Fig.6.1). For comparison of the measured profiles to the theoretical Góra function this function is also shown at the plots.

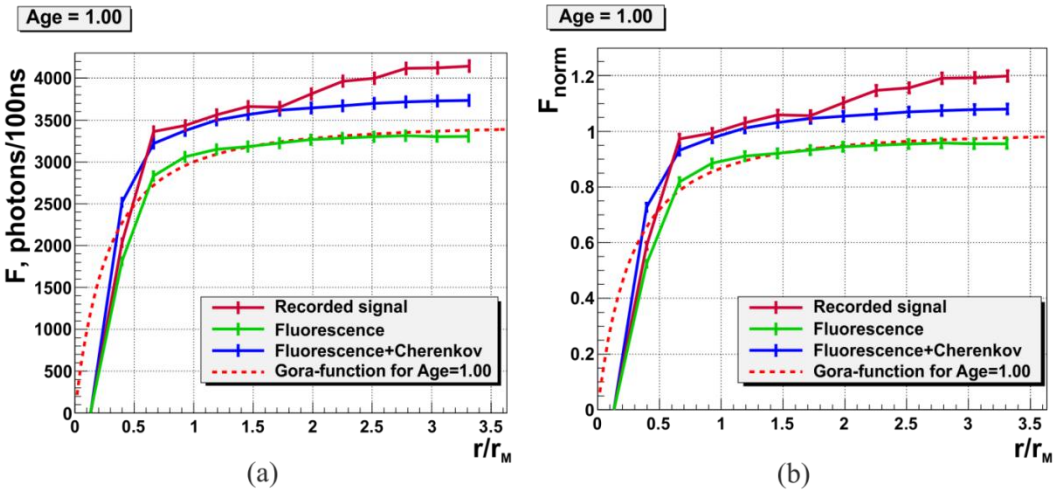

Figure 6.1: Fractions of light $F(r/r_M)$ (a) and normalized fractions of light $F_{norm}(r/r_M)$ (b) are represented vs. distance, expressed in Molière units. The profiles are shown for measured (red curve) and simulated showers of event 1 for age parameter $s = 1$ (blue curve – including the fluorescence and Cherenkov light contributions; and green curve – represented by the fluorescence light only). 100% of the fluorescence light emitted corresponds to $F_{norm} = 1$. Multiple scattering is included in all simulations. The red dashed line indicates the Góra function appropriate for this shower age.

The simulation of total light F_{norm}^{totSim} includes the following light components: simulated fluorescence F_{norm}^{flSim}, Cherenkov F_{norm}^{ChSim}, multiple scattering F_{norm}^{msSim}, and other possible light contributions F_{norm}^{x}:

$$F_{norm}^{totSim} = F_{norm}^{flSim} + F_{norm}^{ChSim} + F_{norm}^{msSim} + F_{norm}^{x}. \qquad [Eq.\,6.2]$$

In particular, the blue curve at (Fig.6.1) includes three of four discussed components (fluorescence, Cherenkov, and multiple scattering), the green one includes only fluorescence with multiple scattering from the fluorescence light correspondingly.

If all types of light are included, it is expected that the measured light F_{norm}^{data} (red curve in Fig.6.1) corresponds to the simulated one (blue curve in Fig.6.1, in this case if $F_{norm}^{x} = 0$):

$$F_{norm}^{data} \approx F_{norm}^{totSim}. \qquad [Eq.\,6.3]$$

When the profiles of total measured and simulated light are compared for various shower ages (Fig.6.2), one can notice that some of them (such as at $s = 1.05$, $s = 1.15$) agree rather well, whereas others (at $s = 0.95$, $s = 1.10$) are a little bit different. The difference, represented by various heights of the profiles, can be explained by existence of additional light in the measured shower profile, which can unexpectedly appear in FD camera field of

view, for example due to some atmospheric effects. The increase of the measured light at about s = 0.95 and s = 1.10 is also reflected in the correspondent longitudinal shower profile (Fig.4.6c) of this event.

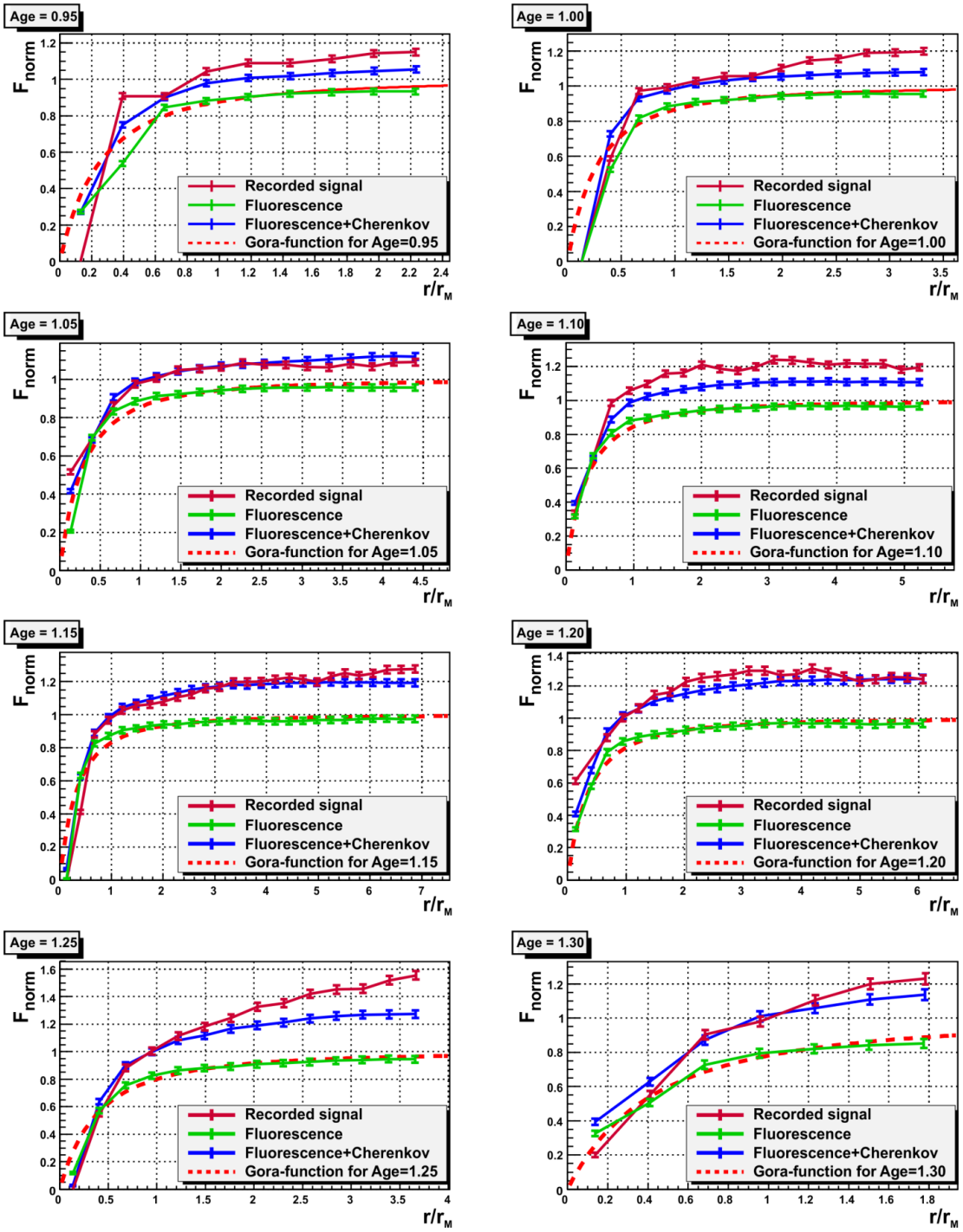

Figure 6.2: Normalized fractions of light $F_{norm}(r/r_M)$ are shown for several shower age parameters, as discussed before (for event 1). The red curves represent the measured shower, while green ones correspond to the simulated showers with fluorescence light only, and blue ones – to the simulated showers with fluorescence and Cherenkov light components. The red dashed line indicates the Góra function appropriate for the defined shower age. Multiple scattering is included in all simulations.

There are also some inconsistences in shape of the measured and simulated profiles (at $s = 1.00$, $s = 1.20$, $s = 1.25$, $s = 1.3$). They can be explained by some effects, which influence the measured light during propagation and registration. They may have different nature: telescopic, atmospheric etc.; and are discussed in detail in the following section.

Consequently, for proper studies of lateral distribution the additional effects should be included into analysis. If strange shape of shower profiles is impossible to explain, such ranges of shower age, or even the whole event, should be eliminated from the analysis.

6.1.1. Impact of the atmosphere and clouds on the shower optical image

As the atmosphere is a part of the extensive air shower detection system, its changes may cause changes in the shower shape. Thus, variations of the atmospheric pressure on the ground correspond to appropriate variations in the amount of matter, which the shower particles traverse, and therefore affect the longitudinal shower profile. On the other side, as the Molière radius is inversely proportional to air density, the decrease of the density leads to increase of the Molière radius and so extends the shower lateral profile. Therefore, the impact of the atmosphere onto shower development is implemented into the analysis. The atmospheric model is supplied to the system by means of a file in XML format.

So, the development of a shower depends on the properties of the atmosphere, particularly on the Molière radius, as the lateral distribution profile is wider or narrower, depending on r_M. Therefore, the reconstruction should be done using the same atmosphere. Since the effective Molière radius, describing the shower lateral distribution, should be calculated at the altitude of two cascade units above the given level (see section 2.2.2), there is a need to calculate the altitude h at the atmospheric density X (as it was shown in Fig.2.12). Therefore, different atmospheric models give different values of X at the same altitude. That is why, for consistency, the same model of atmosphere should be used in real and simulated showers, and X should be converted to h, using *Eq.* 2.6 - *Eq.* 2.7.

The selection of the appropriate model of atmosphere usually depends on the investigated location and the seasonably changing atmospheric parameters (pressure, temperature, etc.), typical for that place. Different atmosphere models are available for data analysis, among them: U.S. standard atmosphere [100]; monthly average atmospheres, strongly dependent on season, produced for the Pierre Auger Observatory experiment at Malargüe [67]; the Global Data Assimilation System (GDAS) atmosphere [68], which gives the atmospheric parameters, specific for certain hour and location.

For implementation of the specified atmosphere into data analysis the vertical atmospheric depth X_v, represented previously by *Eq.* 2.6, can be used as a parameterization function. This parameterization function allows fitting of atmospheric depth at 5 atmospheric layers (particularly, at 4 layers up to h = 100 km a.s.l. and at the 5th layer up to the upper atmospheric limit h = 112.8 km a.s.l.) [47]:

$$X_v(h) = a_i + b_i \cdot e^{-\frac{h}{c_i}} \qquad i = 1, \dots, 4, \qquad [Eq. 6.4]$$

$$X_v(h) = a_5 - b_5 \cdot h/c_5, \qquad [Eq. 6.5]$$

where a_i, b_i, and c_i are the fit parameters, specific for previously selected atmospheric model.

The parameterization *Eq.* 6.4 - *Eq.* 6.5 of the atmospheric depth is applied for conversion of the atmospheric depth X to the altitude h, as described above.

As atmospheric properties may change considerably with time and for different locations, the static US standard model and seasonally changing monthly average model are not accurate enough for precise shower lateral distribution studies. For this purpose the GDAS atmosphere should be used, as it is the most accurate model, with parameters determined every three hours. So, comparing the lateral profiles, calculated with GDAS, US standard and monthly average atmosphere models (Fig.6.3), it is clearly visible that the profiles, made using GDAS and monthly average models, are a little bit different, while the profiles for US standard atmosphere differ considerably at some stages of shower development (s = 1.2, s = 1.3). Such differences in profiles point out that of course the same atmosphere parameterization should be applied both for event reconstruction and simulation procedures for the proper lateral distribution analysis. As the GDAS atmospheric model describes best that atmosphere, in which the real shower is developing, this model is the most convenient parameterisation of the atmosphere. That is why it is used for event simulations and reconstructions in the current work.

For selection of events for the analysis, several standard cuts are usually applied for the dataset from the Pierre Auger Observatory. Among such basic cuts are limits on shower energy (starting from 10^{18} eV), fraction of Cherenkov light (less than 50%), rejection of the bad period FD data (the data, which for some reason cannot be used for physics analysis), selection of only hybrid events, etc. (description of cuts, generally used at the Pierre Auger Observatory, is given in [101]). However, such standard cuts are not enough for choosing events for lateral distribution analysis. The additional factor, which influences the selection, is also the existence of clouds in the telescope field of view. This is a strict criterion for the

current analysis, as presence of the clouds on the shower path strongly influences the shape of the lateral profile.

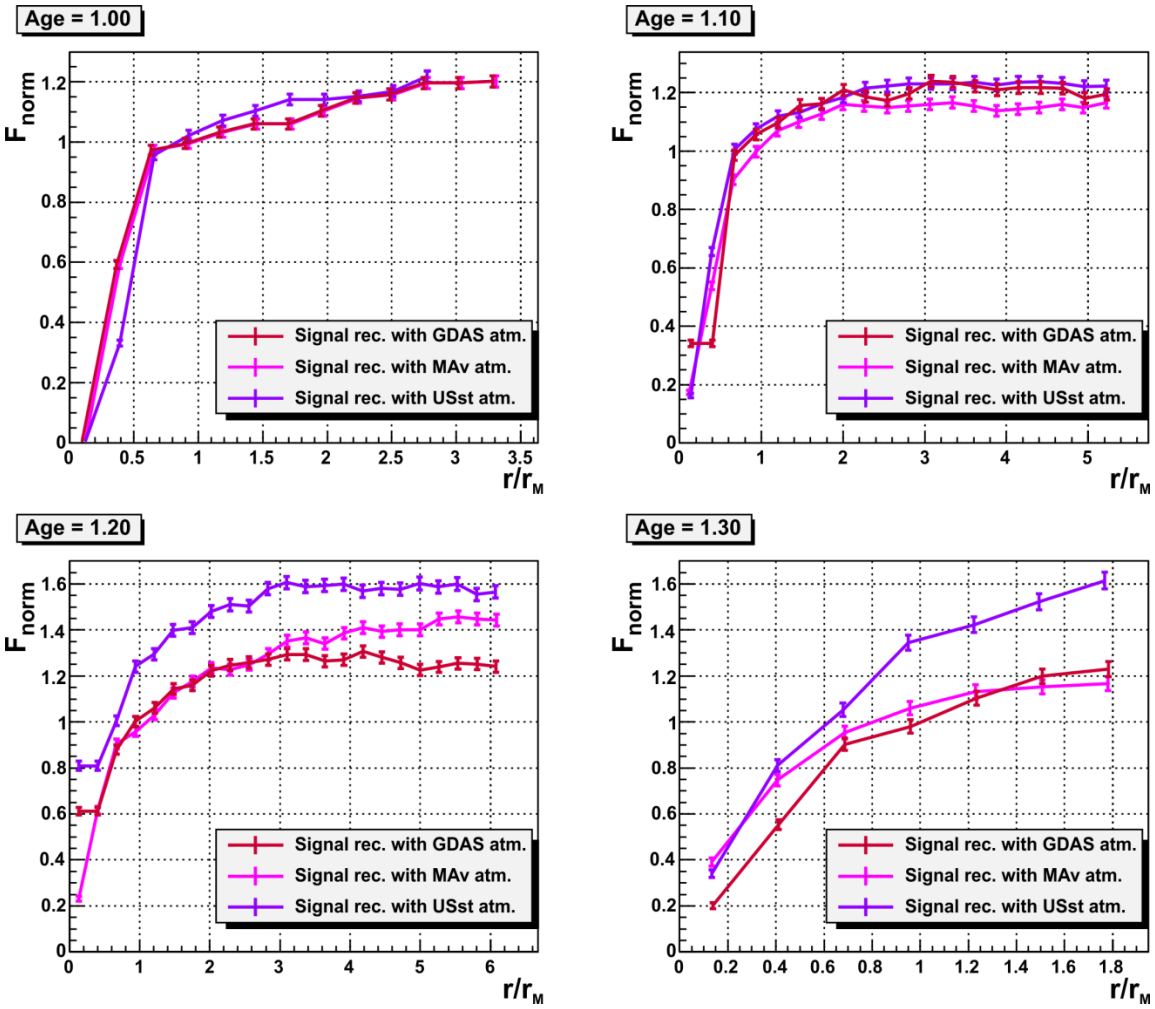

Figure 6.3: The profiles of lateral distribution of light (represented by the normalized fractions of light $F_{norm}(r/r_M)$), obtained from the real reconstructed shower, are shown for different atmosphere parameterisations for several shower age parameters (for event 1). The atmospheric models, used for lateral distribution analysis, demonstrated at this figure, include the GDAS parameterization (red line), Monthly Average (MAv.) and US standard (USst) atmosphere parameterisations (pink and violet lines correspondingly). The GDAS atmosphere is the most accurate one, and therefore should be used in the analysis.

For study of the cloud coverage the cloud cameras are used at the Pierre Auger Observatory. Their data enable the estimation of the cloud fraction (i.e. the part of a pixel field of view, covered by clouds (in %)). A full field of view set of cloud camera images is demonstrated within (Fig.6.4a). It includes a scan of the whole sky, which consists of the 27 images, and is provided by the infrared cloud camera every 15 minutes. Presence of clouds in the field of view is clearly visible at that figure. After processing of such images, the FD

camera pixels which see the clouds are identified (Fig.6.4b). Measurement of light for events, registered in such cloudy atmosphere, leads to the imprecise determination of shower profiles, and, therefore, such events are excluded from the data analysis of the current work.

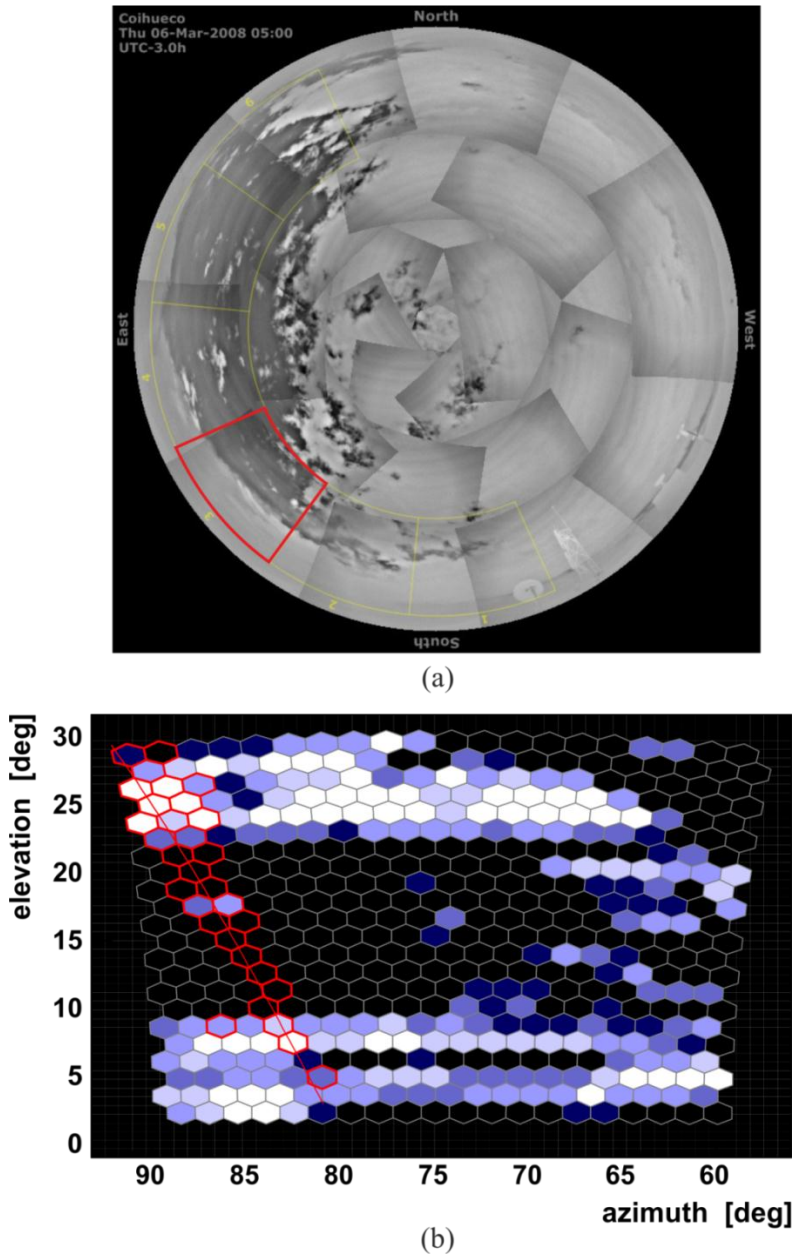

Figure 6.4: A set of the cloud camera images (a) for time moment, corresponding to the time of arrival of event #200806503688 to the detector field of view, is presented. Dense clouds are well visible in this figure. The red line in figure (a) limits the field of view of the camera 3 of Coihueco FD site, shown also at (b). Processing the data from cloud cameras allows estimation of cloud fraction in FD camera field of view (b): triggered pixels, forming shower trace, are indicated at camera (b) by red hexagons; pixels with clouds are graded by colours from white (100% of a pixel is covered by clouds) to dark blue (pixel cloud fraction constitutes 10%), and black coloured pixels are pixels without clouds.

In contrast to the situation, shown in Fig.6.4, the cloud camera sky view without clouds is shown in Fig.6.5. The absence of the clouds in the cloud camera field of view may indicate their absence in FD field of view, and consequently leads to determination of the undeformed lateral shower profiles (Fig.6.2).

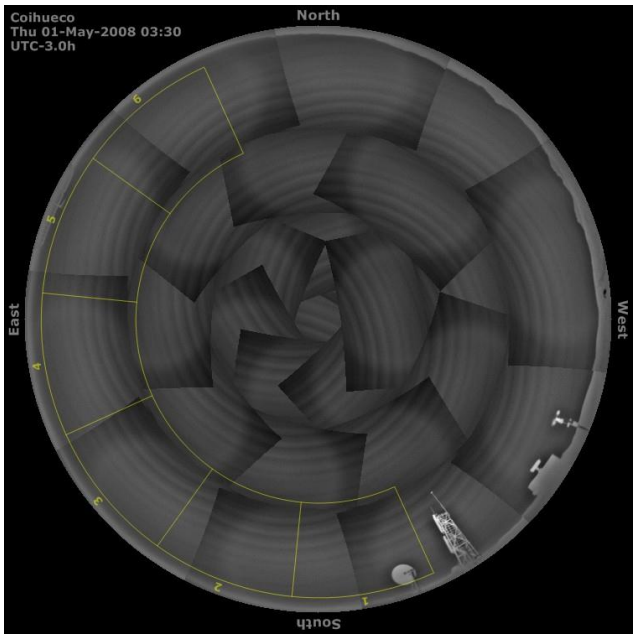

Figure 6.5: A set of the cloud camera images for time moment, corresponding to the time of arrival of event 1 to the detector field of view, is presented. No visible clouds are clearly seen in the cameras field of view. The whole sky view is composed of many photographs in infrared. The horizon is clearly seen at the figure, together with several Auger Observatory buildings (such as communication building), which are in the cloud cameras field of view.

One more example of presence of the clouds in the FD camera field of view is presented in Fig.6.6b. The 6 yellow rectangles in Fig.6.6a correspond to field of view of the 6 FD telescopes; the two red rectangles correspond to the telescopes 4 and 5, which see the discussed example event. Although there are no clearly visible clouds in the total view of the cloud camera images (Fig.6.6a), which are taken every 15 minutes, the precise cloud camera scans, processed for the FD field of view during every 5 minutes denote the existence of the clouds (Fig.6.6b). The clouds probably appeared in the detector field of view soon after the set of cloud camera images was done. These clouds influence much the longitudinal (Fig.6.6d) and lateral (Fig.6.7) shower profiles, since shower light reflected or absorbed by the cloud molecules results in the over- or underestimations of light in the shower profiles. This is visually seen as large fluctuations or waves in the profiles of the events with clouds. Thus, the signal observed in waves in Fig.6.7 drops because of the procedure of signal estimation (described in detail in section 5.2): when the background is

subtracted from the underestimated measured light, the ‘negative’ value of signal, inconsistent with its true expected value, is obtained.

Therefore, the clear sky without clouds is a strict and compulsory selection criterion for registered air showers, used for lateral distribution analysis in this work.

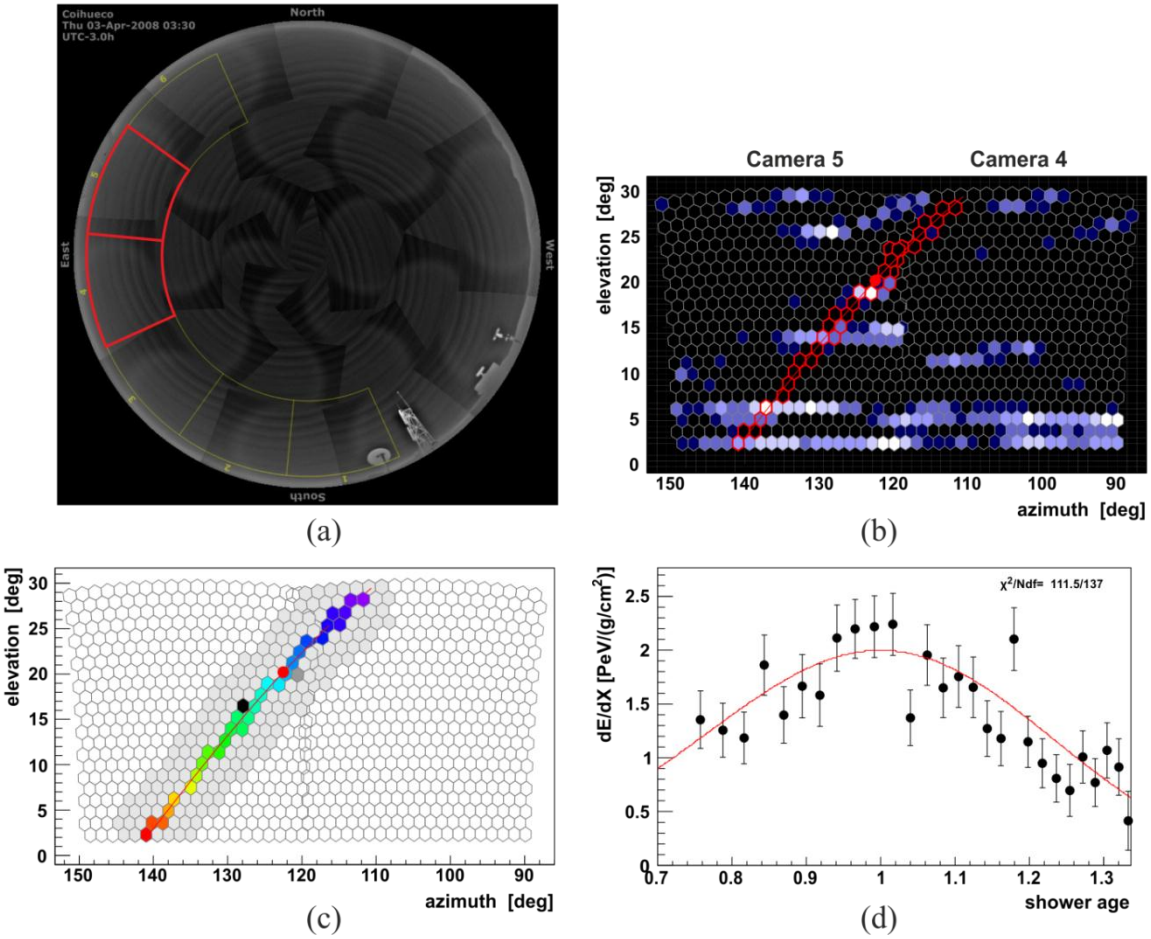

Figure 6.6: A set of cloud camera images (a) for time moment, corresponding to the time of arrival of event #200809303036 to the detector field of view, is presented. The red line at (a) limits two FD camera regions, shown in the following figures (b) and (c). Although there are no dense clouds in the composite image (a), produced every 15 minutes, some clouds are indicated in the FD camera pixels (b) of telescopes 4 and 5. These clouds may lead to significant fluctuations in measured longitudinal shower profile (d). Figure (b) is a more precise image of the region, limited red at (a). It can also be explained by the fact that cloud cameras, looking at the field of view of 6 FD telescopes (limited by the yellow line at figure (a)), scan the sky every 5 minutes, and so, can detect new clouds, coming to the detector field of view. In particular, this event had come to the detector 5 minutes after the set of photographs (a) was done by the cloud camera.

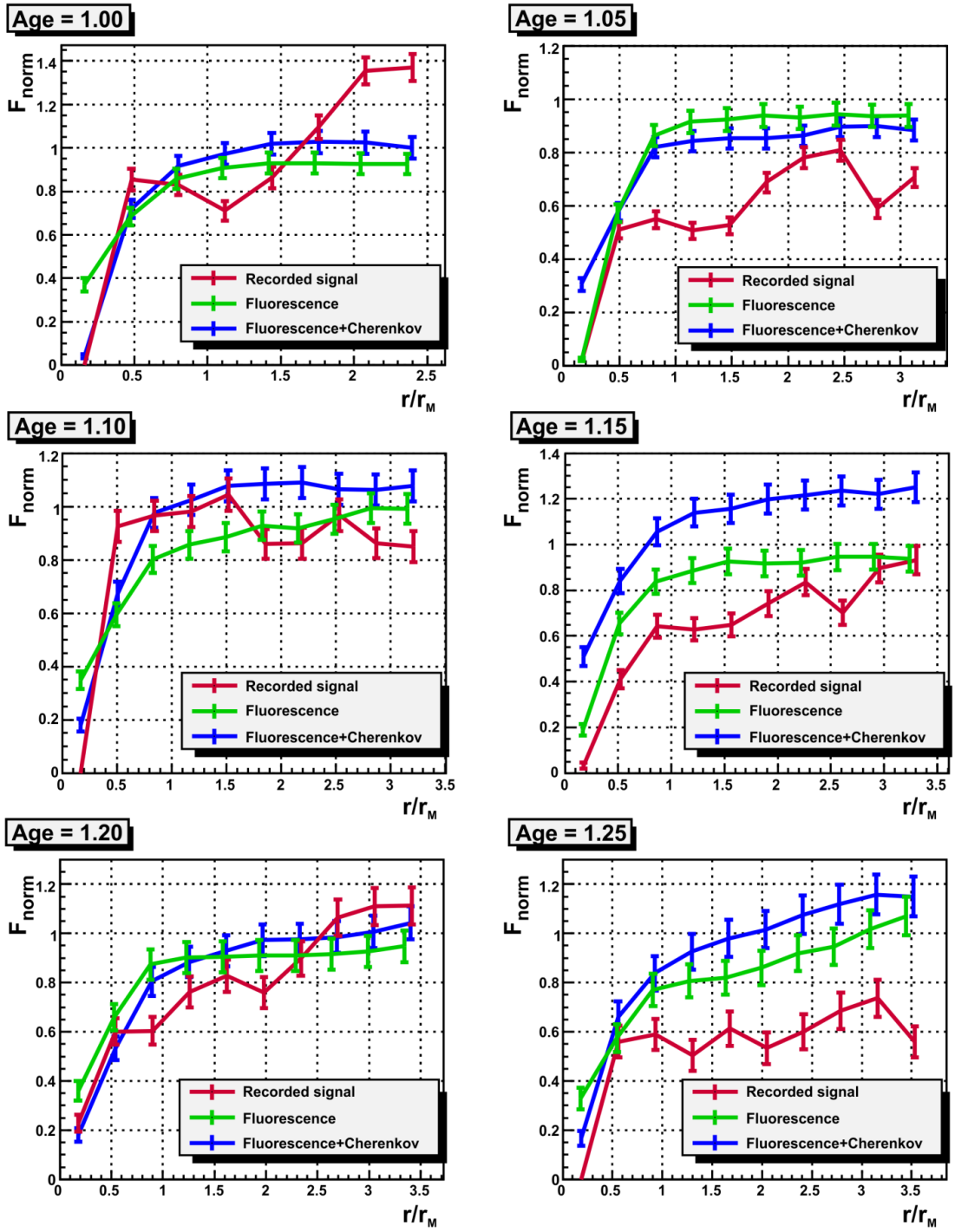

Figure 6.7: Lateral profiles of event #200809303036 with clouds in FD field of view are shown. $F_{norm}(r/r_M)$ denotes the normalized fractions of light, estimated for real (red line) and simulated (green line – the fluorescence component, blue line – the simulated fluorescence and Cherenkov shower components). Existence of a cloud in FD field of view may lead to waves in lateral shower profiles, measured for certain values of shower age parameter. If there were no clouds in the detector field of view, the red line should be approximately the same as the blue one.

However, sometimes there are very weak clouds, not seen at the cloud camera images. They result in the rise of large fluctuations in the longitudinal profile. In this case,

presence of such fluctuations may lead to significant waves in lateral profiles, and so the events with such longitudinal profiles should not be included into the lateral distribution analysis. Furthermore, the fluctuations may be caused by atmospheric effects difficult for prediction. As an example of such effect the variations in aerosol conditions can be given. The vertical density profiles of aerosols, their size, shape, and composition, change considerably with location and time (from hour to hour). If they are not measured precisely, the shower reconstructions may be wrong, and so is the lateral distribution.

After application of the mentioned cuts and conditions, several events were selected for lateral distribution analysis. In particular, among them there is an example event 1. Several other events are presented in Appendix B. Furthermore, the lateral profiles, shown in the following sections, are also provided for events, which satisfy the selection criteria.

6.1.2. Specifics of the shower lateral profiles measurements

As it is shown in Fig.6.2, even after including all the known atmospheric effects into analysis, the simulated profiles do not fully correspond to the ones measured experimentally. Some of the real event profiles (at $s = 1.00$, $s = 1.15$, $s = 1.25$, $s = 1.3$) have a visible increase of light at their tail. This effect can be explained by existence of the relatively large halo around the shower image. Although the halo's nature is not yet clear, it is considered to be a telescope effect.

The fraction of total light due to the halo is estimated to be about 18-20%. As it is a low intensity light, it is very difficult to distinguish its photons from the background ones. Therefore, for halo measurements an isotropic flashing UV point source of light was used at the Pierre Auger Observatory [102]. The flasher emitted short light pulses, which were further registered by FD. Those measurements have shown that halo light broadens the optical light spot. It was found that the angular range of ζ angle, over which the halo is detected, extends even up to 30 degrees, and so may cover the whole camera surface. During further measurements the halo light was discovered in all FD telescopes.

Using flasher data the cumulative distribution of halo signal (measured in 2008) was plotted in Fig.6.8. The obtained shape of the halo distribution may explain the increase in the tail of the light fraction for real measured events.

For explanation of the halo nature several its possible causes were proposed, among them: underestimated impact of the atmospheric multiple scattering; additional light, coming through the gaps in the corrector rings; the dust on the UV filters; reflections on the camera backside; effect of PMT glass reflectivity. Some of them were rejected as a possible

halo sources, others still are under investigation, but the significant contribution into halo fraction was only observed from PMT glass reflectivity effect. It is based on the fact that the reflectivity of the PMT, used in the telescope simulations (with value 8%), is too small, and should be increased up to 20%. That also means that the large part of photons (which contribute to halo) are reflected on the PMT's surface and afterwards in the mirror before being registered in the camera. After application of the new reflectivity values to simulations of the flasher light, up to 12% of light become understood. However, significant part (6-8%) of light still remains unexplained.

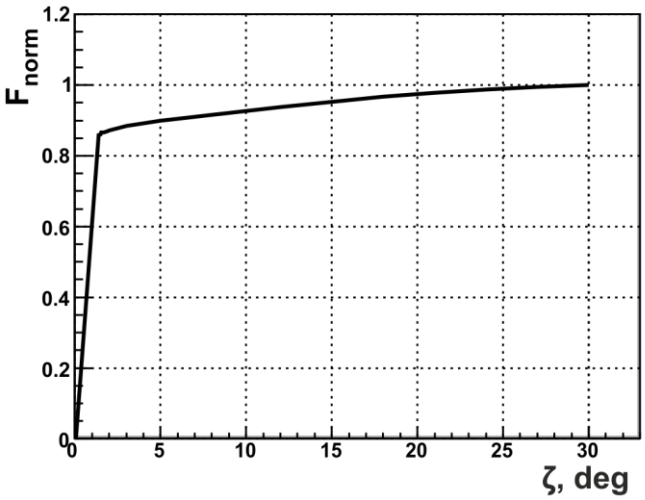

Figure 6.8: Cumulative distribution $F_{norm}(\zeta)$ of halo light in the image at the camera is plotted according to flasher data taken in 2008 [102].

Although the effects causing halo are currently under investigation, some of them are implemented in the developing module of the Offline Framework (in the TelescopeSimulatorKG_dev module), and can be used in real showers simulations. However, after performing such simulations it was discovered that this implementation influences the reconstruction, resulting in underestimation of shower energy. Therefore, to obtain the simulated profiles with halo included, the input shower energy (at CONEX input profile) should be rescaled. The lateral profiles, derived using this procedure are shown in Fig.6.9 together with profiles of real and simulated showers, presented earlier in Fig.6.2.

When the contribution of the halo light $F_{norm}^{haloSim}$ is included into the analysis, the formula (*Eq.* 6.2) for total simulated light F_{norm}^{totSim} can be rewritten as:

$$F_{norm}^{totSim} = F_{norm}^{flSim} + F_{norm}^{ChSim} + F_{norm}^{msSim} + F_{norm}^{haloSim}. \qquad [Eq. 6.6]$$

In this case, F_{norm}^{totSim} is represented by the orange curve, shown in Fig.6.9.

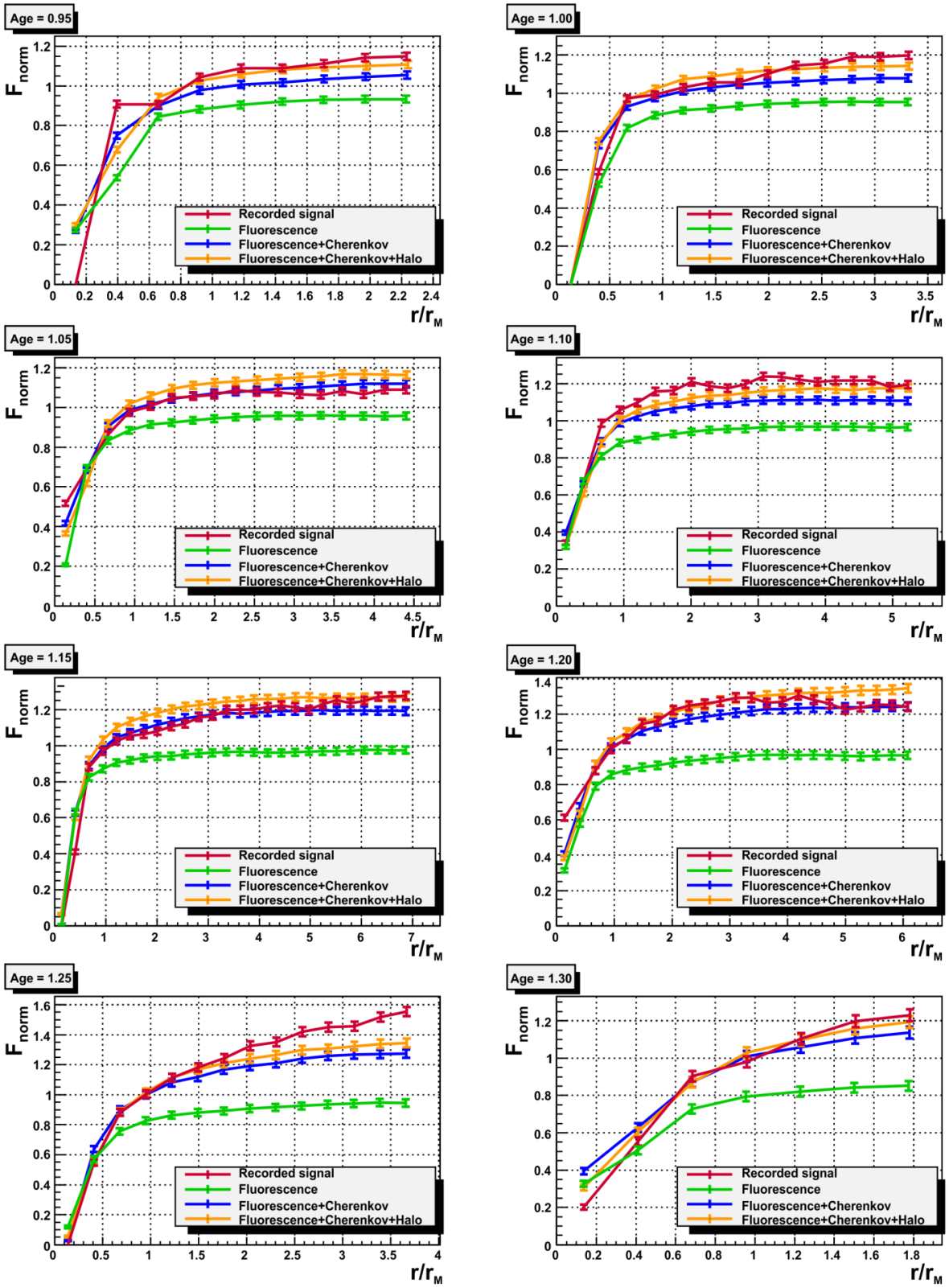

Figure 6.9: Normalized fractions of light $F_{norm}(r/r_M)$ are presented for measured shower (red curves) and simulated ones with only fluorescence light simulated (green curves), with fluorescence and Cherenkov light simulated (blue curves), and finally with fluorescence, Cherenkov and halo light simulated (orange curves). The profiles are derived for different values of shower age parameter for event 1. Multiple scattering light is included in all simulations.

As simulations with halo are in the developing phase, they give approximate results. However, even the approximate results are very similar to the real shower profiles (orange curve, representing simulations with halo in Fig.6.9 has almost the same shape as the red one, representing the real observed shower). Nevertheless, the simulations with halo are not perfect also because of the other factors, which may influence them: unclear nature of fraction of halo light (about 8%); any atmospheric effects; multiple scattering light, etc. The influence of these factors is usually observed in the longitudinal shower profile, as the fluctuations in data. If these fluctuations are essential even after rebinning of shower data (as in Fig.6.6d), the exact determination of the lateral distribution is not possible. At the same time, when data points are in good agreement with the Gaisser-Hillas curve (Fig.4.6c), the measured lateral distribution of light seems to be correct, and therefore its fluorescence component should correspond to the Góra function. These facts are going to be checked in the next section.

6.2. Test of the Góra function

The aim of the Góra function test is to check whether it really corresponds to the measured fluorescence fraction of shower light, and so whether there is dependence between the shape of measured lateral distribution and shower age. For this purpose, several steps are done. First of all, the measured and simulated profiles are taken for certain values of shower age parameter *s*. For this analysis the values of the age parameter are selected from the range 0.8 - 1.3 with the step 0.05. Secondly, the simulated profiles are described by the functions fitted to their data points, for the possibility to estimate the F_{norm} at each distance from shower axis r/r_M. Thus, the best fits to the simulated profiles are found, using the Góra function (Fig.6.10a). Finally, the approximate fractions of the measured fluorescence light are obtained from the real data in the way described below.

For convenience, the simulated light contributions should be represented by the functions fitted to them. Therefore, for estimation of total simulated light F_{norm}^{totSim}, its fitted function $F_{norm,fit}^{totSim}$ is further used (in Fig.6.10a it is a black curve fitted to the orange points, corresponding to the total light, simulated with halo contribution), so that $F_{norm}^{totSim} \equiv F_{norm,fit}^{totSim}$.

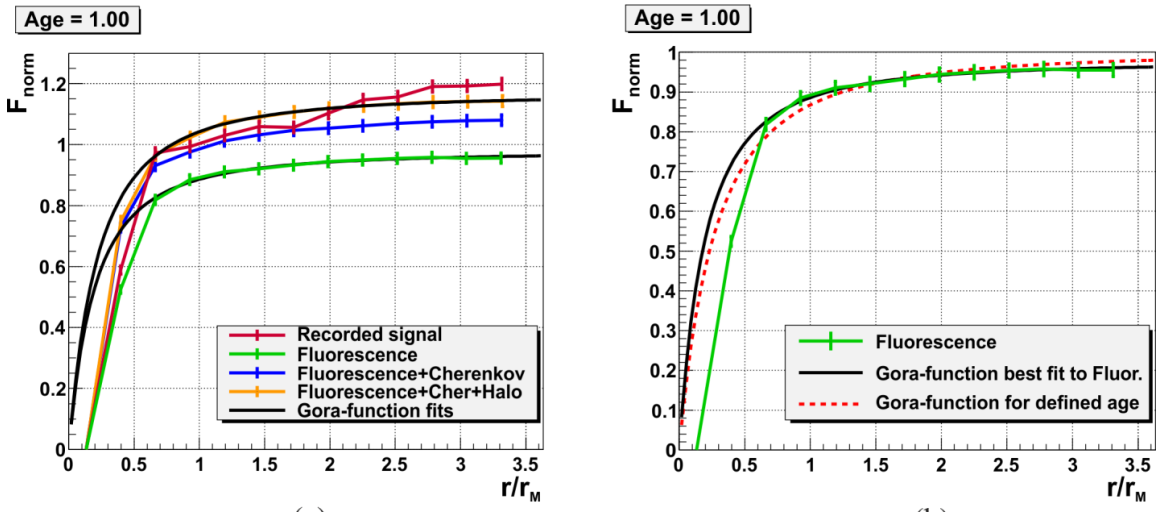

Figure 6.10: Normalized fractions of light $F_{norm}(r/r_M)$ (a) are presented for measured shower (red curve) and simulated ones (for event 1) for age parameter s = 1. The profile of simulated light, including the fluorescence and Cherenkov light, is indicated by the blue colour. The Góra function (black curves) is fitted to the simulated profiles, including the fluorescence light only (green curve) and total known simulated light with halo contribution (orange curve). Multiple scattering light is included in all simulations. The fit of the Góra function to simulated fluorescence light is shown together with the Góra function for defined age parameter at (b).

For the same reason a function is also fitted to the simulated fluorescence light only (in Fig.6.10a it is a black curve fitted to the green points, corresponding to the simulated fluorescence light only). In the following a function $F^{fl}_{norm,fit}$, describing the fit to the simulated fluorescence light, is implemented. It includes also multiple scattering from the fluorescence light $F^{ms\ flSim}_{norm}$, and so can be given by:

$$F^{fl}_{norm,fit} \equiv F^{flSim}_{norm} + F^{ms\ flSim}_{norm}. \qquad [Eq.6.7]$$

As a parameterization function, fitted to the simulated total and fluorescence light, the Góra function with free parameters was used, so that the fitted function has a somewhat different shape than the original Góra function for the defined shower age parameter (Fig.6.10b).

When the fractions of all contributions of shower light are known, the measured light F^{data}_{norm} (red curve in Fig.6.10a) should correspond to the simulated one F^{totSim}_{norm} (*Eq.* 6.3). So that the total measured light should also include all the components, enumerated in the simulated light, and these components should have approximately the same fractions as the simulated ones have:

$$F^{data}_{norm} \approx F^{fl}_{norm} + F^{Ch}_{norm} + F^{ms}_{norm} + F^{halo}_{norm}. \qquad [Eq.6.8]$$

The main task of this test is to check the correspondence between the measured F_{norm}^{fl} fluorescence light and the Góra function. For this purpose it can be assumed that the simulations of other components of total light are performed correctly, so that the simulated components correspond to their contributions in the measured light, i.e. $F_{norm}^{Ch} \approx F_{norm}^{ChSim}, F_{norm}^{ms} \approx F_{norm}^{msSim}$, $F_{norm}^{halo} \approx F_{norm}^{haloSim}$.

However, it is impossible to measure separately all mentioned components of total simulated light, and F_{norm}^{fl}, in particular. But it is feasible to provide simulations of the fluorescence light only or with addition to it any needed set of components (so as it is shown in Fig.6.10a: green curve - representing fluorescence light with multiple scattering, or blue curve - indicating the fluorescence, Cherenkov, and multiple scattering light). Therefore, to extract the fraction of the fluorescence light from the measured data, the total simulated light should be subtracted from the measured one, and then the simulated fluorescence light (with its multiple scattering) should be added. Using the fitted functions the measured fluorescence light can be given by:

$$F_{norm}^{fl} = F_{norm}^{data} - F_{norm,fit}^{totSim} + F_{norm,fit.}^{fl} \qquad [Eq.\,6.9]$$

After application of this formula to the measured and simulated data the profiles of measured fluorescence light can be plotted (Fig.6.11).

The fit of the Góra function to the profile of fluorescence light, obtained from data, gives the values of the shower age parameter s_{fit}, which can be compared to the expected values s_{exp}, calculated using formula *Eq.* 2.10, i.e. $s_{exp} = \frac{3X}{X+2X_{\max}}$.

The approximate depth of shower maximum can be found from *Eq.* 2.10, knowing the fitted shower age parameter s_{fit}:

$$X_{\max} = \frac{X(3 - s_{fit})}{2s_{fit}}. \qquad [Eq.\,6.10]$$

It can be compared with shower maximum, estimated from the Gaisser-Hillas fit (particularly, equal $X_{\max} = 699 \pm 9$ g/cm^2 for the example event 1). From Fig.6.11 it can be deduced that the fitted shower age and $X_{\max}$ values of some measured profiles are in a good agreement with the expected values. At the same time there are values, which do not agree at all. This fact can be explained by over- or underestimation of measured light during analysis procedure, or by pixels having for some reason a larger or smaller fraction of light than it was expected for the defined moment.

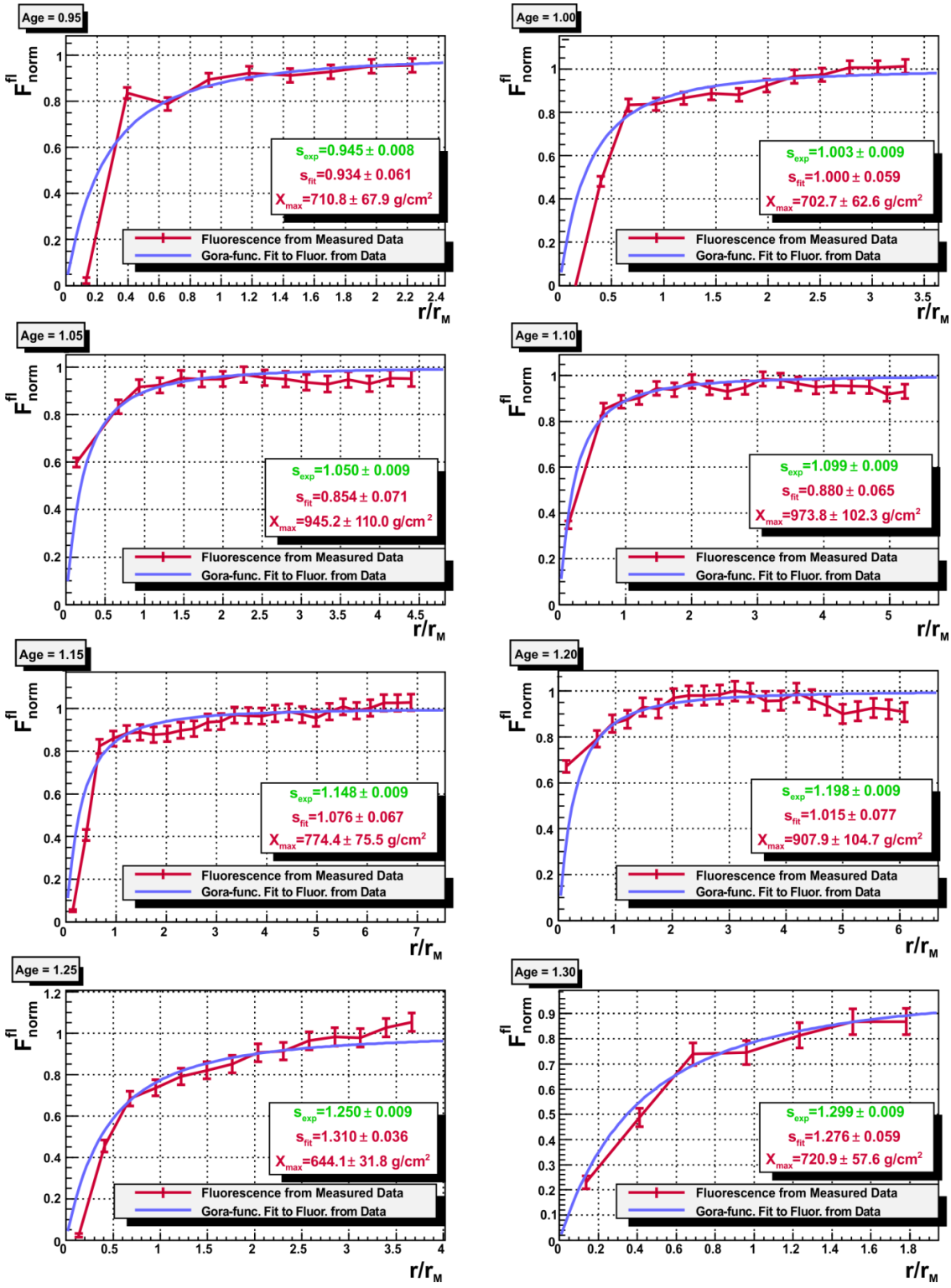

Figure 6.11: Normalized fractions of fluorescence light F_{norm}^{fl} (pink curves) derived from the measured data are presented for defined shower ages (for event 1). The Góra function (blue curves) is fitted to the profiles of fluorescence light, obtained from data. The approximate values of shower age s_{fit} are found from fit, giving the approximate $X_{\max}$ values. The expected shower age values s_{exp}, obtained from the formula *Eq.* 2.10, are shown for comparison. The depth of shower maximum determined from the Gaisser-Hillas fit for this event is $X_{\max} = 699 \pm 9$ g/cm^2.

One of the reasons of the not exact estimation of s and X_{max} values is a selection of the circle with probably wrong radius for light collection on the FD camera. Up to this moment the largest possible radius was used for analysis in this work. However, sometimes at several stages with the large circle radius there are pixels in the circle (white pixels in Fig.6.12 in the large circle, drawn for s = 1.2), the signal for which was not saved into the database. It is expected that the signal in them is fluctuating around zero, and so does not contribute much. For this reason the study of the signal within the circle of the large radius, was provided in the previous parts of this work. Nevertheless, inclusion of such pixels into the circle may result in underestimation of the signal in that circle. Therefore, the smaller circle which covers the pixels with signal is taken for the further analysis (Fig.6.12).

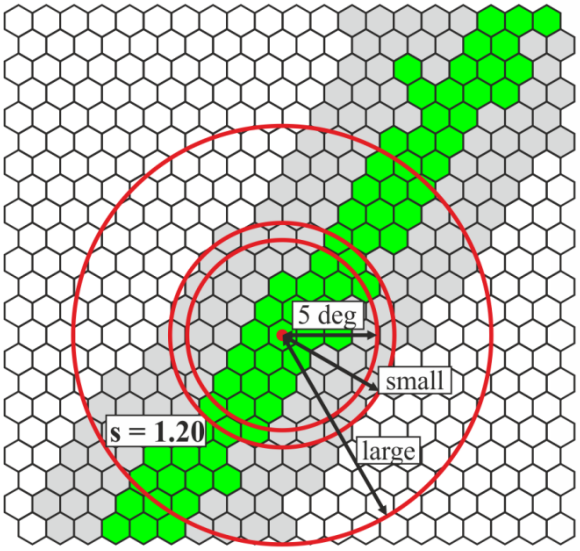

Figure 6.12: The area of light collection for certain stage of shower development (s = 1.2) is limited by the circle. The circle of a large radius includes the pixels without signal (white ones). The circle of the small radius includes all the pixels, which have a signal (grey and green). The circle of the radius equal 5 degree includes the pixels with signal and excludes the pixels with possible large halo contribution.

The profiles of measured fluorescence light for which the change of the radius to the smaller one is essential are shown in Fig.6.13. A comparison with Fig.6.11 shows that such change improves considerably the parameter values.

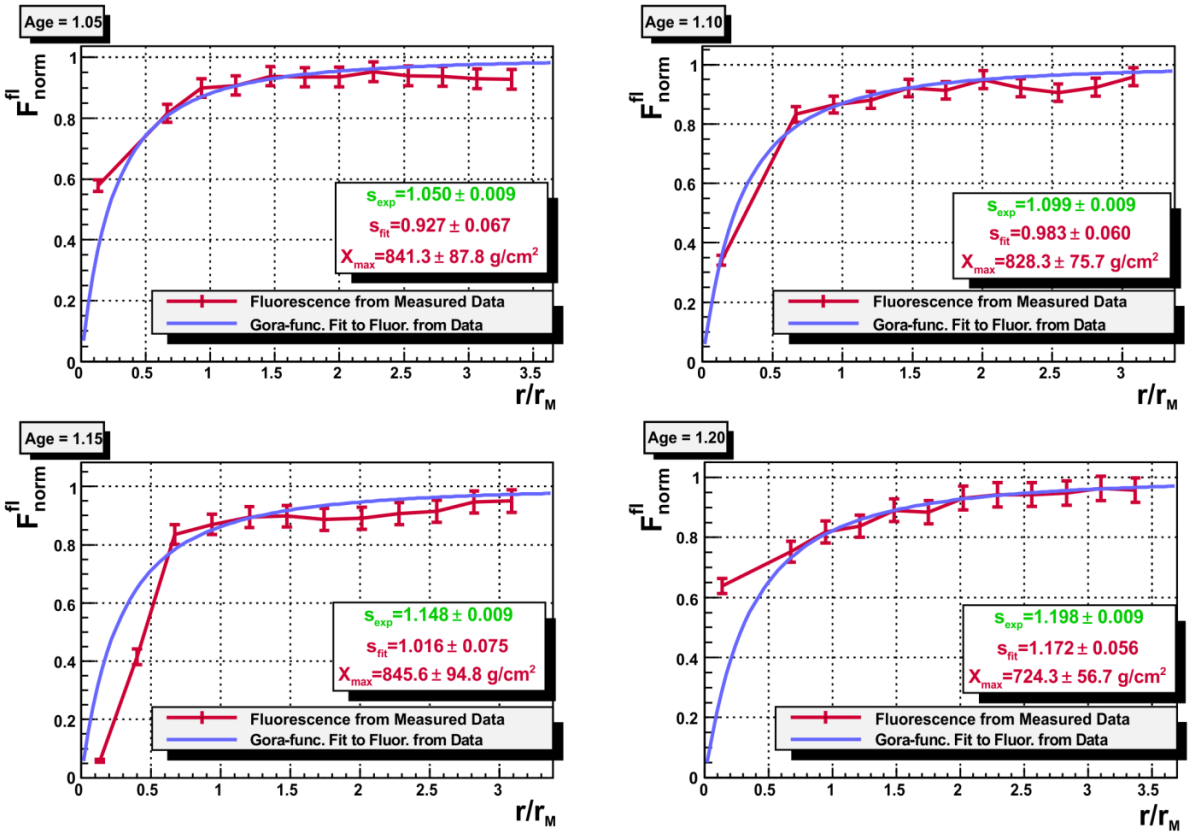

Figure 6.13: Normalized fractions of measured fluorescence light F^{fl}_{norm} (pink curves), determined in the circle of smaller radius (see Fig.6.12), are presented together with shower parameters found using the Góra function fits (blue curves) for several selected age parameters for event 1. The depth of shower maximum determined from the Gaisser-Hillas fit for this event is $X_{\max} = 699 \pm 9$ g/cm^2.

According to the first measurements of halo it can be assumed that the halo light contribution grows noticeably when the radius of the circle, in which the light is collected, is larger than 5 degree. Therefore, as simulations with halo are only in the developing phase, and so the data may have uncertainties caused by simulations, it is worth also to estimate the light fraction within the circle with radius of 5º, using the reliable standard simulation procedure, not including halo. The profiles of measured fluorescence light, plotted for this case, are shown in Fig.6.14 together with the following calculation of the shower parameters. These parameters are in better agreement with the expected values than those obtained from the profiles, representing the total simulated light with halo contribution, collected within the small radius. The examples of such profiles, measured for other events, are shown in Appendix C. They support the results obtained for example event 1.

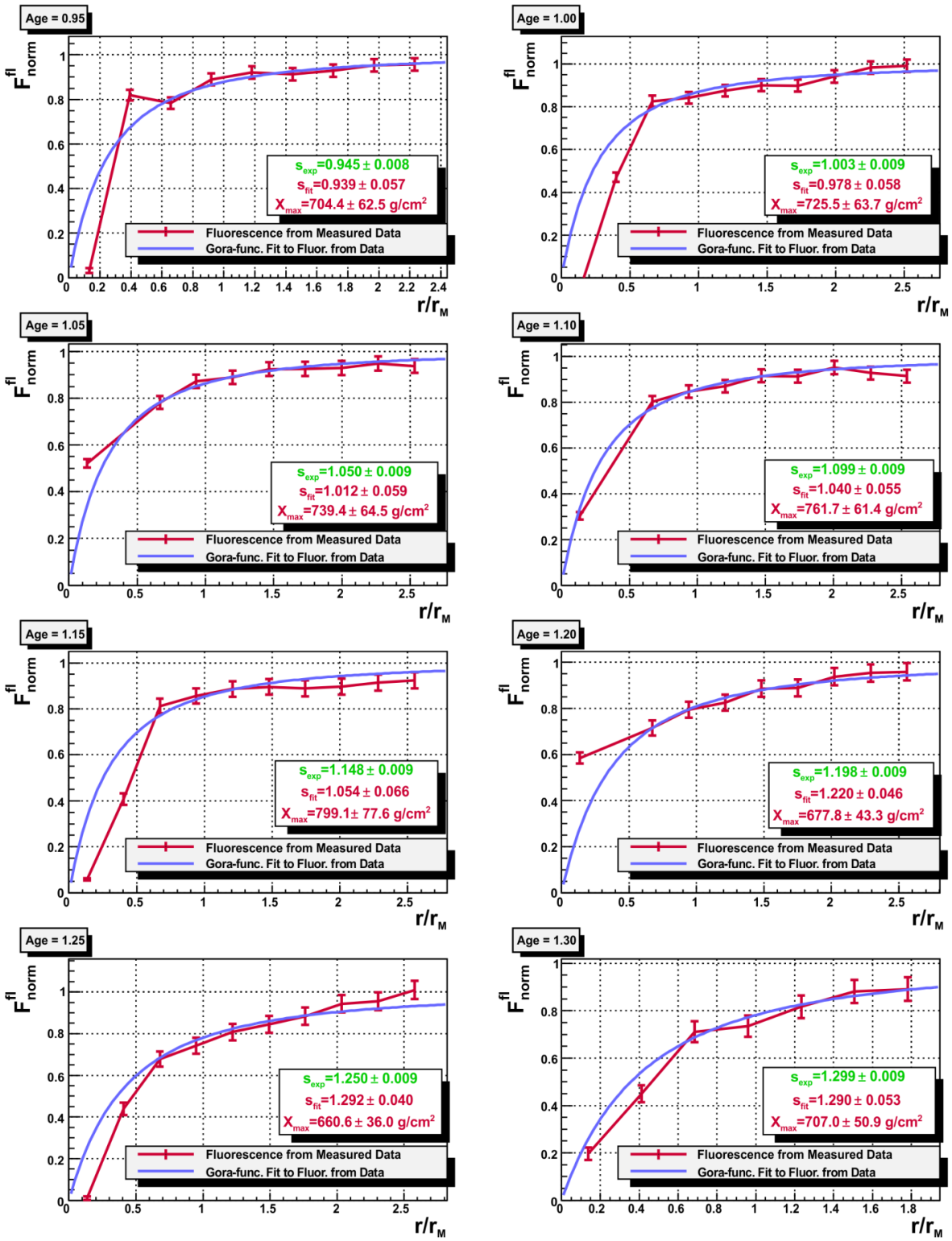

Figure 6.14: Normalized fractions of measured fluorescence light $F_{norm}^{fl}(r/r_M)$ (pink curves) are plotted for circle radius equal 5 degree for defined shower ages (for event 1). The Góra function (blue curves) is fitted to the profiles of fluorescence light, obtained from data. The approximate values of shower age parameters and $X_{\max}$ are found and presented at the figure. The depth of shower maximum determined from the Gaisser-Hillas fit for this event is $X_{\max} = 699 \pm 9$ g/cm^2.

So, use of the 5 degree cut on the circle radius gives much better values of shower age, and consequently shower maximum. However, the calculation of these parameters still is not perfect for some profiles (for example, at s = 1.10, s = 1.15), that is also reflected in the corresponding region of the longitudinal profile (Fig.4.6c). This fact can be explained by the increase of the light fraction in measured light, because of any atmospheric or telescope effect. Therefore, when choosing the stages for shower age determination, those regions of longitudinal profiles, where the measured data deviate from the Gaisser-Hillas curve, should not be taken to the analysis. It is better not to take them into account, as the profiles, obtained from them are uncertain and give wrong results.

Other Auger events were analysed in the same way (so that the total number of events taken to the analysis is ten). The profiles of measured fluorescence light are obtained for them and shown in Fig.6.15. Profiles of all events available for a given age are plotted together and compared to the Góra function for the particular ages. It is seen that the fractions of measured fluorescence light for different shower ages keep the shape, corresponding to the shape of the Góra function.

To check whether the values of s_{exp} and s_{fit} (and correspondingly their $X_{\max}$) agree to each other, the difference between these values is calculated for each good event discussed in this work for each available shower age (Fig.6.16).

From Fig.6.16 it can be concluded that generally the Góra function describes well the data. So, as the shape of the fluorescence light distribution for measured showers corresponds to the shape of the Góra function at different shower ages, the test of the Góra function gives a positive result.

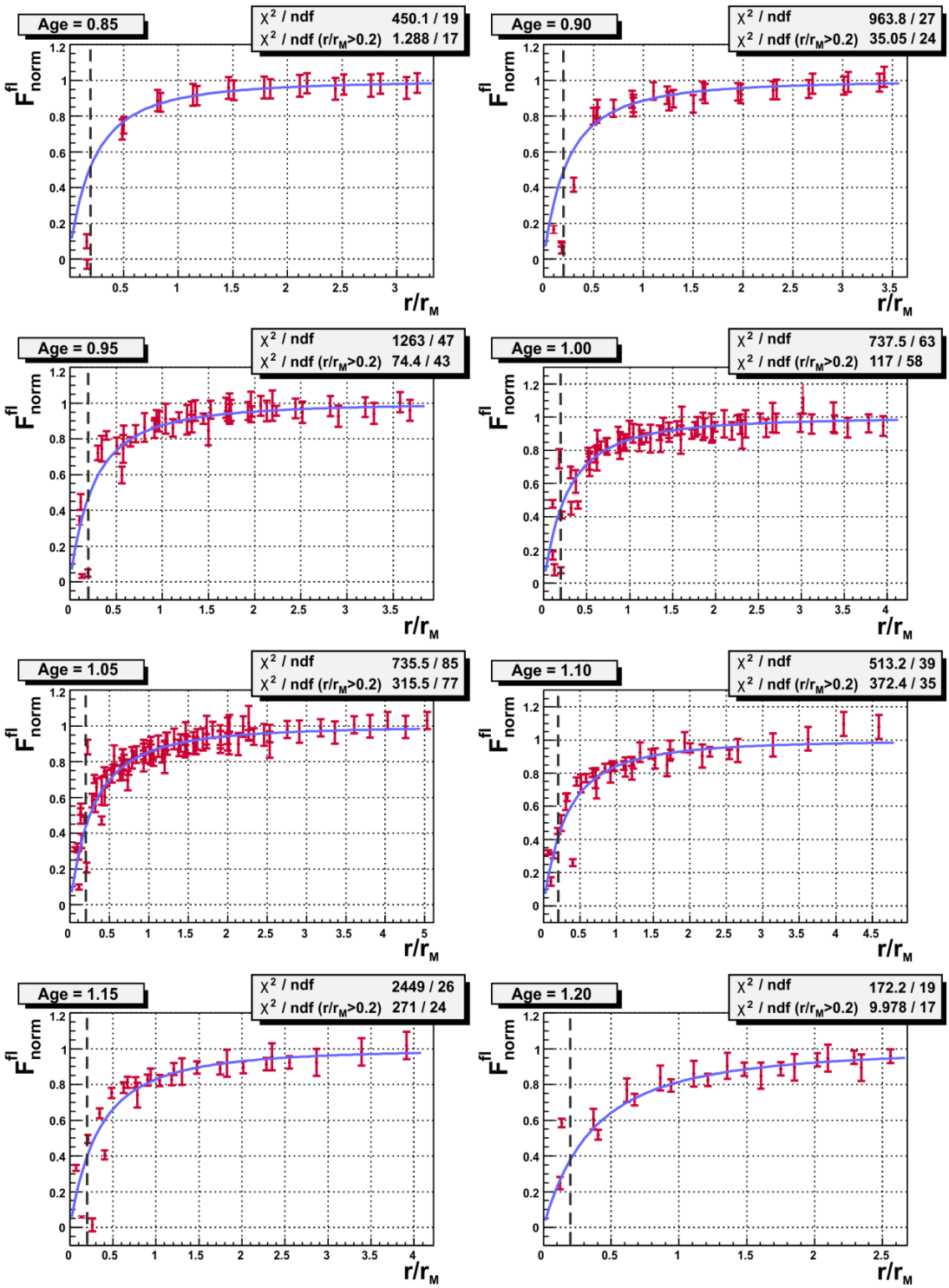

Figure 6.15: Normalized fractions of measured fluorescence light $F_{norm}^{fl}(r/r_M)$ (pink curves) are shown for several events for the defined shower age parameters. The numbers of Auger events used for the analysis for each shower age, varies from 2 to 10, depending on the number of profiles available at each event for the specified age. The blue lines correspond to the Góra function, appropriate to each age. χ^2/ndf is estimated for the total range and for the points (limited by the dashed line) with $r/r_M \geq 0.2$ (i.e. excluding the points with signal measured at the central pixel of the circle. As the signal was measured with the step 0.5º, and the pixel size is 1.5º that may lead to uncertainties in the signal measurement in the central pixel).

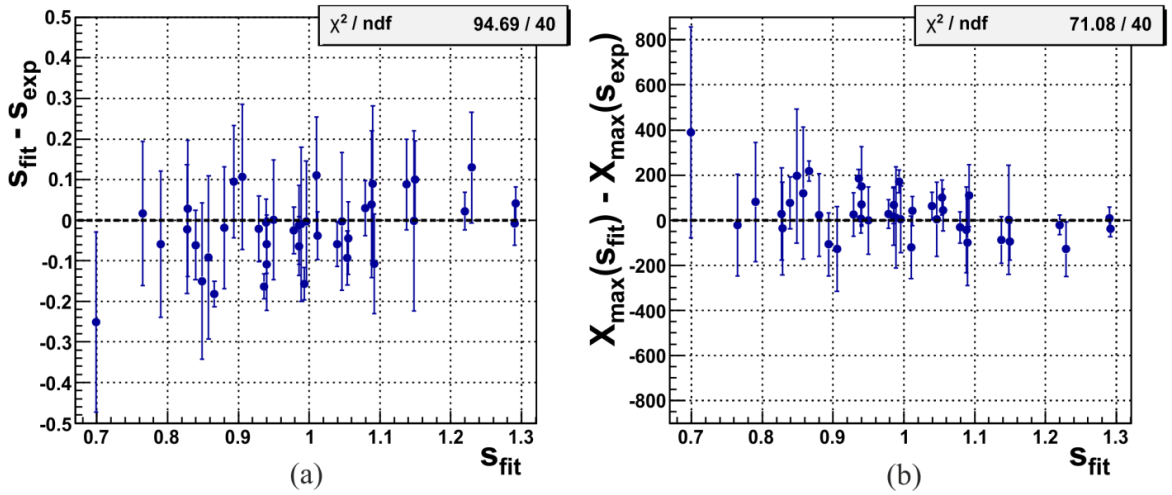

Figure 6.16: The difference between the values s_{exp} and s_{fit} (a) is varying near zero that points out at the correspondence between their values. Correspondingly, the difference of the $X_{\max}$ values of these age values (s_{exp} and s_{fit}) is shown at (b). The dashed black line corresponds to the Góra function, and the points represent the deviation from this function.

6.3. Study of the method of $X_{\max}$ determination, using shower optical image

According to *Eq.* 2.10 and *Eq.* 6.10, there is a correspondence between shower age s and shower maximum $X_{\max}$. So, knowing one of these values, it is possible to find the other. Therefore, it is possible to obtain $X_{\max}$ by estimation of shower age from the fit of the Góra function to the measured fluorescence light.

The test of the Góra function was provided for selected stages of shower development, i.e. for known values of shower age, obtained using the fit to longitudinal profile. This was needed for the test. However, such kind of selection cannot be used as a separate method of $X_{\max}$ determination, as shower age is not known a priori and has to be determined from the measured data. Therefore, the lateral profiles should be selected according to other variable, which changes together with shower development, such as the atmospheric depth X.

The atmospheric depth can be found from the profiles of the atmosphere, using the parameterization, described in section 6.1.1 (*Eq.* 6.4, *Eq.* 6.5). Therefore, the lateral light distribution can be measured at certain values of atmospheric depth X (Fig.6.17). Then, the measured fluorescence light is estimated (Fig.6.18), according to the procedure described in the previous section, and the Góra function is fitted to this light (for fractions of light, estimated at certain X for several other example events, see Appendix D).

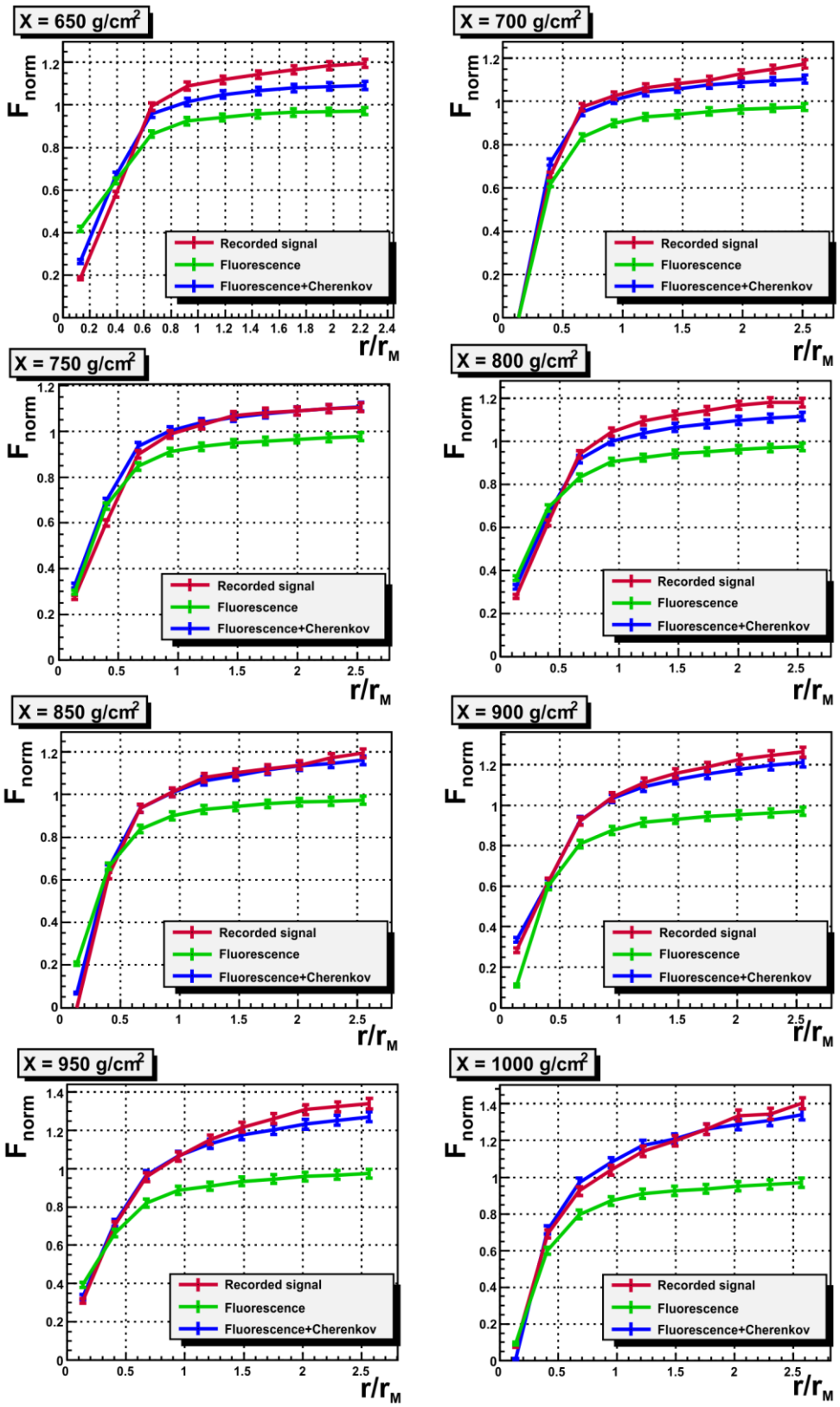

Figure 6.17: Normalized fractions of light $F_{norm}(r/r_M)$, collected in the circle with radius equal 5 degree, are presented for measured (red curve) and simulated showers (blue curve – including the fluorescence and Cherenkov light contributions; and green curve – represented by the fluorescence light only) of event 1 at the defined stages of shower development, corresponding to the appropriate values of atmospheric depth X. Multiple scattering is included in all simulations.

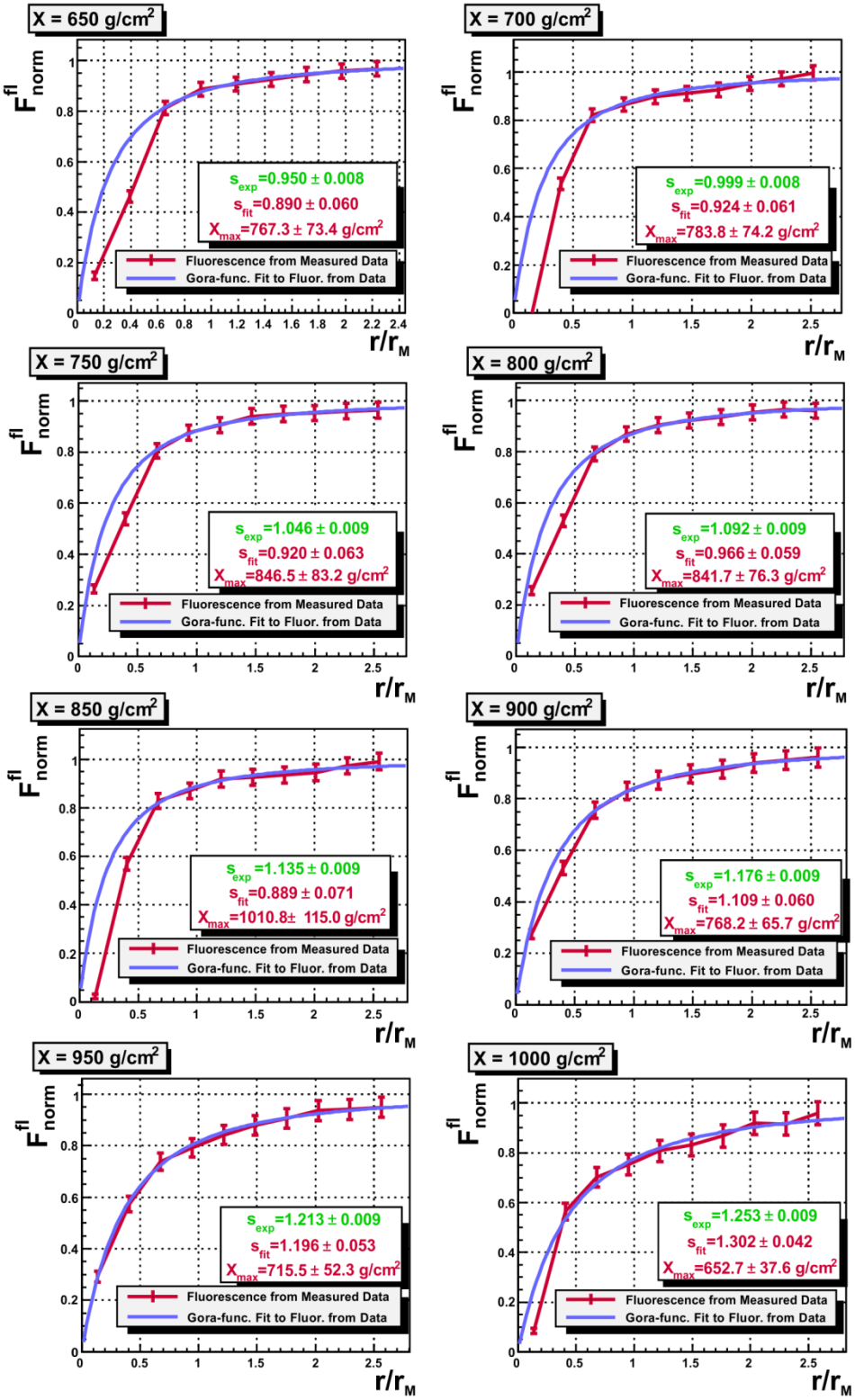

Figure 6.18: Normalized fractions of measured fluorescence light $F_{norm}^{fl}(r/r_M)$ (pink curves), collected in the circle with radius equal 5 degree, are shown for event 1 at the defined stages of shower development, corresponding to appropriate values of atmospheric depth X. The approximate values of shower age s_{fit} are found from fit, giving the approximate X_{max} values. The expected shower age values s_{exp} are also shown for comparison. The depth of shower maximum determined from the Gaisser-Hillas fit for this event is $X_{max} = 699 \pm 9$ g/cm^2.

Knowing the shape of the lateral distribution of fluorescence light, the shower age can be further found. So, using the Góra function with the free parameters, the shower age parameter s_{fit} is obtained from the fit. Finally, the depth of shower maximum can be calculated using *Eq*. 6.10.

The expected values of shower age s_{exp} are calculated, using formula *Eq*. 2.10. As it was already mentioned above, some obtained values of shower age s_{fit} do not correspond to expected parameters s_{exp}. This can happen as measured data may be influenced by many unpredictable atmospheric effects, occurring at the corresponding development stage. The inconsistence between the data points of measured longitudinal profile and its fit (Fig.4.6d) is also reflected in the incorrect shower age determination at some stages (for example, as it is shown in Fig.6.18 at X = 800 g/cm^2, X = 850 g/cm^2). For stages, where the data points are located on the Gaisser-Hillas curve, the shower age parameter and shower maximum are determined correctly within error values.

Giving the possibility of the shower maximum estimation, the method discussed here can be applied for determination of $X_{\max}$ for events with maximum outside the detector field of view (such as event 5, presented in Appendixes in figures B.4, C.4, and D.4).

Although $X_{\max}$ determination is still not much precise (because of large errors on s and $X_{\max}$), the discussed method allows obtaining the values of shower age parameter and shower maximum independently on the other methods. As demonstrated above, in good observation conditions the obtained parameters are very close to those found using the other method (the Gaisser-Hillas fit to longitudinal profile). This allows us to state that the method of $X_{\max}$ determination, using the Góra function, is perspective for further development.

In addition, this method indicates the fact that the Góra function corresponds to the measured fraction of fluorescence light, and so it is universal, depending on the shower age parameter and distance from shower axis only. At the same time, this method can also contribute into estimation of the composition and energy of cosmic rays, using the measured $X_{\max}$ values.

7. Conclusion

The properties of the shower optical image were investigated in this work, in particular, the study of the lateral distribution of the light within the shower optical image, including the estimation of its angular size.

The shower light often comes to several pixels simultaneously. However, as the shower image is almost always larger than the pixel size of the fluorescence detector of the Pierre Auger Observatory, a part of the signal goes to pixels with the signal values below the trigger threshold, and so is lost, leading to an underestimation of the shower energy. To avoid the signal loss, the lateral distribution of light should be used to recuperate the signal in the subthreshold pixels. This is done with the Góra function, but this function has not been verified experimentally so far. The actual measurement of the Góra function was done for the first time in this work for showers registered by the fluorescence detectors of the Pierre Auger Observatory.

The measured lateral distributions of light in the shower image were compared to the simulated ones, obtained using the real simulation method. These distributions are expected to be the same. Nevertheless, in many cases it was not so, as the fraction of light, determined for simulated showers (including all known light components, i.e. fluorescence, Cherenkov and multiple scattering light) was generally smaller than the fraction of total light in measured events. This underestimation of light can be explained by the presence of the halo light in the shower optical image. The lateral profiles, obtained from simulations, including the halo light, seem to solve this problem. However, as the nature of the halo still is not completely clear, the simulations of the halo light are in the developing phase now, and therefore are not much reliable. So, the ordinary (not including the halo) procedures were used for simulation of the showers. After that the distribution of light was measured in the circles of 5 degree at different stages of shower development to study the lateral distribution in the region, which is expected to contain none (or low) fraction of halo light.

In this work it was discovered that there are several important factors, which influence and distort the shape of the lateral distribution. So, only events recorded without presence of clouds are eligible for the lateral distribution analysis. Moreover, it was noticed that large fluctuations in the data in the longitudinal profiles also indicate possibility of large distortions in the lateral profiles. Such fluctuations may be a result of a presence of undetectable clouds in the detector field of view. In addition, a correct atmosphere parameterization was needed for the analysis procedure, as the atmosphere influences much the shape of the profiles.

The lateral distribution of fluorescence light in shower image can be parameterized by the Góra function. This phenomenological function was used for simulation of the fluorescence light distribution in the Auger Offline framework. This function is universal, as it depends on the shower age parameter and distance from shower axis only. This dependence was checked in this work using the fraction of the measured fluorescence light. For this purpose, the fluorescence light was extracted from the total measured light, using the Monte Carlo simulations. So, the test of the Góra function was performed for various age parameters of showers. The test had shown quite a good agreement for events, which are not much influenced by the atmospheric and telescope effects. It was observed that such events had good fits of the Gaisser-Hillas function to the longitudinal distribution data points. In particular, the test has shown experimentally the existence of the dependence of the measured lateral distribution on the shower age.

As the Góra function gives the possibility to estimate the shower age and consequently the depth of shower maximum, based only on the distribution of the fraction of fluorescence light, the method of determination of s and $X_{\max}$ parameters was elaborated. Using this method, the approximate values of these parameters were found, which are in a good correspondence with their expected values. At this moment the discussed method does not give better results of estimation of the depth of shower maximum, than the method, which uses the longitudinal profiles for this purpose. But it is an independent method of shower maximum estimation, which has given the first good results. That is why this method is perspective for further developing and should be studied in more detail. It may give better results in future, when, for example, the fraction of the halo light in the total light will be exactly known.

As a final point of this work it should be stressed that when the lateral distribution of the measured fluorescence light is known, it is possible to determine the exact distribution of light around shower axis, and so to find more accurately the values of shower energy. In such a way, a precise measurement of the lateral distribution of light in shower optical image, provided in this work, can contribute to the shower energy estimation, and so improve the fluorescence detection technique of extensive air showers.

Appendixes

Appendix A

The sequences of modules, specific for reconstruction and simulation procedures used in Auger Offline software, are presented in Appendix A.

Appendix A1

A module sequence, typical for standard hybrid reconstruction, is presented. It is used as one of the input files (ModuleSequence.xml) in the Offline software.

```
<sequenceFile>
    <enableTiming/>
    <moduleControl>
        <loop numTimes="unbounded" pushEventToStack="yes">
            <module> EventFileReaderOG </module>
            <module> EventCheckerOG </module>
                <!-- HYBRID reconstruction part -->
                <module> FdCalibratorOG </module>
                <module> SdCalibratorOG </module>
                <module> FdPulseFinderOG </module>
                <module> FdSDPFinderOG </module>
                <module> FdAxisFinderOG </module>
                <module> HybridGeometryFinderOG </module>
                <module> FdApertureLightOG </module>
                <module> FdProfileReconstructorKG </module>
            <module> RecDataWriterNG </module>
        </loop>
    </moduleControl>
</sequenceFile>
```

The general modules, involved at the beginning and at the end of the sequence, are the following:

- EventFileReader, which reads the raw data (with the shower profile and ground particle data), measured at the Pierre Auger Observatory; or in the simulation case - the input file, created using extensive air shower simulation program (like CORSIKA, CONEX, etc.);

- RecDataWriter – writes down an output of the reconstruction in a format specified by the user (ROOT, ASCII), gives to user a possibility to choose the writing options.

During the hybrid reconstruction a not described previously SD module (SdCalibrator) is launched. It is responsible for the reading in appropriate calibration constants out detector characteristics of the real events and their simulated equivalents.

Appendix A2

A sequence of modules, used for real hybrid Monte Carlo simulation, is presented. This part should precede the reconstruction part to perform the full standard modeling of extensive air shower at the Pierre Auger Observatory.

```
<module> EventGeneratorOG </module>
        <!-- REAL FD simulation part -->
        <module> FdSimEventCheckerOG </module>
        <module> ShowerLightSimulatorKG </module>
        <module> LightAtDiaphragmSimulatorKG </module>
        <module> ShowerPhotonGeneratorOG </module>
        <module> TelescopeSimulatorKG </module>
        <module> FdBackgroundSimulatorOG </module>
        <module> FdElectronicsSimulatorOG </module>
        <module> FdTriggerSimulatorOG </module>
        <!-- REAL SD simulation part -->
        <module> SdSimpleSimKG </module>
```

For simulations with the multiple scattering option switched on, the ShowerPhotonGeneratorST module should be used instead of ShowerPhotonGeneratorOG .

To include the halo telescope effect into the real MC simulation, the TelescopeSimulatorKG module is modified. Instead of this module, its developing version TelescopeSimulatorKG_DEV should be included into the simulation module sequence.

Appendix B

Examples of events, registered at the Pierre Auger Observatory, and then reconstructed using the Offline software, are presented in this appendix part. The following events are the good ones, they do not have clouds in their field of view and some part of their longitudinal profile is in a good agreement with the Gaisser-Hillas function, giving the possibility to obtain good profiles of lateral distribution. As it was already denoted in section 4.2, for convenience, the long number of the Auger events will be replaced by the single numbers. So, Auger event #200812103155 is renamed as event 2, event #200809503337 – as event 3, Auger event #200812102538 – as event 4, and event #200809304337 – as events 5.

The results, obtained from reconstruction of each event, are described in the following by the camera view (a) with triggered pixels, the time fit (b), and longitudinal profiles, drawn as a function of shower age (c) and as a function of slant depth (d). The profiles are rebinned for better display.

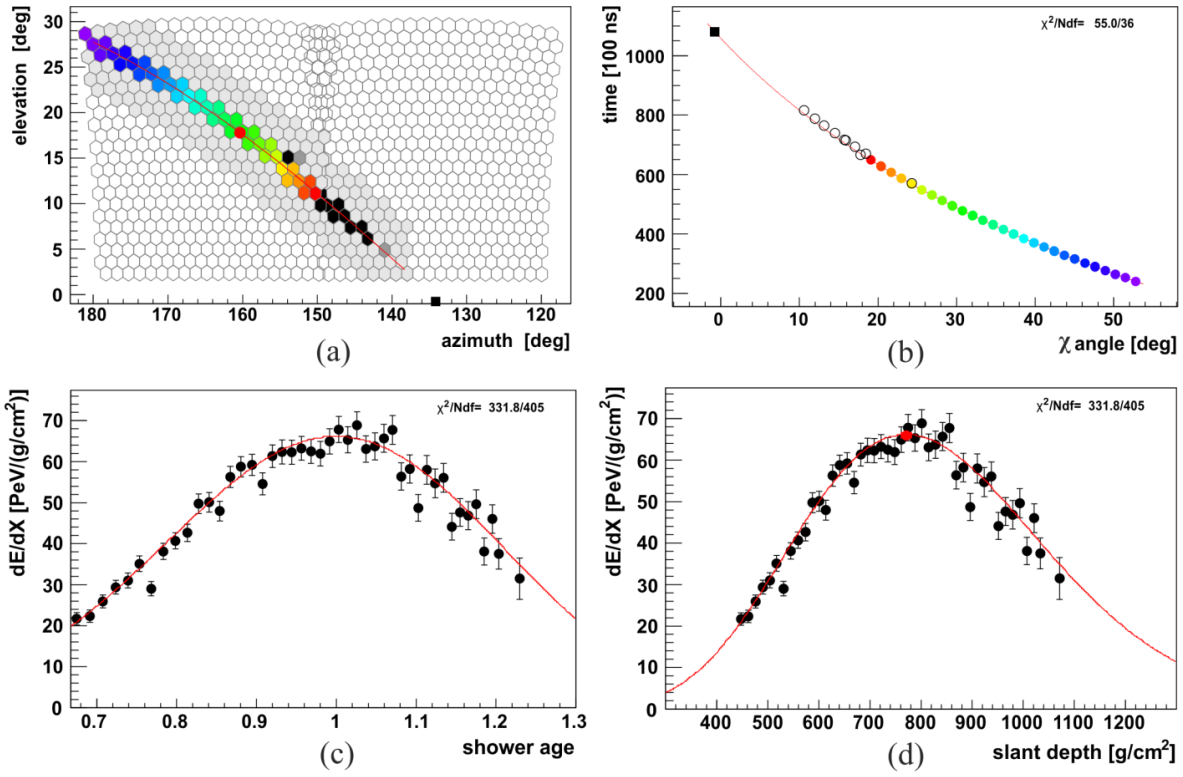

Figure B.1: Auger event 2 with reconstructed energy $E = 43.1 \pm 0.38$ EeV, $X_{max} = 771 \pm 9$ g/cm^2, zenith angle $\theta = 61.2 \pm 0.2°$, azimuth angle $\varphi = 149.4 \pm 0.4°$, distance to the detector ~ 20.39 ± 0.03 km, and total Cherenkov fraction ~ 4%.

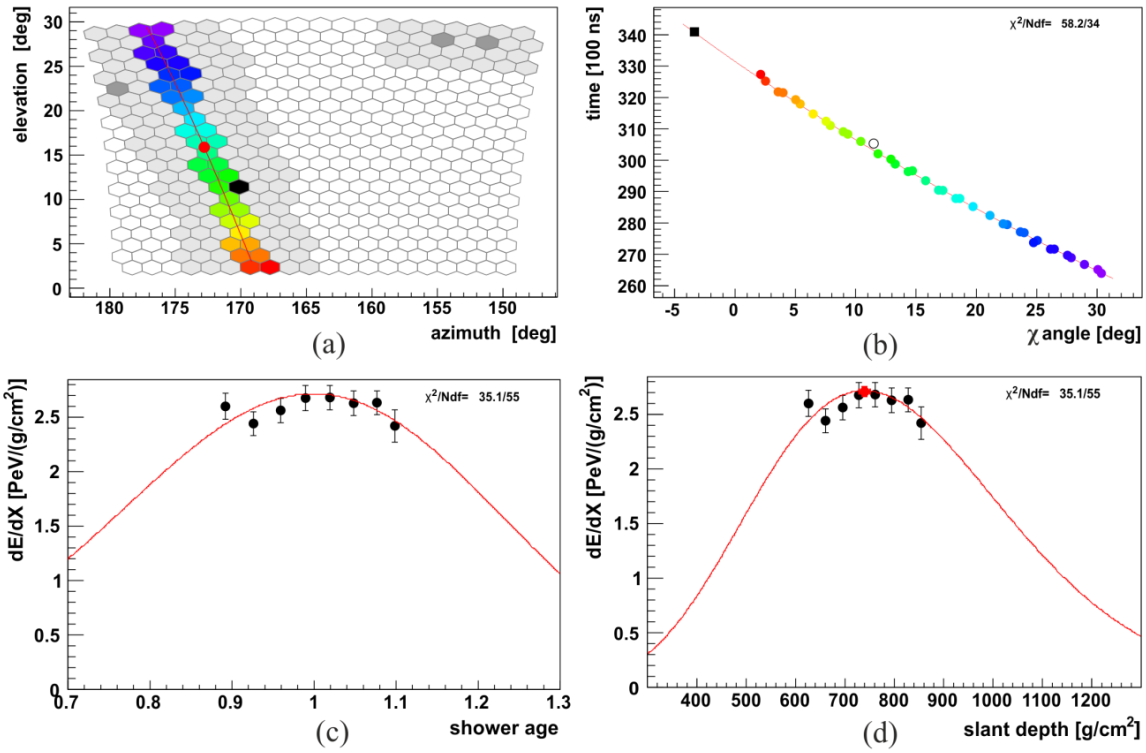

Figure B.2: Auger event 3 with reconstructed energy $E = 1.89 \pm 0.33$ EeV, $X_{max} = 740 \pm 11$ g/cm^2, zenith angle $\theta = 17.3 \pm 0.4°$, azimuth angle $\varphi = 111.8 \pm 1.5°$, distance to the detector ~ 5.28 ± 0.03 km, and total Cherenkov fraction ~ 13%.

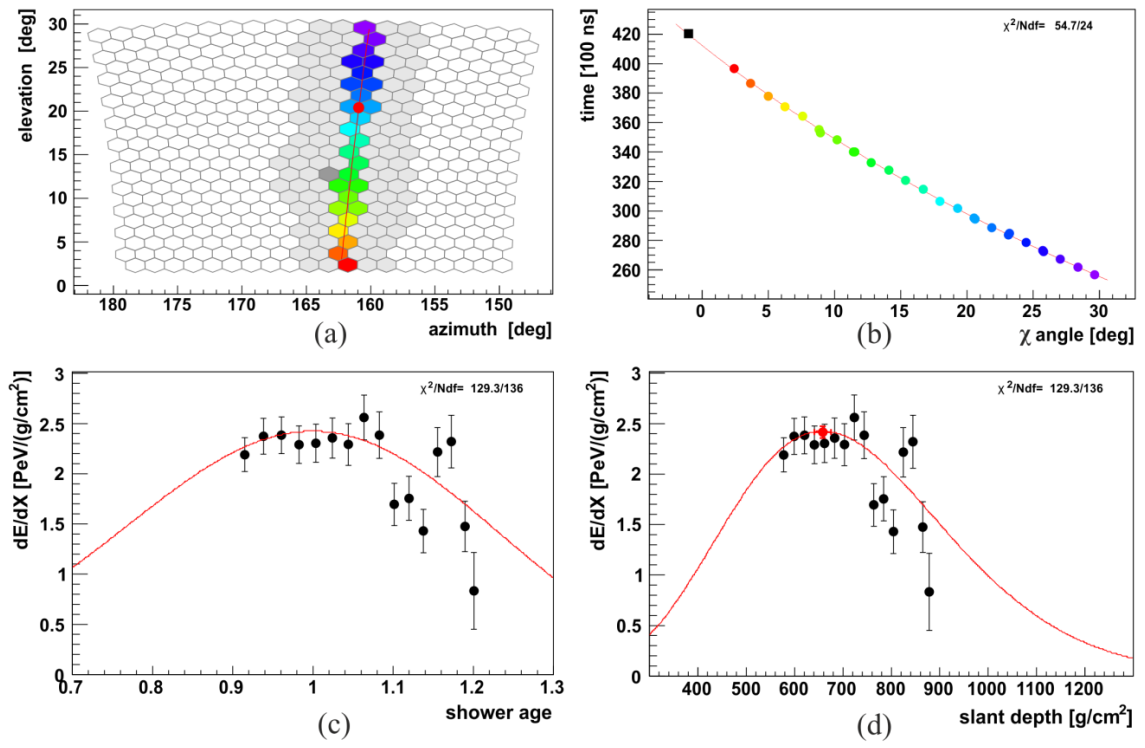

Figure B.3: Auger event 4 with reconstructed energy $E = 1.51 \pm 0.25$ EeV, $X_{max} = 658 \pm 17$ g/cm^2, zenith angle $\theta = 22.3 \pm 0.2°$, azimuth angle $\varphi = 235.8 \pm 1.3°$, distance to the detector ~ 7.69 ± 0.03 km, and total Cherenkov fraction ~ 9%.

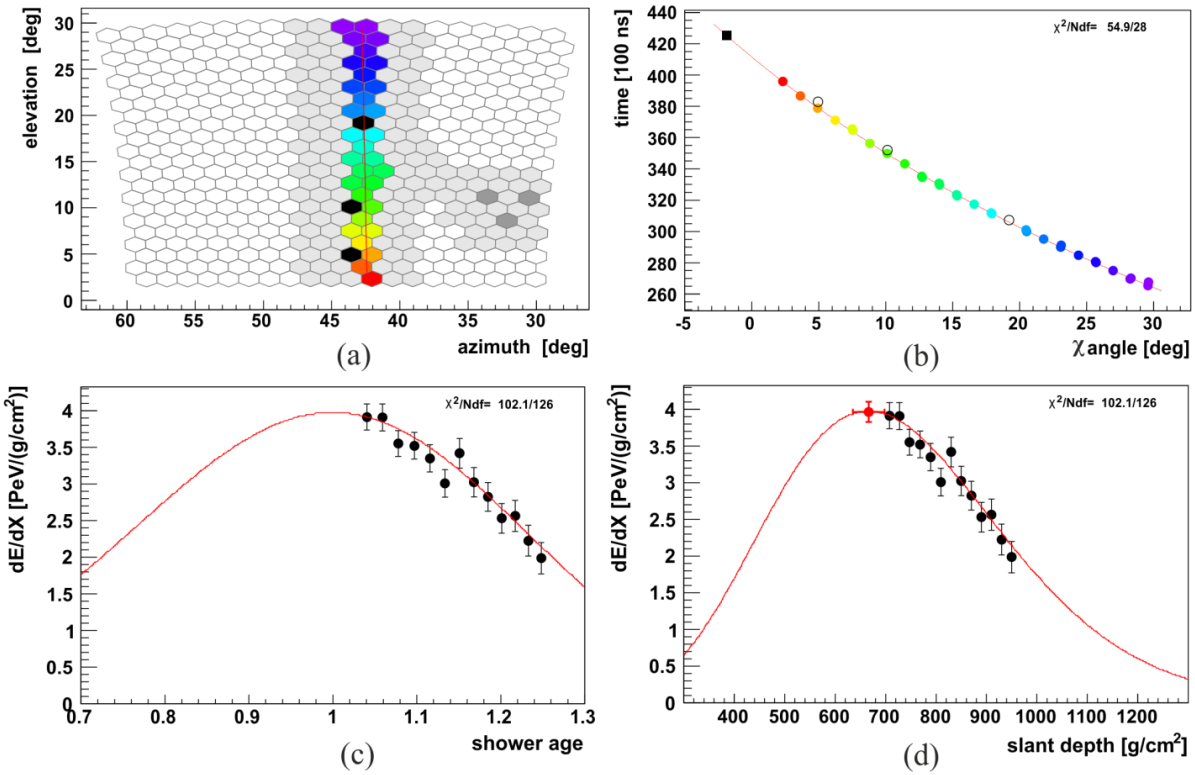

Figure B.4: Auger event 5 with reconstructed energy $E = 2.51 \pm 0.42$ EeV, $X_{max} = 666 \pm 32$ g/cm^2, zenith angle $\theta = 31.0 \pm 0.2°$, azimuth angle $\varphi = 104.2 \pm 0.8°$, distance to the detector ~ 5.89 ± 0.03 km, and total Cherenkov fraction ~ 12%.

Appendix C

The normalized fractions of light are presented for events, discussed in Appendix B. The lateral profiles are built for shower age parameters *s*, specific for each selected event. The circle radius, in which the signal is determined, equals 5 degree. Description of the line colours is given in the plots and in the main text.

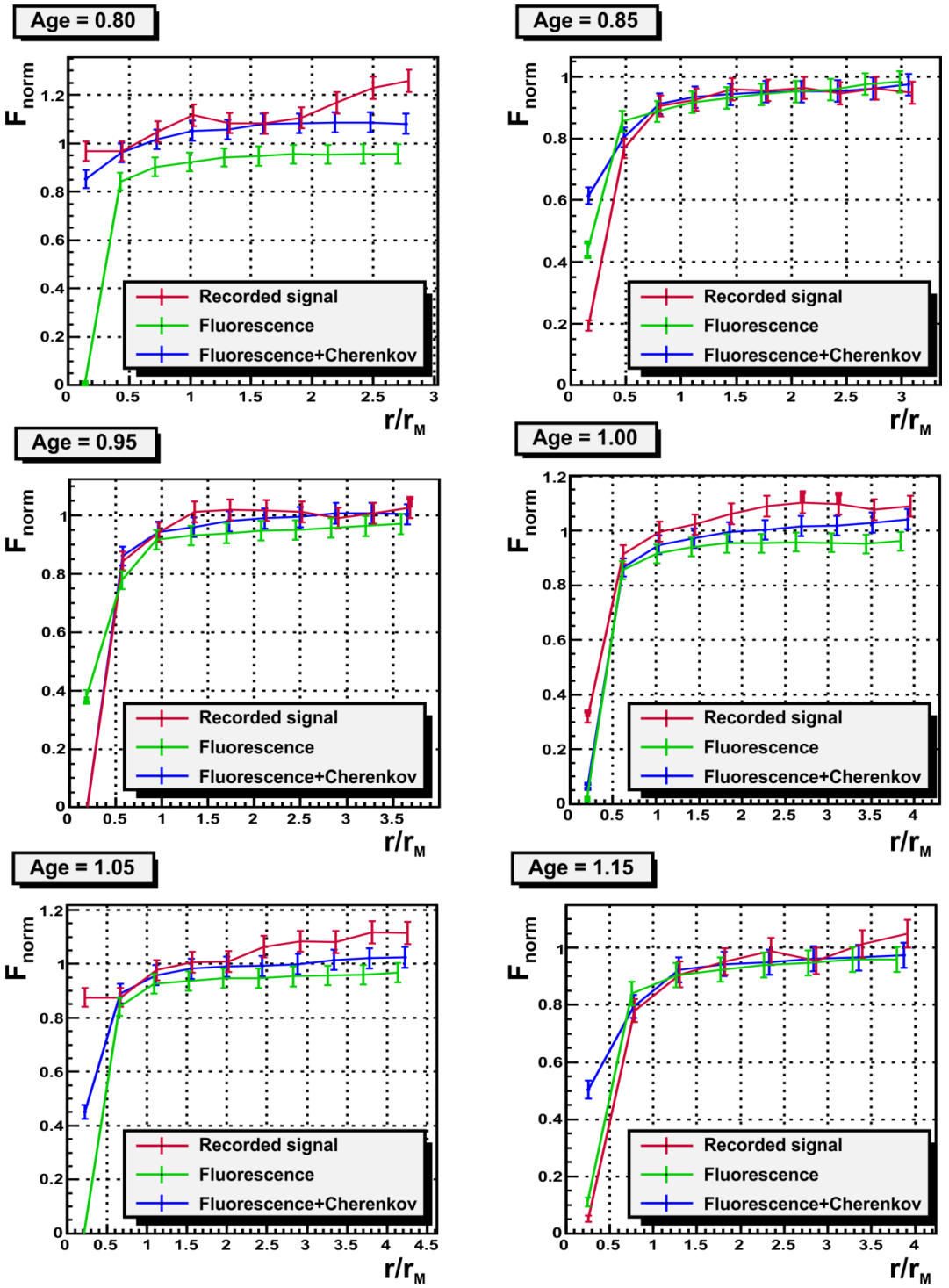

Figure C.1.1. The fractions of light $F_{norm}(r/r_M)$ are obtained for event 2, presented in Fig.B.1 from Appendix B.

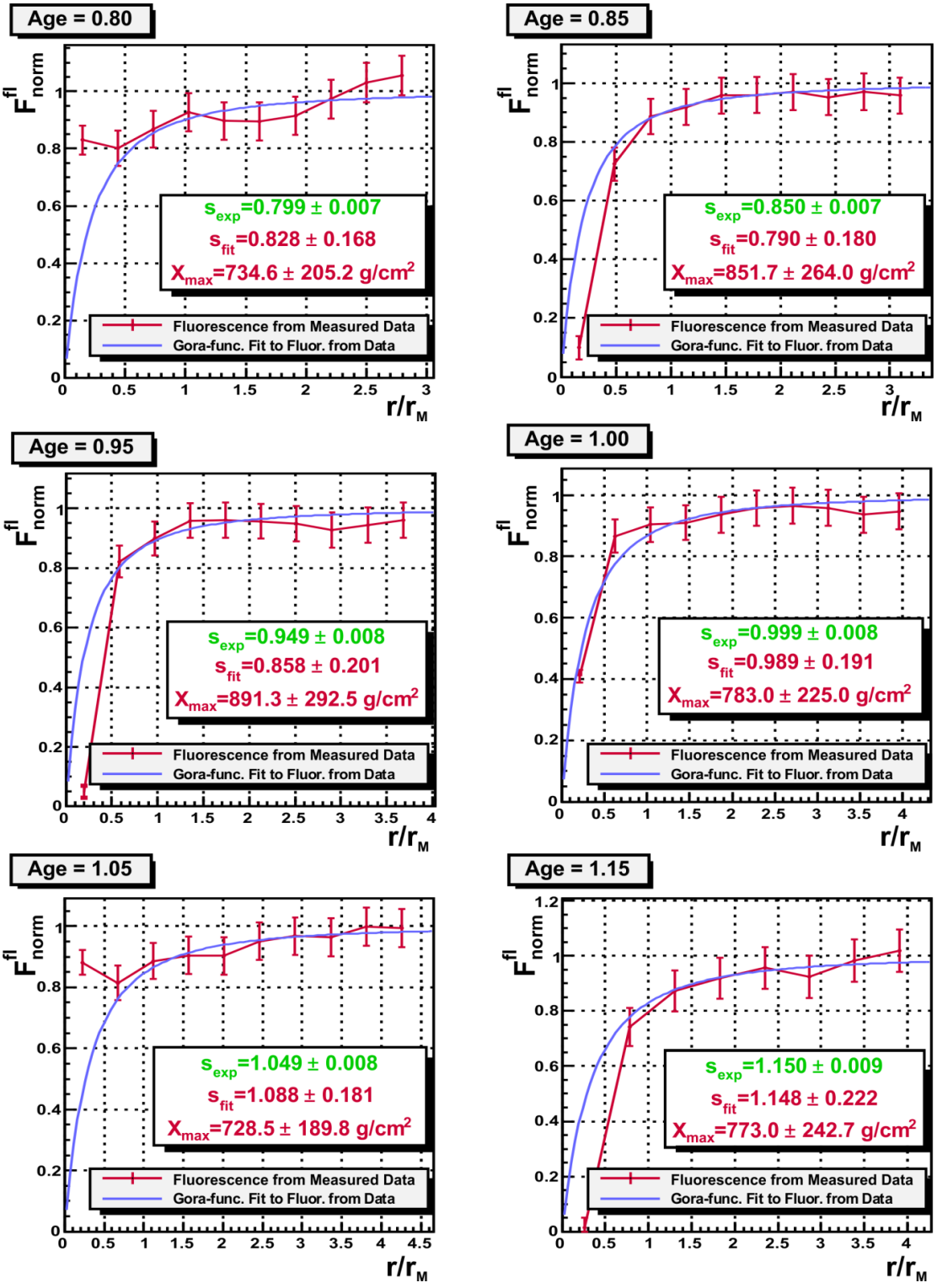

Figure C.1.2: The normalized fractions of fluorescence light $F^{fl}_{norm}(r/r_M)$ are obtained for example event 2, presented in Fig.B.1 from Appendix B. The expected $X_{\max}$ determined from the Gaisser-Hillas fit for this event is $X_{\max}$ = 771 ± 9 g/cm^2.

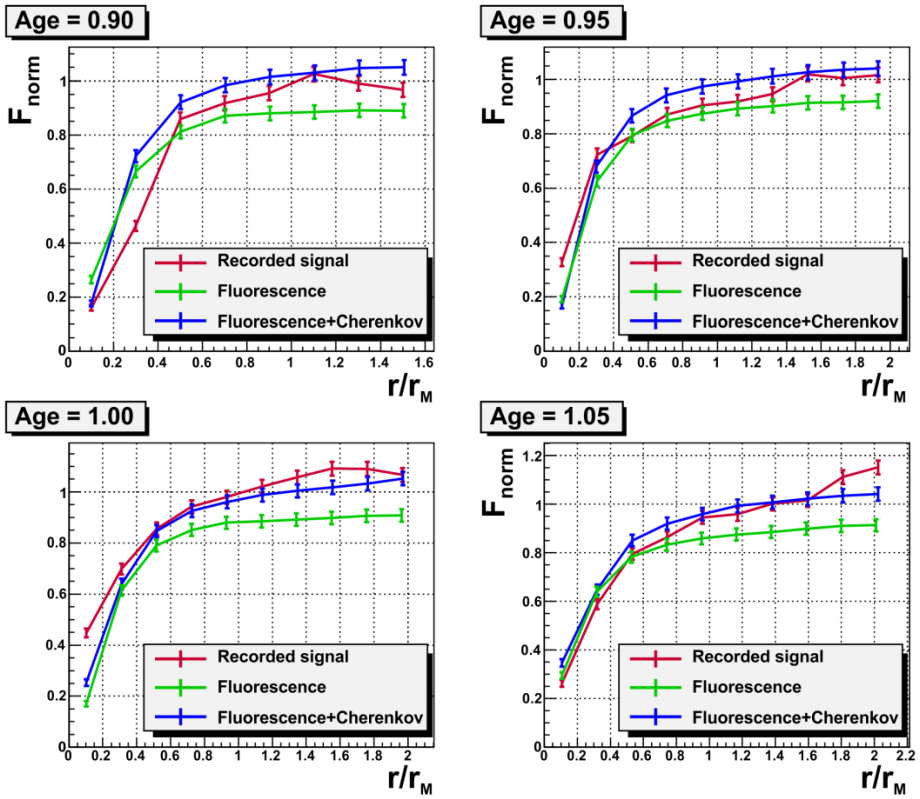

Figure C.2.1: The fractions of light $F_{norm}(r/r_M)$ are obtained for event 3, presented in Fig.B.2 from Appendix B.

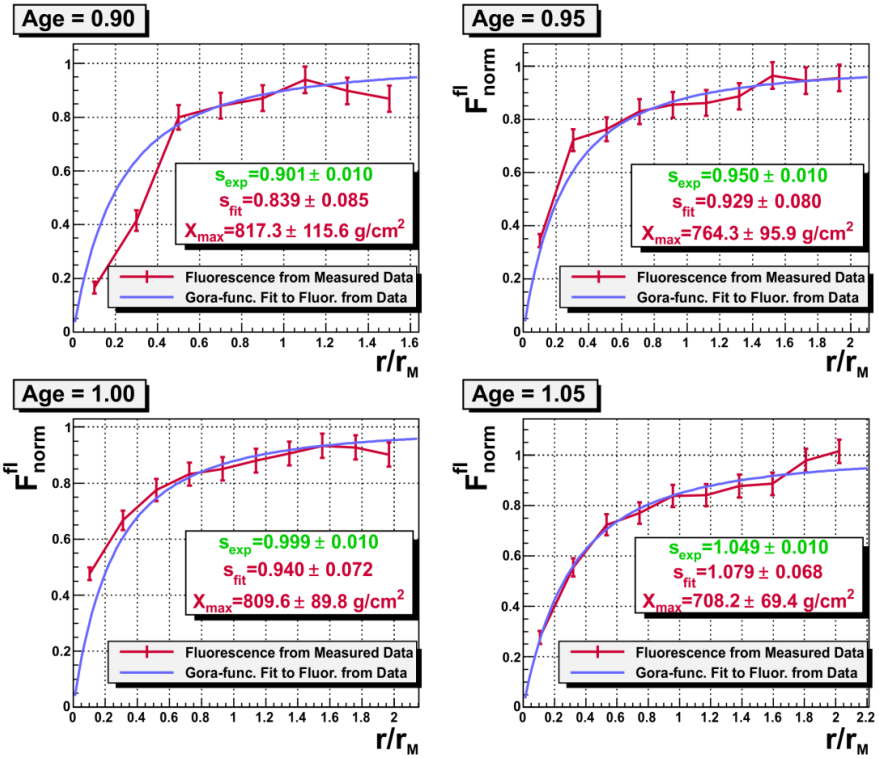

Figure C.2.2: The normalized fractions of fluorescence light $F^{fl}_{norm}(r/r_M)$ are obtained for example event 3, presented in Fig.B.2 from Appendix B. The expected $X_{\max}$ determined from the Gaisser-Hillas fit for this event is $X_{\max} = 740 \pm 11$ g/cm^2.

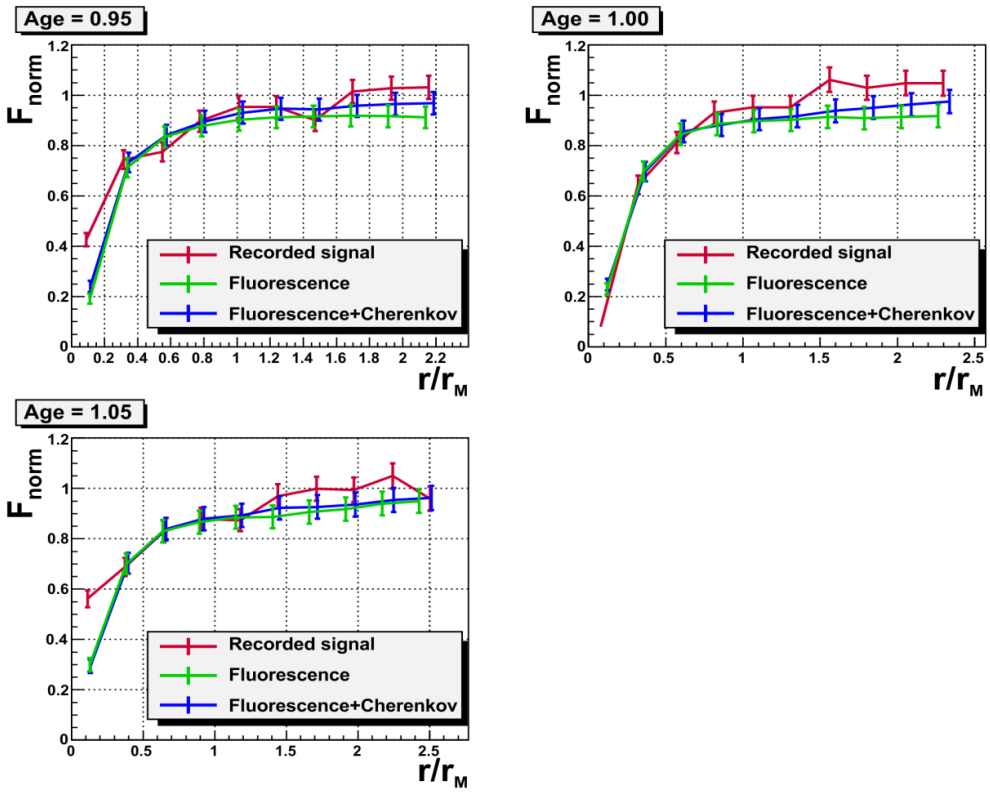

Figure C.3.1: The fractions of light $F_{norm}(r/r_M)$ are obtained for event 4, presented in Fig.B.3 from Appendix B.

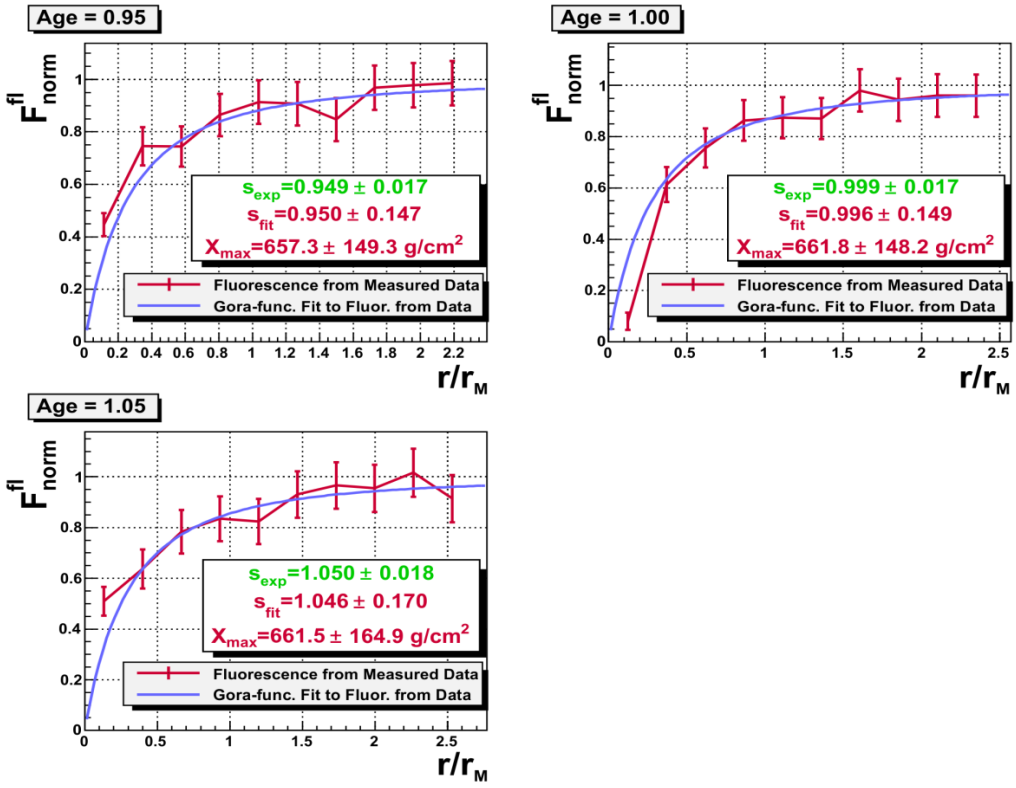

Figure C.3.2: The normalized fractions of fluorescence light $F_{norm}^{fl}(r/r_M)$ are obtained for example event 4, presented in Fig.B.3 from Appendix B. The expected $X_{\max}$ determined from the Gaisser-Hillas fit for this event is $X_{\max} = 658 \pm 17$ g/cm^2.

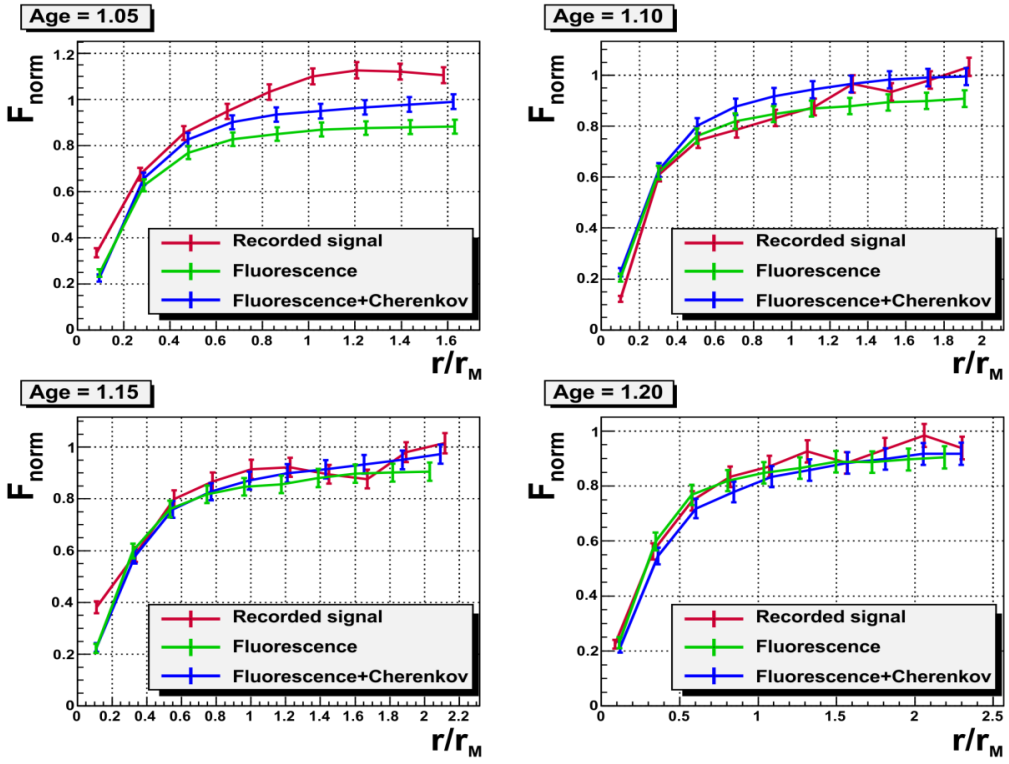

Figure C.4.1: The fractions of light $F_{norm}(r/r_M)$ are obtained for event 5, presented in Fig.B.4 from Appendix B.

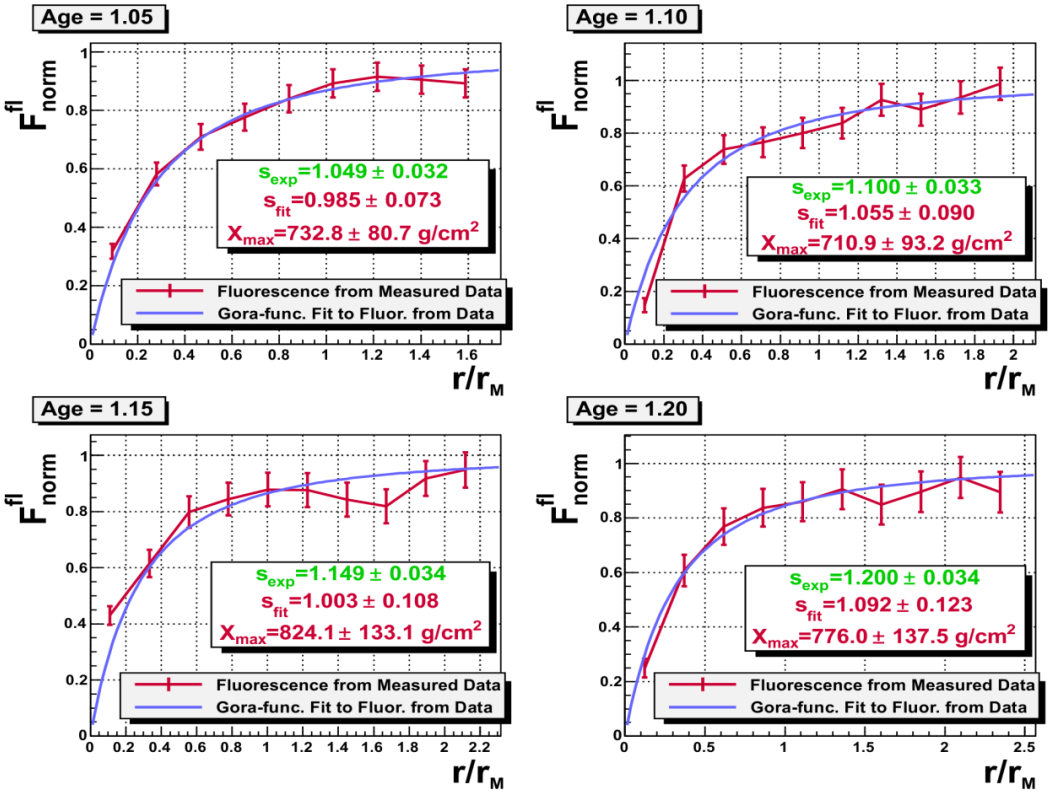

Figure C.4.2: The normalized fractions of fluorescence light $F^{fl}_{norm}(r/r_M)$ are obtained for example event 5, presented in Fig.B.4 from Appendix B. The expected $X_{\max}$ determined from the Gaisser-Hillas fit for this event is $X_{\max}$ = 666 ± 32 g/cm^2.

Appendix D

The normalized fractions of light are presented for events discussed in Appendix B. The lateral profiles are built for the shower development stages, which correspond to atmospheric depth *X*, selected from the longitudinal profile of each event. The circle radius, in which the signal is determined, equals 5 degree. Description of the line colours is given in the plots and in the main text.

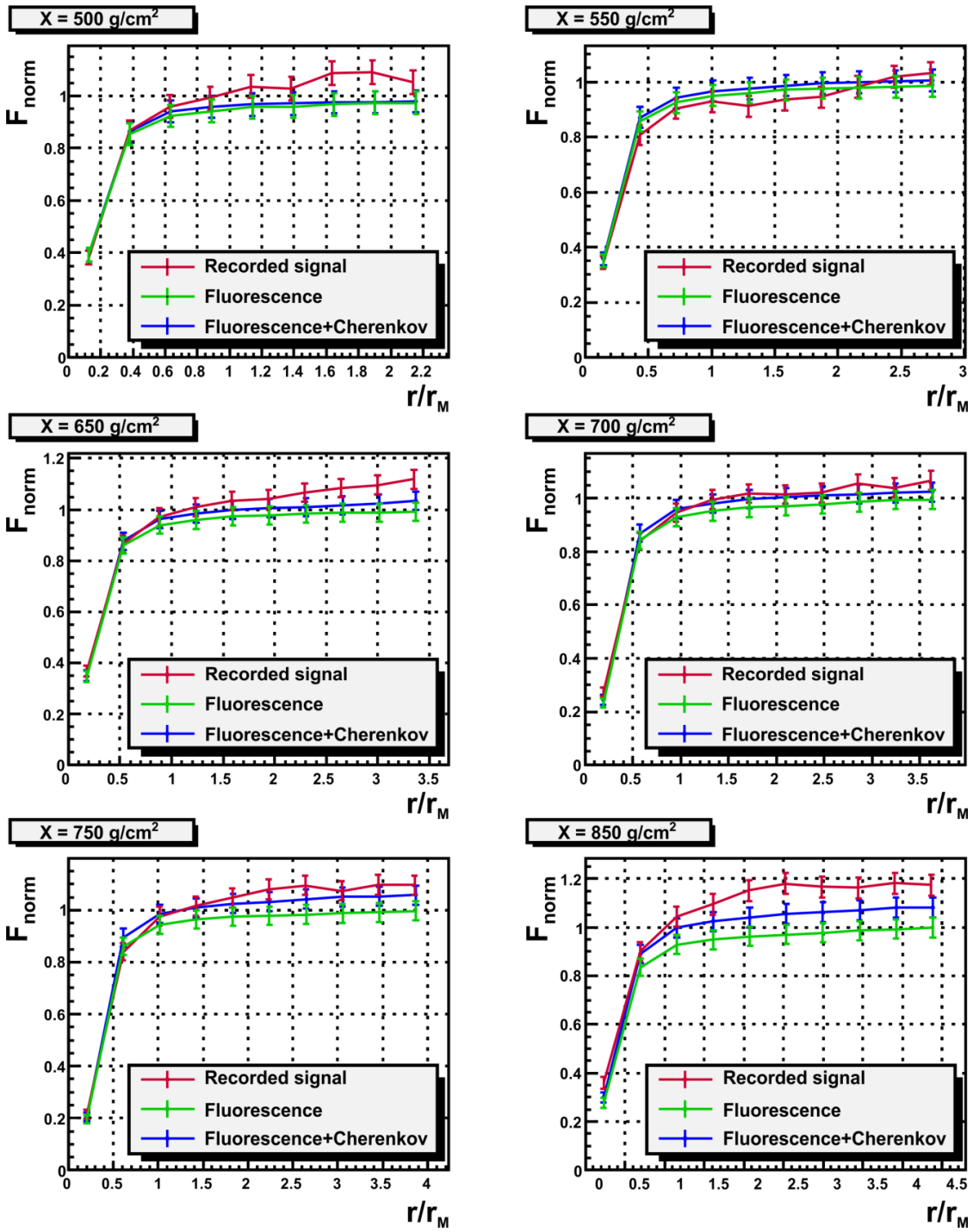

Figure D.1.1: The normalized fractions of light $F_{norm}(r/r_M)$ are obtained for event 2, presented in Fig.B.1 from Appendix B.

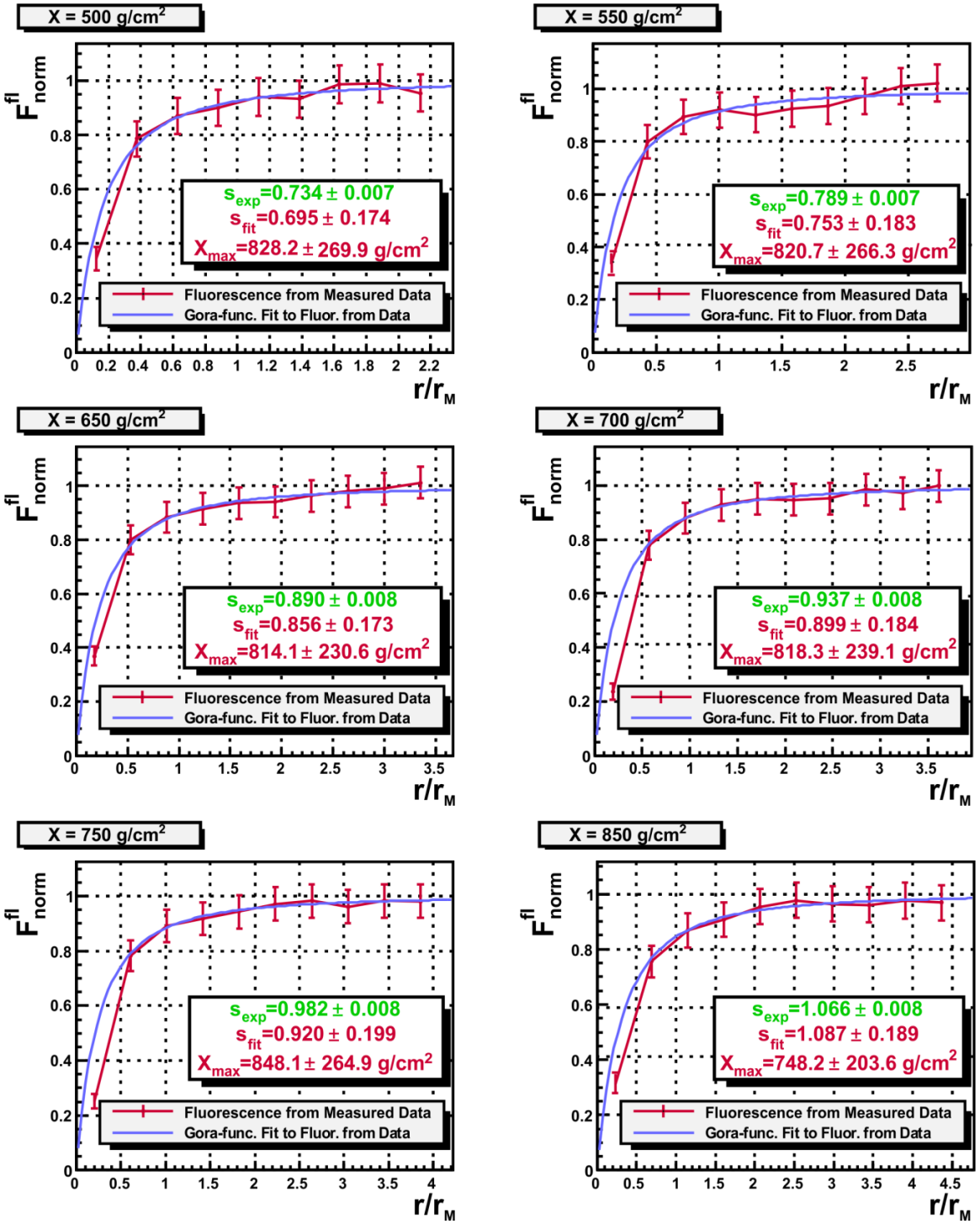

Figure D.1.2: The normalized fractions of fluorescence light $F_{norm}^{fl}(r/r_M)$ are obtained for example event 2, presented in Fig.B.1 from Appendix B. The expected $X_{\max}$ determined from the Gaisser-Hillas fit for this event is $X_{\max}$ = 771 ± 9 g/cm^2.

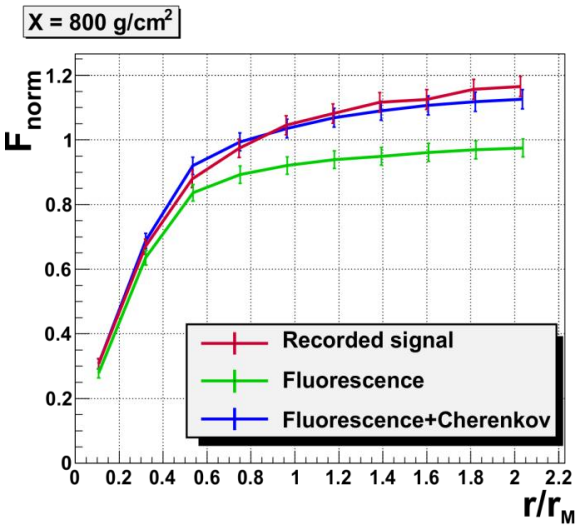

Figure D.2.1: The normalized fractions of light $F_{norm}(r/r_M)$ are obtained for event 3, presented in Fig.B.2 from Appendix B.

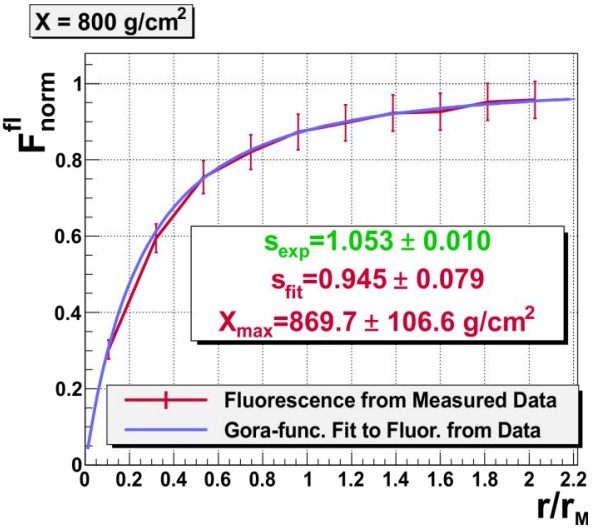

Figure D.2.2: The normalized fractions of fluorescence light $F_{norm}^{fl}(r/r_M)$ are obtained for example event 3, presented in Fig.B.2 from Appendix B. The expected $X_{\max}$ determined from the Gaisser-Hillas fit for this event is $X_{\max} = 740 \pm 11$ g/cm^2.

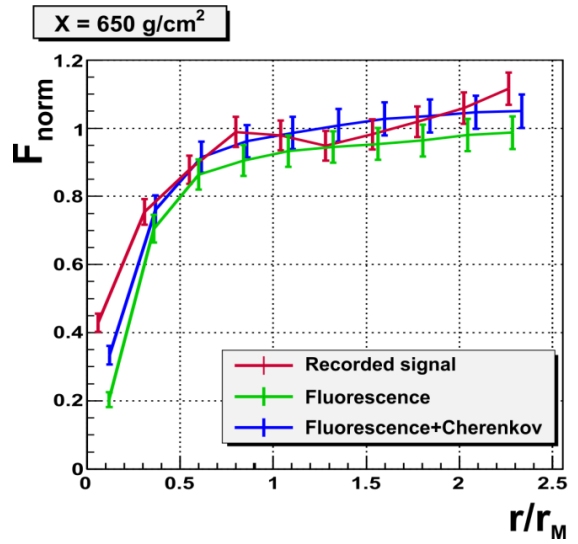

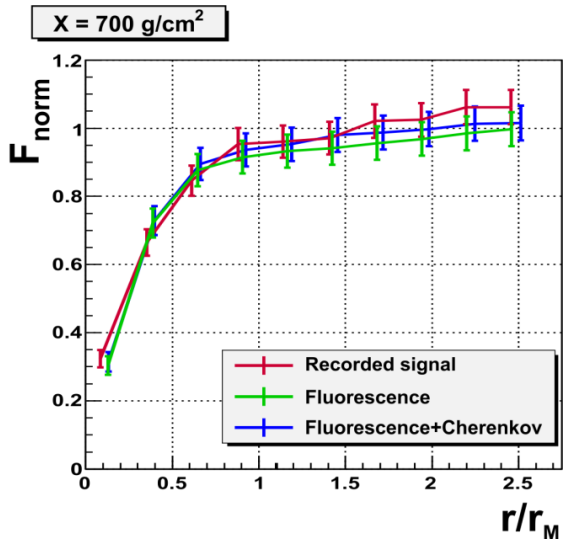

Figure D.3.1: The normalized fractions of light $F_{norm}(r/r_M)$ are obtained for event 4, presented in Fig.B.3 from Appendix B.

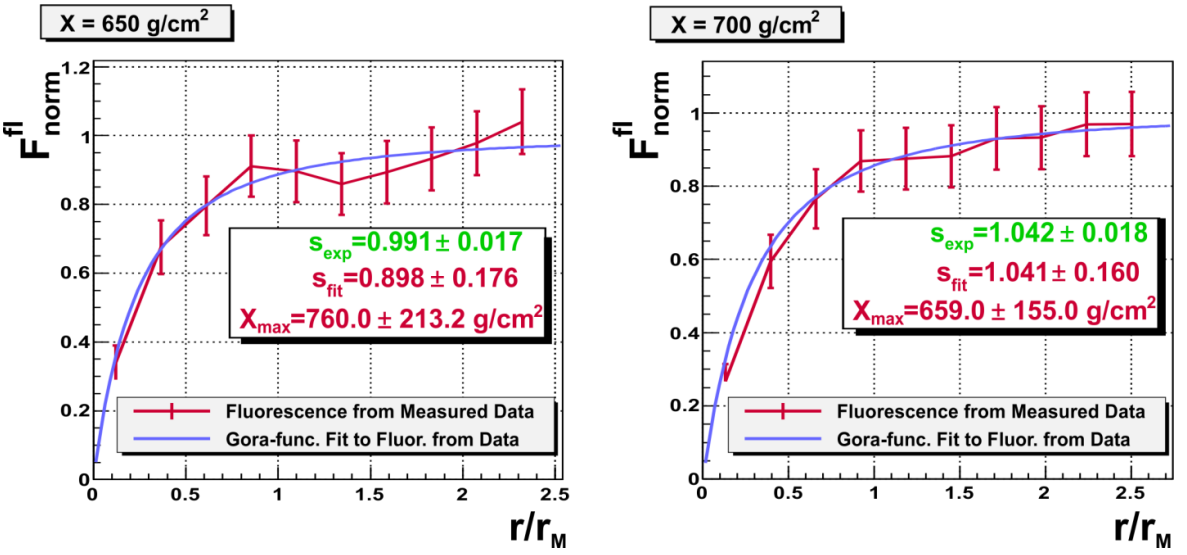

Figure D.3.2: The normalized fractions of fluorescence light $F_{norm}^{fl}(r/r_M)$ are obtained for example event 4, presented in Fig.B.3 from Appendix B. The expected $X_{\max}$ determined from the Gaisser-Hillas fit for this event is $X_{\max}$ = 658 ± 17 g/cm^2.

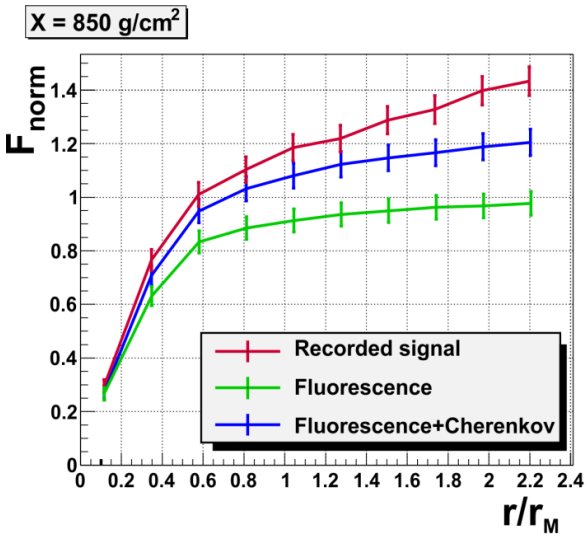

Figure D.4.1: The normalized fractions of light $F_{norm}(r/r_M)$ are obtained for event 5, presented in Fig.B.4 from Appendix B.

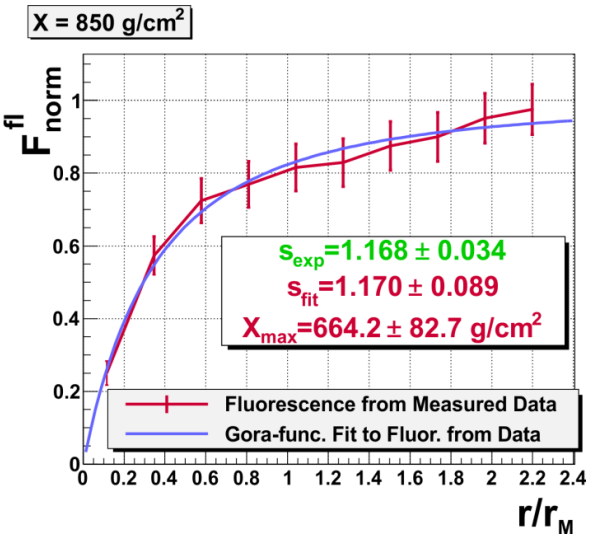

Figure D.4.2: The normalized fractions of fluorescence light $F_{norm}^{fl}(r/r_M)$ are obtained for example event 5, presented in Fig.B.4 from Appendix B. The expected $X_{\max}$ determined from the Gaisser-Hillas fit for this event is $X_{\max}$ = 666 ± 32 g/cm^2.

Bibliography

[1] V. F. Hess, Phys. Zeitschrift 13 (1912), 1084 – 1091.

[2] J. Abraham et al. [The Pierre Auger Collaboration], Nucl. Instr. and Meth. in Phys. Res. A 523(1 – 2) (2004), 50 – 95.

[3] Y. Tameda [the Telescope Array Experiment], Nucl. Phys. B – Proc. Suppl. 196 (2009), 74 – 79.

[4] M.N. Dyakonov et al., Nucl. Instr. and Meth. in Phys. Res. A 248 (1986), 224 – 226.

[5] A. Santangelo, et al. [the JEM-EUSO collaboration], Nucl. Phys. B – Proc. Suppl. 212–213 (2011), 368 – 378.

[6] K. Nakamura et al. [Particle Data Group], J. Phys. G 37, 075021 (2010) and 2011 partial update for the 2012 ed.

[7] K. Greisen, Phys. Rev. Let. 16 (1966), 748 – 750.

[8] R.U. Abbasi et al. [High Resolution Fly's Eye Collaboration], Phys. Rev. Lett. 100 (2008), 101101.

[9] J. Abraham et al. [The Pierre Auger Collaboration], Phys. Rev. Lett. 101 (2008), 061101.

[10] J. Abraham et al. [The Pierre Auger Collaboration], Phys. Let. B 685 (2010), 239 – 246.

[11] J. Cronin, T.K. Gaisser, S.P. Swordy, Sci. Amer. 276 (1997), 44, (updated in www.physics.utah.edu/~whanlon/spectrum.html).

[12] E.S. Seo et al., Astrophys. J. 378 (1991), 763 – 772.

[13] N.L. Grigorov et al., Proc. of 12th ICRC 5 (1971), 1760.

[14] B.N. Afanasiev et al., Proc. Int. Symp. on Extremely High Energy Cosmic Rays: Astrophysics and Future Observatories, Ed. by M. Nagano (1996), 32.

[15] M.A. Lawrence et al., J. Phys. G: Nucl. Part. Phys. 17 *(*1991), 733.

[16] M. Nagano et al., J. Phys. G: Nucl. Part. Phys. 18 (1992), 423.

[17] D.J. Bird et al., Astrophys. J. 424 (1994), 491 – 502.

[18] W. F. Hanlon, Ph.D. Thesis, The University of Utah (2008).

[19] J. Beringer et al. [Particle Data Group], Phys. Rev. D86 (2012), 010001 (http://pdg.lbl.gov).

[20] G.T. Zatsepin, V.A. Kuzmin, Journal of Experimental and Theoretical Physics Letters 4 (1966), 78 – 80.

[21] R.J.Protheroe, P.Johnson, Astropart.Phys. 4 (1966), 253.

[22] J.W.Cronin, Nucl. Phys. 28B – Proc. Suppl. 213 (1992).

[23] V.S. Berezinsky, S.I. Grigor'eva, Astron. Astrophys. 199 (1988), 1.

[24] M.Longair, High Energy Astrophysics, Cambridge University Press (1994).

[25] P.Perkins, Particle Astrophysics, Oxford University Press (2003).

[26] J. Wefel, Cosmic Rays, Supernovae and the Interstellar Medium, NATO ASI Series C 337 (1991), 29.

[27] J. Abraham et al. [The Pierre Auger Collaboration], Phys. Rev. Lett. 104 (2010), 091101-1 – 091101-7.

[28] R.U.Abbasi et al., Astrophys. J. 622 (2005), 910.

[29] J.Bellido et al., Proc. of 31st ICRC, Lodz (2009).

[30] D. J. Bird et al., Astrophys. J. 441 (1995), 144 – 150.

[31] G. Cocconi, Nuovo Cimento 3 (1956), 1433.

[32] A. M. Hillas, Annual Review of Astronomy and Astrophysics 22 (1984), 425 – 444.

[33] P. Bhattacharjee, G. Sigl, Phys. Rep. 327 (2000), 109 – 247.

[34] M. Berezinsky, V. Kachelriess, A. Vilenkin, Phys. Rev. Lett. 79 (1997).

[35] Z. Fodor, S. D. Katz, Phys. Rev. Lett. 86 (2001), 3224 – 3227.

[36] D. Fargion, B. Mele, A. Salis, Astrophys. J. 517 (1999), 725 – 733.

[37] E. Fermi, Phys. Rev. 75 (1949), 1169 – 1174.

[38] W. F. Swann, Phys. Rev. 43 (1933), 217 – 220.

[39] P. Auger, et al., Rev. of Modern Physics 11 (1939), 288 – 291.

[40] T.K. Gaisser, Cosmic rays and particle physics, Cambridge University Press (1990).

[41] T.K. Gaisser, A. M. Hillas, Proc. 15th ICRC 8, Plovdiv (1977), 353.

[42] W. Heitler, The Quantum Theory of Radiation, Oxford University Press, 3 ed. (1954).

[43] K.-H. Kampert, M. Unger, Astropart. Phys. 35 (2012), 660 – 678.

[44] B. Rossi, K. Greisen, Rev. Mod. Phys. 13 (1941), 240.

[45] H. S. Snyder, Phys. Rev. 76 (1949), 1563 – 1571.

[46] K. Greisen, Progress in Cosmic Ray Physics, volume 3, Amsterdam (1956).

[47] D. Heck et al., FZKA-6019, Forschungszentrum Karlsruhe (1998).

[48] K. Greisen, Annual Review of Nuclear Science, 10 (1960), 63 – 108.

[49] J. Linsley, L. Scarsi, B. Rossi, Journal of the Phys. Soc. of Japan Suppl. C, 17 (1962), 91.

[50] N. Chiba et al. [AGASA Collaboration], Nucl. Instr. Meth. A 311 (1992), 338 – 349.

[51] D.M. Edge et al., Journal of Phys. A (Mathematical General) 6 (1973), 1612 – 1634.

[52] D.Newton et al., Astropart. Phys. 26, 6 (2007), 414 – 419.

[53] K. Kamata, J. Nishimura, Prog. Theoret. Phys. Suppl. 6 (1958), 93.

[54] R.M. Baltrusaitis et al., Nucl. Instr. Meth. A 264 (1988), 87 – 92.

[55] T. Abu-Zayyad et al., Nucl. Instr. Meth. A 450 (2000), 253 – 269.

[56] R.M. Baltrusaitis et al., Nucl. Instr. Meth in Phys.Res. A 240 (1985), 410 – 428.

[57] F. Kakimoto et al., Nucl. Instr. Meth. A 372 (1996), 527.

[58] A.N. Bunner, Ph.D. Thesis, Cornell University (1967).

[59] M. Nagano et al., Astropart. Phys. 20 (2003), 293.

[60] B.R. Dawson, Proc. of 30th ICRC 4, Mérida (2007), 425 – 428.

[61] I. Allekotte et al., Nucl. Instr. Meth. A 586 (2008), 409 – 420.

[62] J. Abraham et al., Nucl. Instr. Meth. A 620 (2010), 227 – 251.

[63] M. Born, E. Wolf, Principles of Optics, Cambridge University Press (1980).

[64] R. Sato, C. O. Escobar, Proc. of 29th ICRC, Pune (2005), 3 – 11.

[65] R. Jansson, et al., J. Cosmol. Astropart. Phys. 7 (2009), 21.

[66] H. Gemmeke et al., IEEE Transactions on Nuclear Science 47 (2000), 371 – 375.

[67] B. Keilhauer et al., Astropart. Phys. 22 (2004), 249 – 261.

[68] P. Abreu, et al. [The Pierre Auger Collaboration], Astrop. Phys. 35 (2012), 591 – 607.

[69] B. Fick et al., JINST 1 (2006), P11003.

[70] S.Y. BenZvi et al., Astropart. Phys. 28 (2007), 312 – 320.

[71] S.Y. BenZvi et al., Proc. of 30th ICRC 4, Mérida (2007), 347 – 350.

[72] S.Y. BenZvi et al., Nucl. Instr. Meth. A 574 (2007), 171 – 184.

[73] L. Valore, Proc. of 31st ICRC, Lodz (2009).

[74] H.O. Klages, Proc. of 30th ICRC, Merida (2007).

[75] M. Platino, Proc. of 31st ICRC, Lodz (2009).

[76] T. Huege, Nucl. Instr. and Meth. A 617 (2010), 484 – 487.

[77] R. Pesce, Proc. of 32nd ICRC, Beijing (2011).

[78] M. Unger, et. al., Astronomische Nachrichten 328 (2007), 614.

[79] Pedro Facal San Luis, Proc. of 32nd ICRC 2, Beijing (2011).

[80] J. Abraham et al. [The Pierre Auger Collaboration], Science 318 (2007), 939.

[81] P. Abreu et al., Astropart. Phys. 34 (2010), 314 – 326.

[82] S. Argiro et al., Nucl. Instr. and Meth. in Phys. Res. Section 580 (2007), 1485 – 1496.

[83] ROOT, the object-oriented data analysis framework, http://root.cern.ch.

[84] Advanced Data Summary Tree (ADST), The Auger Observer, http://observer.fzk.de.

[85] D. Kuempel, K.-H. Kampert, M. Risse, Astropart. Phys. 30 (2008), 167 – 174.

[86] M. Unger, et al., Nucl. Instr. Meth. A 588 (2008), 433 – 441.

[87] F. Nerling, et al., Astropart. Phys. 24 (2006), 421 – 437.

[88] D. Heck, T. Pierog, Extensive Air Shower Simulation with CORSIKA: A User's Guide, (2010).

[89] T. Bergmann et al., Astropart. Phys. 26 (2007), 420 – 432.

[90] N. N. Kalmykov, S. S. Ostapchenko, A. I. Pavlov, Nucl. Phys. Proc. Suppl. 52B (1997), 17 – 28.

[91] H. Fesefeldt, The Simulation of Hadronic Showers: Physics and Applications, PITHA-85-02.

[92] D. Góra et. al, Astropart. Phys. 24 (2006), 484 – 494.

[93] M. Giller et al., Proc. of 28th ICRC, Tsukuba (2003).

[94] M. D. Roberts, J. Phys. G: Nucl. Part. Phys. 31 (2005), 1291.

[95] J. Pekala et al., Nucl. Instr. Meth. A, 605 (2009), 388.

[96] P. Sommers, Astropart. Phys. 3 (1995), 349 – 360.

[97] D. Góra, et al., Astropart. Phys. 16 (2001), 129 – 136.

[98] R. Caruso et al., Proc. of 29th ICRC, Pune (2005).

[99] D. Góra, Astropart. Phys. 22 (2004), 29 – 45.

[100] US Standard Atmosphere Model,
http://nssdc.gsfc.nasa.gov/space/model/atmos/us_standard.html.

[101] M. Unger, Proc. of 30th ICRC, Mérida (2007).

[102] J. Parrisius, Diploma thesis, Universitat Karlsruhe (2009).

Acknowledgments

This work was supported in part by the Polish Ministry of Science and Higher Education and National Science Centre under grants No. N N202 207238 and N N202 480939, and by the German Academic Exchange Service (DAAD) under grant No. 507 25595.

I also would like to express a great gratitude to my colleagues from the Department of Cosmic Ray Research of the Henryk Niewodniczański Institute of Nuclear Physics in Kraków for their steady support which has been essential for this thesis preparation. I am especially grateful to my PhD supervisor, prof. Henryk Wilczyński for his guidance, enormous help, patience and support during all the time of my studies. Many thanks to my colleagues dr. Piotr Homola, dr. Barbara Wilczyńska, dr. Jarosław Stasielak and dr. Jan Pękala for their valuable advices and help in my research. I am deeply thankful to dr hab. Dariusz Góra who has provided important initial ideas for this work and feedbacks during my work on the thesis.

Very special thanks to dr. Michael Unger from Karlsruhe Institute of Technology, who never got tired in answering my questions about the Offline software and gave invaluable suggestions for my research.

I also thank prof. Petro Golod and dr hab. Bohdan Hnatyk for inspiring me to become a physicist, and to study the physics of cosmic rays.

I owe a debt of gratitude to my friends, particularly dr. Olesya Klymenko, dr. Yuriy Natanzon, and dr. Volodymyr Marchenko for their steady support and encouragement.

Finally, I express sincere thanks to my parents and my husband for their love and confidence through the past years.